skb.se

SKB TR-25-04

ISSN 1404-0344
ID 2074569
August 2025

Stability of deformation zones at Forsmark

Application of the updated Forsmark stress model and an extended GIA model catalogue

Billy Fälth
Clay Technology AB

Keywords: Zone stability, Stress model, *CFS*, GIA, Monte-Carlo simulation

This report concerns a study which was conducted for Svensk Kärnbränslehantering AB (SKB). The conclusions and viewpoints presented in the report are those of the author. SKB may draw modified conclusions, based on additional literature sources and/or expert opinions.

This report is published on www.skb.se

Abstract

The objective of the work presented in this report was to evaluate the stability of the seven local Forsmark deformation zones ZFMA2, ZFMNW0017, ZFMNW1200, ZFMWNW0123, ZFMWNW0809A, ZFMENE0060A and ZFMENE0062A. These zones were considered since the reactivation of one of these zones may potentially have implications for the repository safety. The stability was evaluated for present-day conditions as well as for conditions that may arise at the beginning or at the end of a period with glacial loading.

The zone stability was evaluated in terms of Coulomb Failure Stress (*CFS*) (*CFS*>0 means instability) while considering the updated Forsmark stress model and an expanded catalogue of Glacial Isostatic Adjustment (GIA) models. The uncertainty in the input was considered by assuming that the input parameters are random variables and the *CFS* calculations were performed by means of Monte-Carlo simulations. Based on the results from the calculations made for present-day conditions, the following could be concluded:

- The steep zones ZFMNW0017, ZFMNW1200, ZFMWNW0123, ZFMWNW0809A, ZFMENE0060A and ZFMENE0062A have high stability. The probability that these zones would be unstable below 0.5 km depth is practically zero.
- The shallow and gently dipping ZFMA2 has low stability over a significant part of its depth extent. The results indicate that the probability of *CFS*>0 is higher than 0.2 down to about 1 km depth. Below 1.5 km depth, there is zero probability of *CFS*>0.

When the probability of *CFS*>0 was estimated for conditions that may arise at the beginning or at the end of a glacial period, it was implied that there actually is a glacial load that influences the stress conditions in Forsmark; the probability of having such load conditions was not considered. The following conclusions could be made:

- In the forebulge, at the beginning of a glacial period, the stability tends to be reduced on the steep zones ZFMNW0017, ZFMNW1200, ZFMWNW0123, ZFMWNW0809A, ZFMENE0060A and ZFMENE0062A relative to what is found for present-day conditions. There is a non-zero probability of *CFS*>0 at all depths on the northwest striking zones ZFMNW0017, ZFMNW1200, ZFMWNW0123 and ZFMWNW0809A. The probability at depths below 0.5 km is in the range 0.01 to 0.04. On the northeast striking zones ZFMENE0060A and ZFMENE0062A, the stability margins are high, with the probability of *CFS*>0 being practically zero at depths below 0.3 km.
- Under endglacial conditions, at the end of a glacial period, the stability tends to be reduced on the gently dipping zone ZFMA2 relative to what is found for present-day conditions. The probability of *CFS*>0 exceeds 0.2 down to about 1.4 km depth.
- Applying excess pore pressure assumptions that are judged to be low-probability bounding cases has a clear impact on the calculated zone stability. For ZFMA2, the two assumptions of endglacial excess pore pressure considered here, the probability of *CFS*>0 at 1.5 km depth increases from 0.1 to 0.4 and 0.9, respectively. When applying the forebulge pore pressure assumption to the steep zones the probability of *CFS*>0 increases from low levels and stays in the range 0.02 to 0.09 at depths below 0.5 km (except for ZFMENE0060A and ZFMENE0062A). Due to the high stability margins on ZFMENE0060A and ZFMENE0062A the excess pore pressure is without practical importance for these zones.
- Extending the ice residence time at maximum load from 25,000 years to 50,000 years gives only modest additions to the glacial stresses. This indicates that the base case GIA model catalogue, which includes the 25,000 years duration case, covers for situations where a large ice sheet remains stationary for times up to at least 50,000 years.

To summarise, the gently dipping ZFMA2 has low stability under present-day conditions and will be further destabilised under endglacial conditions. All steep zones are stable under present-day conditions. Under forebulge conditions, it cannot be excluded that the northwest striking steep zones ZFMNW0017, ZFMNW1200, ZFMWNW0123 and ZFMWNW0809A may become unstable. Regardless of the load conditions, the probability of instability on the northeast striking steep zones ZFMENE0060A and ZFMENE0062A appears to be very low.

Sammanfattning

Syftet med det arbete som presenteras i denna rapport var att utvärdera stabiliteten hos de sju lokala deformationszonerna i Forsmark: ZFMA2, ZFMNW0017, ZFMNW1200, ZFMWNW0123, ZFMWNW0809A, ZFMENE0060A och ZFMENE0062A. Stabiliteten hos dessa zoner studerades eftersom en reaktivering hos någon av dessa potentiellt kan ha implikationer för säkerheten hos förvaret. Stabiliteten utvärderades för nuvarande förhållanden samt för förhållanden som kan uppstå i början eller i slutet av en period med glacial last.

Zonernas stabilitet utvärderades i termer av Coulomb Failure Stress (*CFS*) (*CFS*>0 indikerar instabilitet). I beräkningarna beaktades den uppdaterade spänningsmodellen för Forsmark samt en utökad katalog med modeller för Glacial Isostatisk Anpassning (GIA). Osäkerheten i indata beaktades genom att indataparametrarna antogs vara slumpmässiga variabler och *CFS*-beräkningarna utfördes med hjälp av Monte-Carlo-simuleringar. Baserat på resultaten från beräkningarna för dagens spänningsförhållanden kunde följande konstateras:

- Den ytligt belägna och svagt stupande ZFMA2 har låg stabilitet över en betydande del av sin utsträckning i djupled. Resultaten indikerar att sannolikheten för *CFS*>0 är högre än 0,2 ner till cirka 1 km djup. På djup större än 1,5 km är sannolikheten noll för *CFS*>0.
- De branta zonerna ZFMNW0017, ZFMNW1200, ZFMWNW0123, ZFMWNW0809A, ZFMENE0060A och ZFMENE0062A har hög stabilitet. Sannolikheten att dessa zoner skulle vara instabila på djup större än 0,5 km är praktiskt taget noll.

När sannolikheten för CFS>0 utvärderades för förhållanden som kan uppstå i början eller i slutet av en period med glacial last, förutsattes det att där faktiskt finns en glacial last som påverkar spänningsförhållandena i Forsmark; sannolikheten för att sådana förhållanden uppstår beaktades inte. Följande kunde konstateras:

- I början av en glacial period (”forebulge”), tenderar stabiliteten att reduceras relativt dagens förhållanden på de branta zonerna ZFMNW0017, ZFMNW1200, ZFMWNW0123, ZFMWNW0809A, ZFMENE0060A och ZFMENE0062A. Sannolikheten för *CFS*>0 är större än noll på alla djup för de nordväststrykande zonerna ZFMNW0017, ZFMNW1200, ZFMWNW0123 och ZFMWNW0809A. Sannolikheten för *CFS*>0 på djup större än 0,5 km ligger i intervallet 0,01 till 0,04. För de nordöststrykande zonerna ZFMENE0060A och ZFMENE0062A är stabilitetsmarginalerna höga, och sannolikheten för att *CFS*>0 är praktiskt taget noll på djup större än 0,3 km.
- I slutet av en glacial period tenderar stabiliteten att reduceras relativt dagens förhållanden på den svagt stupande ZFMA2. Sannolikheten för *CFS*>0 är högre än 0,2 ner till cirka 1,4 km djup.
- Att applicera antaganden om portrycksöverskott, vilka bedöms vara extrema och ha låg sannolikhet, har en tydlig påverkan på zonernas stabilitet. För de två antaganden om endglacialt portrycksöverskott som applicerades här ökar sannolikheten för *CFS*>0 på 1,5 km djup för ZFMA2 från 0,1 till 0,4 respektive 0,9. För antagandet om portrycksöverskott som gjordes för forebulgeförhållanden ökar sannolikheten för *CFS*>0 på de branta zonerna men håller sig inom intervallet 0,02 till 0,09 på djup större än 0,5 km (förutom ZFMENE0060A och ZFMENE0062A). På grund av de höga stabilitetsmarginalerna hos ZFMENE0060A och ZFMENE0062A är portrycksöverskottet utan praktisk betydelse för dessa zoner.
- Att förlänga den istäckta periodens varaktighet vid maximal belastning från 25 000 år till 50 000 år ger ett modest tillskott till de glaciala spänningarna. Detta indikerar att basscenariodelen av GIA-katalogen, vilken inkluderar fallet med 25 000 års förlängning, innefattar eventuella effekter av att en stor inlandsis förblir stationär i åtminstone 50 000 år.

Sammanfattningsvis kan sägas att den svagt stupande ZFMA2 har låg stabilitet under nuvarande förhållanden och kommer att destabiliseras ytterligare under endglaciala förhållanden. Alla branta zoner är stabila under nuvarande förhållanden. Under forebulgeförhållanden kan det inte uteslutas att de nordväststrykande zonerna ZFMNW0017, ZFMNW1200, ZFMWNW0123 och ZFMWNW0809A kan bli instabila. Oavsett spänningsförhållanden, förefaller det högst osannolikt att de nordöststrykande zonerna ZFMENE0060A och ZFMENE0062A skulle bli instabila.

Contents

1 Introduction

1.1 Background

The concept for final disposal of high-level spent nuclear fuel developed by the Swedish Nuclear Fuel and Waste Management Co (SKB) is the KBS-3 system, in which the spent fuel is encapsulated in canisters consisting of a cast iron insert surrounded by a copper shell. The canisters are emplaced in vertical deposition holes in crystalline rock at a depth of approximately 500 m and surrounded by a bentonite clay buffer for isolation and protection (SKB 2011). SKB has chosen Forsmark, located in south-eastern Sweden, as the planned site for the spent fuel repository.

SKB must show that the long-term safety of the repository complies with the regulations set up by the authorities. Since the fuel will be hazardous for a very long period of time, the time perspective of the safety assessment is up to one million years (SKB 2011). Hence, the assessment must consider the potential effects of low-probability intraplate earthquakes occurring at shallow depths under present-day stress conditions, as well as earthquakes induced by the effects of future glaciations. The long-term safety assessment is focused on the effects on the repository after closure, when all equipment used during construction and operation is removed and all tunnels and other openings are backfilled.

Shaking alone is not considered to have the potential to jeopardize the integrity of the buffer-canister system, which is confined by the bedrock (SKB 2010a, 2011). The only risk to the repository associated with seismicity is that of canister damage caused by seismically induced fracture shear displacements across canister positions (Fälth et al. 2010). Such displacements may, at least theoretically, be induced by the combined dynamic and quasi-static stress effect generated by an earthquake rupture and the associated shear displacement on a fault plane near the repository.

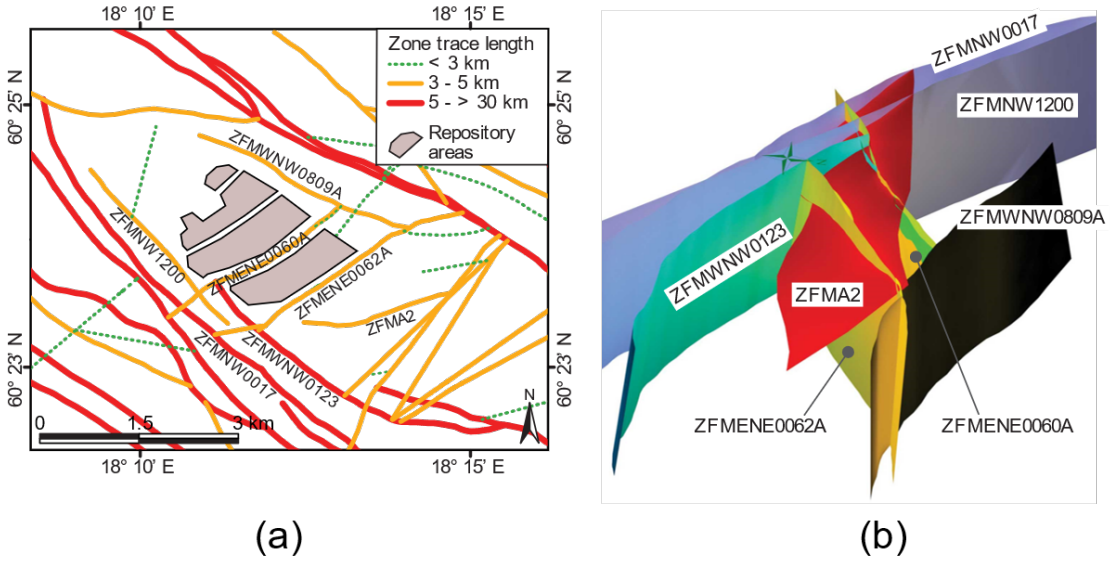

Figure 1-1. *a) Deformation zone map at 470 m depth in Forsmark, and b) 3D view of the zones surrounding the repository volume (view from east) (from Fälth et al. 2016). Among the seven zones with trace lengths > 3 km close to the repository, only one (ZFMA2) is gently dipping.*

It has earlier been concluded (Fälth et al. 2010) that a deformation zone/fault, should it become unstable and act as a seismic source, needs to be longer than 3 km in strike direction to generate stress effects with the potential to jeopardize the safety of the repository. At the repository site in Forsmark, there are seven deformation zones close to the planned repository volume with trace lengths longer than 3 km (Figure 1-1). Hence, for the safety assessment it is of interest to assess the stability of these zones, for present-day stress conditions as well as for the stress conditions that may be the result of stress alterations caused by future glaciations.

The objective of the work that is presented here was to evaluate the stability of the seven large Forsmark deformation zones close to the projected repository volume. The stability of these zones has been examined in previous studies (see section 1.2). However, here a new Forsmark background stress model (Hakami et al. 2025) was applied. This was combined with data from a new catalogue of Glacial Isostatic Adjustment (GIA) model results (Schmidt and Lund 2025) that is more extensive than what previously has been available. As background to the work, a brief description of the previous stability assessments is given below. There is also a description of the theory of glacially induced faulting.

1.2 Previous stability estimates

The stability of Forsmark deformation zones has been evaluated in previous studies. Hökmark et al. (2019) made zone stability estimates while applying a background stress model in general accordance with that proposed by Martin (2007) down to about 1 km depth. At about 2.5 km depth, the model changed from reverse to strike-slip regime, in qualitative agreement with observations by e.g. Lund and Zoback (1999) and Slunga (1991). Hökmark et al. (2019) concluded that the gently dipping ZFMA2 zone is the one that has the lowest present-day stability out of the seven large deformation zones close to the repository volume in Forsmark. They concluded that the other zones, all steeply dipping, are clamped by the high horizontal stresses prevailing in the present-day reverse stress field and hence have considerable stability margins. Furthermore, Hökmark et al. (2019) noted that ZFMA2 is the only large Forsmark zone that would lose stability under endglacial conditions while the steep zones would be stabilized. For the forebulge situation, during ice advance, they concluded that the steep zones would lose stability but remain stable.

Later, Fälth (2022) made further evaluations of the stability of the steep Forsmark deformation zones under forebulge conditions. Here, the background stress model was identical to the model of Martin (2007) down to 0.5 km depth, while the stress gradients applied at larger depths gave a strike-slip regime below 2 km depth and stress anisotropies in general agreement with observations by e.g. Lund and Zoback (1999) in the depth range 4 to 6 km. Fälth (2022) examined the effects on the stability of variations in the background stress magnitudes, background stress orientation as well as of variations in the deformation zone orientations. It was concluded that, given the nominal best estimate background stress magnitudes, none of the steep Forsmark deformation zones will become unstable during forebulge conditions for any assumption of the stress trend or for any of the zone strike and dip values that were considered. However, a reduction of the background minor horizontal principal stress gave a stability reduction due to the increased stress difference in the horizontal plane. One case was tested where the minor horizontal stress was reduced by 11 % at repository depth. This corresponds to a ratio between the two horizontal principal stress components of 2, which is the highest ratio that was expected. For this case, the zones ZFMNW0017 and ZFMNW1200 obtained instability down to about 0.5 km depth while the ZFMWNW0123 and ZFMWNW0809A zones obtained modest instability down to about 0.25 km depth. In another case, which was considered a hypothetical bounding case, the background minor horizontal stress was reduced such that strike-slip stress conditions were obtained at repository depth. In this case, all steep zones except ZFMENE0060A and ZFMENE0062A obtained considerable instability at the surface. The instability tapered off to become zero at about 1 km depth.

Based on the stability calculations and on numerical simulations, Fälth (2022) concluded that, given background stresses within the reported uncertainty margins, conditions for the initiation of an earthquake rupture on the steep Forsmark deformation zones do not exist under present-day conditions and will not exist under future forebulge conditions.

1.3 Glacially induced faulting

A glacial cycle, with ice thicknesses of several kilometres covering parts of the Earth's surface for long periods of time, has a significant impact on the stress field in the upper crust. The weight of the ice is causing the crust beneath the ice cover to bend down into the viscous mantle (Lund et al. 2009). The down-bending is accompanied by an uplift of the crust outside the ice margin, a phenomenon called "forebulge" (e.g. Benn and Evans 2010). The deformation of the crust induces changes to the prevailing background stress field that influence the stability of deformation zones (e.g. Fälth 2018, Hökmark et al. 2019, Lund et al. 2009). The magnitude and orientations of the glacially induced stress changes depend on the glacial evolution (thickness of the ice, its spatial extent and temporal evolution) as well as on the elastic and rheological properties of the crust and mantle (Hökmark and Fälth 2014, Lund et al. 2009).

The glacial stress changes mean that deformation zones, which are stable and seismically quiet under present-day stress conditions, could potentially be reactivated and host earthquakes. The present-day stability on a deformation zone as well as the amount of glacially induced stability reduction, and hence the potential for reactivation, depend on the orientation of the zone, the orientation and magnitude of the background (present-day) stresses as well as on the orientation and magnitude of the glacially induced stress changes (e.g. Hökmark and Fälth 2014). Given the evidence for endglacial faulting in northern Fennoscandia (e.g. Lagerbäck and Sundh 2008) and stability estimates based on results from GIA simulations (Lund et al. 2009), there are two stages during a glacial cycle that are considered to be potentially critical for zone/fault stability (cf. Figure 1-2); (i) the beginning of a period with glacial load when a growing ice sheet, and the associated forebulge, approaches the actual site and (ii) the end of the glaciated period when the stabilising ice cover melts away.

The uplift that is generated at the forebulge by the approaching ice reduces the horizontal stresses in the upper crust and leads to reduced confining stresses on steeply dipping zones. Depending on how the components of the glacial stresses are oriented relative to the background stress field, this may give reduced stability of such zones (Figure 1-2b), and could potentially lead to earthquake triggering (Steffen and Steffen 2021).

At the end of a glaciation, the stress anisotropy in the crust is instead increased due to the melting of the stabilising ice sheet in combination with remaining horizontal excess stresses (Figure 1-2d). The excess stresses have been induced during glaciation by the down-warping of the crust beneath the ice (Lund et al. 2009). There may also be additional horizontal stress excess due to tectonic stresses that have been accumulated beneath the stabilizing ice cover. Increased horizontal stresses destabilise gently dipping fault zones and promote reverse-type faulting (Hökmark and Fälth 2014). This type of fault movement is in accordance with the endglacial faulting that took place in Fennoscandia at the end of the latest Weichselian glaciation. Even though the most prominent traces of endglacial faulting in Fennoscandia are found in the northern parts of the region (e.g. Lagerbäck and Sundh 2008, Munier et al. 2020), it cannot be excluded that significant events will take place further south in connection with future glaciated periods.

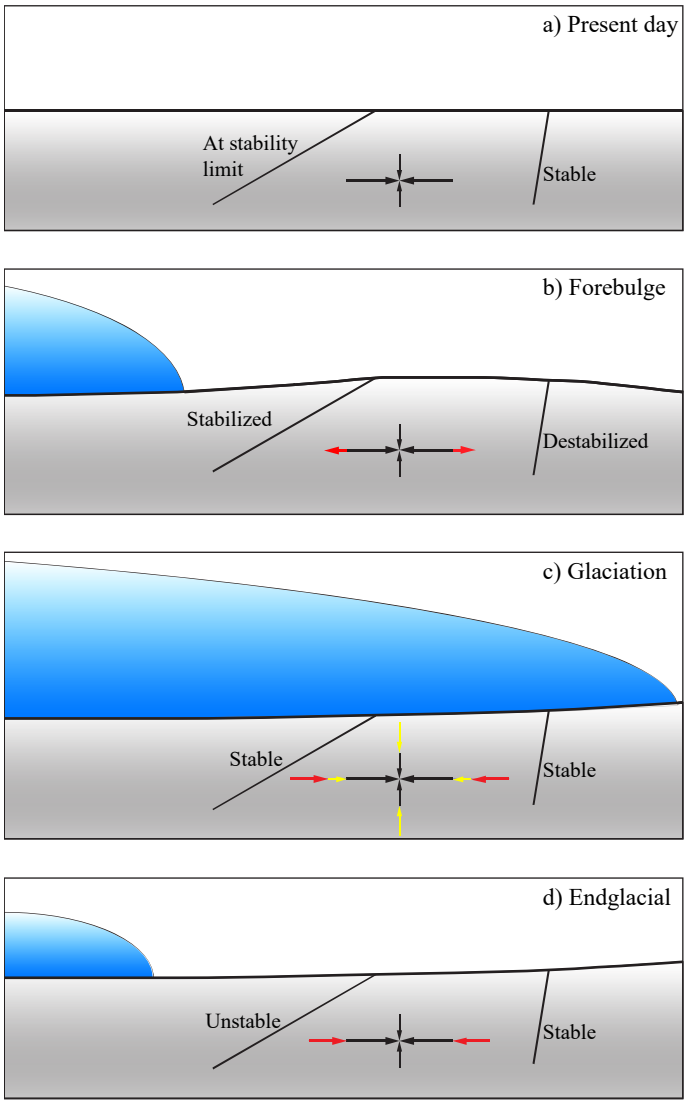

Figure 1-2. *Schematic view of stress evolution in the upper crust during a glaciated period. a) Present-day reverse stress field. High stability on steep deformation zones due to high horizontal stresses. b) Stress field at the forebulge outside the margin of a growing ice sheet. Reduction of horizontal stress (red) and reduced stability of steep zones c) Stress field under a stabilizing ice cover. Vertical stress increased by the weight of the ice and horizontal stress increased due to the direct elastic response to the vertical load (yellow). Tectonic strain accumulation and crustal flexure (red). d) Stress field in region below and outside the margin of a retreating ice. Stresses induced by possible tectonic strain accumulation and crustal flexure remain (red), giving increased stress anisotropy and possibly reactivation of gently dipping fractures and deformation zones. Note: The arrows are not to scale.*

1.4 Scope and objectives

The deformation zone stability assessments cited in section 1.2 were based on the following prerequisites:

- The background stress field in the depth range 0 to 1 km was based on the Forsmark site stress model developed by Martin (2007) (see also Glamheden et al. 2007).
- The glacial stress additions were obtained from a GIA simulation using the University of Maine Ice Sheet Model (UMISM) reconstruction of the Weichselian ice sheet (see e.g. Lund et al. 2009).

Since these stability calculations were performed, a new stress model for the Forsmark site has been developed (Hakami et al. 2025) mainly relying on the recent ranking results of the reliability assessment of overcoring stress measurements at Forsmark (Sjöberg et al. 2025). According to this model, the present-day horizontal stresses at repository depth are more than 30 % higher than those given by the model of Martin (2007). This should have a significant impact on any stability calculations made for Forsmark.

In addition, a set of new GIA simulation results valid for the Forsmark site has been made available (Schmidt and Lund 2025). The set comprises results from simulations where five glaciation models have been combined with five Earth models, resulting in 25 glacial stress evolutions. Some of the combinations have also been used for sensitivity analyses, summing up to a total of 43 GIA models. The GIA results catalogue contains a range of glacial stress evolutions and thus gives a significantly wider case coverage than what has been previously available. The new background stress model and the GIA results catalogue were used as input to the deformation zone stability calculations presented in this report.

The objective of the work presented in this report was to

- Make updated deformation zone stability calculations for the seven Forsmark deformation zones ZFMA2, ZFMNW0017, ZFMNW1200, ZFMWNW0123, ZFMWNW0809A, ZFMENE0060A and ZFMENE0062A close to the projected repository volume using the latest available Forsmark background stress model and the new set of GIA simulation results. The stability was evaluated for present-day conditions as well as for conditions that may arise at the beginning or at the end of a period with glacial loading.
- Account for the uncertainties in the input assumptions by evaluating the stability by means of Monte Carlo simulations where the input parameters are assumed to be random variables with probability distributions rather than being parameters with discrete values.

The calculations were carried out using MATLAB (R2019a) (MathWorks 2020).

2 Input data

To evaluate the stability of a deformation zone, basically three types of input data are needed: zone orientation and location, zone properties and stress field. These are described in this chapter.

The orientations and frictional properties of the deformation zones were based on data from the site investigation in Forsmark (see section 2.1 and 2.2). This also applies for the background stress model. For glacially induced stresses there are no observations. Hence, this data was obtained from GIA simulations of the stress evolution in the crust during glacial cycles.

2.1 Deformation zone orientation

The orientations of the deformation zones were set according to the Forsmark deformation zone model (Petersson et al. 2024). In reality, deformation zones are not perfectly planar but may show spatial variations in both dip and strike. In addition, there will inevitably be uncertainties in the determination of the orientation of a deformation zone. In the zone stability calculations carried out here, the values of zone strike and dip angles (Table 2-1) were assumed to be normally distributed with the most likely values given by the Forsmark site deformation zone model (Petersson et al. 2024). No values of the uncertainty in strike and dip are given in Petersson et al. (2024). The uncertainty ranges given in Table 2-1 were set according to Stephens and Simeonov (2015) and were assumed to represent 95 % confidence intervals. Examples of distributions of strike and dip are shown in Figure 7-1 in Appendix 1.

Note that the uncertainty in dip means that dip values δ larger than 90° are included in the distributed data set for the steep deformation zones (Table 2-1). A dip larger than 90° implies that strike θ would be 180° off the nominal value and that $\delta := 180° - \delta$. However, this is without importance here. For instance, in the calculations presented below, dip and strike values of $\delta = 85°$ and $\theta = 100°$, respectively, would yield the same stability value as [$\delta = 95°$, $\theta = 100°$], [$\delta = 95°$, $\theta = 280°$] and as [$\delta = 85°$, $\theta = 280°$].

Table 2-1. Deformation zone data (Petersson et al. 2024)

Zone	Strike θ (°)*	Dip δ (°)*	Trace length (m)
ZFMA2	82±15	24±10	4000
ZFMNW0017	137±5	85±10	7900
ZFMWNW0123	119±5	82±10	5100
ZFMNW1200	140±5	85±10	3300
ZFMWNW0809A	118±5	90±10	3300
ZFMENE0060A	241±5	85±10	3100
ZFMENE0062A	60±5	85±10	3400

*The uncertainty ranges were set according to Stephens and Simeonov (2015).

2.2 Coefficient of friction

In the deformation zone stability estimate presented in Hökmark et al. (2019), the coefficient of friction on the zones was assumed to be 0.65 while Fälth (2022) assumed the value to be 0.7. Both these assumptions are in accordance with the friction coefficient values approximately in the range 0.58 to 0.75 (friction angles in the range 30° to 37°) reported to be valid for open fractures and deformation zones in Forsmark (Glamheden et al. 2007). All these values agree with values reported by Byerlee (1978) for a range of rock types. According to Byerlee (1978), the friction coefficient of rock is typically in the range 0.6 to 0.85.

In the Monte Carlo simulation performed here, the friction coefficient was assumed to have a normal probability distribution (Figure 7-2 in Appendix 1) with the most likely value set to 0.7 (friction angle 35°) and the 95 % confidence interval assumed to be [0.6 0.8] (friction angles [31° 39°]) (Table 2-2). This implies an assumed standard deviation of 0.05. The standard deviation reported for friction coefficients of open fractures in Forsmark is approximately in the range 0.02 to 0.06 (1.3 to 3.3°) (Glamheden et al. 2007).

2.3 Stress field

When the stability during a glacial cycle was evaluated, the stress field was assumed to be the sum of the background (present-day) stress field and glacially induced stress additions. These are described in the following two subsections.

As noted in section 0, the possibility cannot be excluded that tectonic strain accumulation beneath a stabilizing ice cover will contribute to increased excess in horizontal stress during the endglacial stage. However, since the determination of the tectonic strain rate is associated with large uncertainties, there is a considerable uncertainty regarding the potential for accumulation of tectonic strain. Current GPS measurements indicate that the tectonic strain rates are lower than the uncertainties in the GPS based strain estimates, at approximately 10^{-9}/year (Scherneck et al. 2010). Muir Wood (1995), however, suggested a tectonic strain rate in the Baltic Shield of the order of 10^{-11}/year while Slunga (1991) suggested a rate as high as $1.5 \cdot 10^{-9}$/year. Thus, the strain rate estimates differ by about two orders of magnitude. The potential effects of tectonic strain accumulation are omitted in this work. The possible implications of this are discussed in Chapter 4.

2.3.1 Background (present-day) stress field

According to the background stress model applied here (Hakami et al. 2025) there is a reverse faulting stress regime at depths down to about 2 km in Forsmark (Figure 2-1). The notion of a reverse stress regime at shallow depths is in agreement with conclusions made by Stephansson et al. (1991) regarding stresses in the Fennoscandian shield. At larger depths, the uncertainties regarding both stress regime and stress magnitudes are larger. However, there are observations that give some indications. Measurements made in the Siljan region (Lund and Zoback 1999), as well as earthquake source mechanisms analysed by Slunga (1991), indicate that a strike-slip stress regime dominates at depth in the Baltic Shield. Furthermore, the results of Lund and Zoback (1999) agree with the notion that the crust is in frictional equilibrium on optimally oriented faults (see Zoback & Townend (2001)).

The horizontal principal stress components $\sigma_{H,b}$ and $\sigma_{h,b}$ were modelled using a bi-linear depth dependence (the subscript "b" denotes "background"). This means that strike-slip stress conditions are assumed to prevail at larger depths, in accordance with the observations noted above. The bi-linear relation was set such that $\sigma_{h,b}$ is equal to the vertical stress $\sigma_{v,b}$ at about 2 km depth and that $\sigma_{h,b}<\sigma_{v,b}$ at depths below 2 km. The magnitudes of the principal stress components of the most likely background stress field in Forsmark are defined by (Hakami et al. 2025)

$$\sigma_{H,b} = \begin{cases} 6 - 100z & -0.5 \le z \le 0 \\ 41 - 30z & z \le -0.5 \end{cases}$$

$$\sigma_{h,b} = \begin{cases} 1 - 60z & -0.5 \le z \le 0 \\ 23.5 - 15z & z \le -0.5 \end{cases} \qquad (2\text{-}1)$$

$$\sigma_{v,b} = -26.5z$$

where $\sigma_{H,b}$, $\sigma_{h,b}$ and $\sigma_{v,b}$ are the major horizontal, the minor horizontal and the vertical stress components, respectively, in MPa and z is elevation above sea level (a.s.l.) in kilometres (negative downwards). Note that compressive stresses are here defined as positive.

The observations made by Lund and Zoback (1999) in the Siljan Ring area provide the possibility to check the relevance of the stress magnitudes at depth. At 5 km depth, Lund and Zoback (1999) noted that the minor horizontal stress is approximately two-thirds of the vertical stress. Given the vertical stress $\sigma_{v,b}$ according to Eq. (2-1), this would correspond to 88 MPa. The minor horizontal stress $\sigma_{h,b}$ applied at 5 km depth in the calculations here is 98.5 MPa (Eq. (2-1)), i.e., about 12 % higher. Hence, the horizontal stress levels at the largest depth considered here appear to be slightly higher but in general agreement with those observed by Lund and Zoback (1999).

The stress anisotropy of the stress field defined by Eq. (2-1) corresponds to frictional equilibrium on optimally oriented fault planes (cf. Jaeger and Cook 1979) with a friction coefficient of $\mu = 0.46$ at 2.25 km depth, $\mu = 0.55$ at 5 km depth and $\mu = 0.59$ at 7.5 km depth (cf. most likely values in Figure 2-2). The assumption of a stress anisotropy corresponding to a friction coefficient in the range 0.5 to 0.6 at 4-6 km depth is in agreement with the observations made by Lund and Zoback (1999).

In the stability calculations presented below, the magnitudes of the horizontal principal stress components were handled in a statistical manner by assuming that the magnitudes follow a normal distribution around their most likely values from Eq. (2-1). The reported uncertainty in the horizontal stress values are ±6 MPa for $\sigma_{H,b}$ and ±5 MPa for $\sigma_{h,b}$ (Hakami et al. 2025). When determining the distributions these uncertainty ranges were assumed to correspond to 95 % confidence intervals (Table 2-2). The distributions of stress magnitudes around their most likely values are indicated in Figure 2-1. No distribution was applied for the vertical stress $\sigma_{v,b}$. It was always set according to Eq. (2-1). It can be noted that, close to the surface, where stress levels are low, these constant uncertainty values may result in negative horizontal stresses, i.e., tensional. In the calculations here, no background stress was allowed to be lower than zero.

The observations made by Lund and Zoback (1999) can also be used to check the relevance of the ±6 MPa and ±5 MPa uncertainty ranges of $\sigma_{H,b}$ and $\sigma_{h,b}$ used to define the distributions of stress magnitudes. The upper and lower limits of these ranges applied on the stresses at 4 km depth (Eq. (2-1)) correspond to friction coefficients in the range [0.44 0.63] on optimally oriented planes. The corresponding range of friction coefficients obtained for 5 km depth is [0.47 0.64]. Noting that the observed stress anisotropy at these depths corresponds to a friction coefficient in the range [0.5 0.6] (Lund and Zoback 1999), it appears that the stress uncertainty ranges used here can be considered wide rather than narrow. A wider range should tend to give a larger spread in the output from the stability calculation and correspondingly more pessimistic results.

The most likely trend of $\sigma_{H,b}$ was assumed to be N145°E, in accordance with the Forsmark site stress model (Hakami et al. 2025) and other data from south-central Sweden (Heidbach et al. 2016, Lund and Zoback 1999, Slunga 1991) indicating that the direction of the maximum horizontal stress is in agreement with the push from the Mid-Atlantic Ridge, i.e., in the range N120°E to N150°E. As for the horizontal stress magnitudes, the trend was assumed to have a normal distribution. The 95 % confidence interval of the distribution was set to [N125°E N165°E] (cf. Hakami et al. 2025), which corresponds to a standard deviation of 10°. The interval is in accord with the uncertainty range of the previous Forsmark stress model (Glamheden et al. 2007, Martin 2007) and was also used in the previous zone stability assessment by Fälth (2022). However, this uncertainty may be considered small compared to the uncertainty in stress orientations indicated by the measurements in southern Sweden included in the World Stress Map catalogue (Heidbach et al. 2016). These have been classified to have standard deviations in the range 15° to 25° (see also Gregersen et al. 2021). The majority of these data are based on earthquake focal mechanisms at several kilometres depth. This may lead to larger uncertainties compared to the uncertainties associated with the measurements at smaller depths that were used to develop the Forsmark stress model applied here. However, the possibility cannot be excluded that the uncertainty in stress orientation assumed here is underestimated.

To illustrate the distributions of the stress model parameters, histograms of $\sigma_{H,b}$ and $\sigma_{h,b}$ at 0.5 km depth as well as the $\sigma_{H,b}$ trend are presented in Figure 7-3 in Appendix 1.

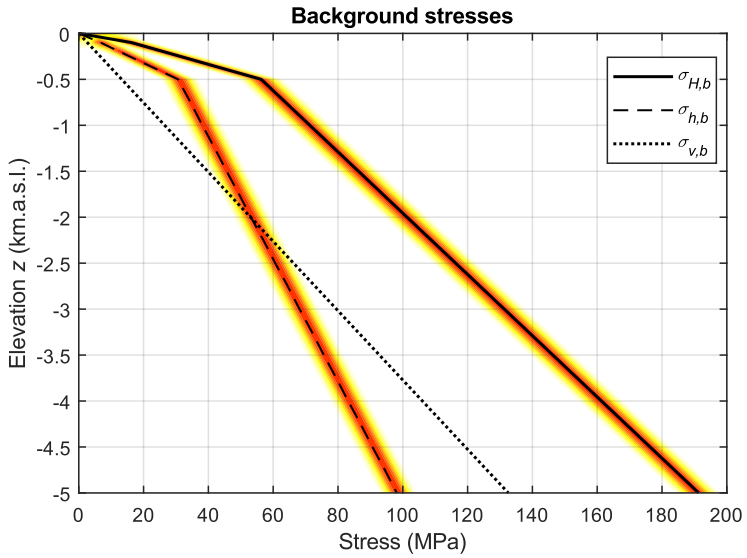

Figure 2-1. *Principal components of the background (present-day) stress field. The colour scale indicates normalised probability density of the horizontal stresses, which were assumed to be normally distributed around their most likely values with the parameter ranges in Table 2-2 corresponding to a 95 % confidence interval. The lines indicate the most likely stress values extracted from the distributions, cf. Eq. (2-1).*

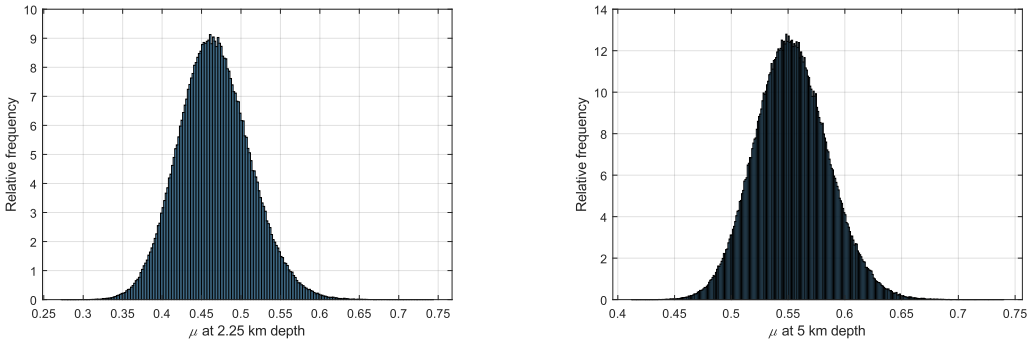

Figure 2-2. *Histograms of friction coefficient values corresponding to frictional equilibrium on optimally oriented planes at 2.25 km and 5 km depth. The values were calculated from the distributions of $\sigma_{H,b}$ and $\sigma_{h,b}$ at respective depth (cf. Figure 2-1).*

Table 2-2. Parameter values for background stress and deformation zones

Parameter	Symbol	Most likely value	Range corresponding to 95 % confidence interval
Background major horizontal stress	$\sigma_{H,b}$	See Eq. (2-1)	±6 MPa
Background minor horizontal stress	$\sigma_{h,b}$	See Eq. (2-1)	±5 MPa
Background major horizontal stress trend		N145°E	[N125°E N165°E]
Zone dip	δ	See Table 2-1	See Table 2-1
Zone strike	θ	See Table 2-1	See Table 2-1
Coefficient of friction	μ	0.7	[0.6 0.8]

2.3.2 Glacial stress additions

As reference when determining the glacial stress input, results from a set of GIA simulations were used (Schmidt and Lund 2025). In these simulations, the evolution of glacial stress additions in Forsmark was estimated for several combinations of Earth models and glacial models. The GIA simulations were carried out using flat-earth models with layers representing the lithosphere and the underlaying mantle. There are five Earth models with different thickness of the lithosphere and different elastic and visco-elastic properties of the lithosphere and the mantle. The Earth models are combined with five ice sheet models. A detailed description of the modelling methodology and the models is given in Schmidt and Lund (2025).

By combining the five Earth models with the five glacial evolutions, 25 stress evolution scenarios were created. In addition, nine of these Earth/ice combinations (three ice models × three Earth models) were selected for additional analysis. In these additional cases, it was assumed that the residence time of the ice coverage was extended at the glacial maximum ice configuration. Two extensions were tested: 25,000 years (+25k) and 50,000 years (+50k). Hence, including these additional cases, in total 25+9+9 = 43 stress evolution scenarios were included in the GIA data set. Here, the +25k case was considered pessimistic, but to be within the frame of the potential variability of future glacial loads (Jens-Ove Näslund 2024-11-22, personal communication). Hence, the +25k case was here included in the base case scenario catalogue. The +50k case was not considered a realistic possibility but was used here as an illustrative case. The ice models and Earth models included in the model catalogue are summarised in Table 2-3.

Two of the ice models are reconstructions of previous glaciations. The UMISM ice model (SKB 2010b) is a reconstruction of the last (Weichselian) glaciation while NH40 (Colleoni and Liakka 2020) is a reconstruction of the Saalian ice sheet that was considerably larger and thicker than the Weichselian ice. Then, there are three ice models (RCPxxx) (Thölix et al. 2019) that are projections of future glaciations based on different assumptions of the future evolution of CO_2 in the atmosphere, i.e., on different CO_2 emission scenarios or Representative Concentration Pathways (RCPs).

The evolutions of the ice sheets are shown in Figure 2-3 and Figure 2-4. As seen in the figures, the NH40 ice has the largest ice volume and also the largest thickness over Forsmark. Its residence time at Forsmark is shorter than that of the Weichselian ice, though. Among the future projection models, RCP45 is the largest with an ice-covered area and ice thickness on par with those of the Weichselian ice sheet. The RCP45e and RCP85 ices are much smaller. In the RCP45e model, the ice boundary just reaches the Forsmark site, and the ice gives only minor vertical load for a short period of time. In the RCP85 model, the ice cover never reaches the site. The shortest distance between the margin of the RCP85 ice and Forsmark is about 200 km. Hence, for the RCP45e and the RCP85 models, Forsmark lies in the forebulge.

Table 2-3. Summary of GIA models

Base case catalogue				**Illustrative case catalogue**	
Original models		*25 kyrs extended ice*		*50 kyrs extended ice*	
Ice models	*Earth models*	*Ice models*	*Earth models*	*Ice models*	*Earth models*
UMISM	M14	UMISM+25k	M14	UMISM+50k	M14
NH40	M118	NH40+25k	VM5a	NH40+50k	VM5a
RCP45	L2017	RCP45e+25k	L11	RCP45e+50k	L11
RCP45e	VM5a				
RCP85	L11				

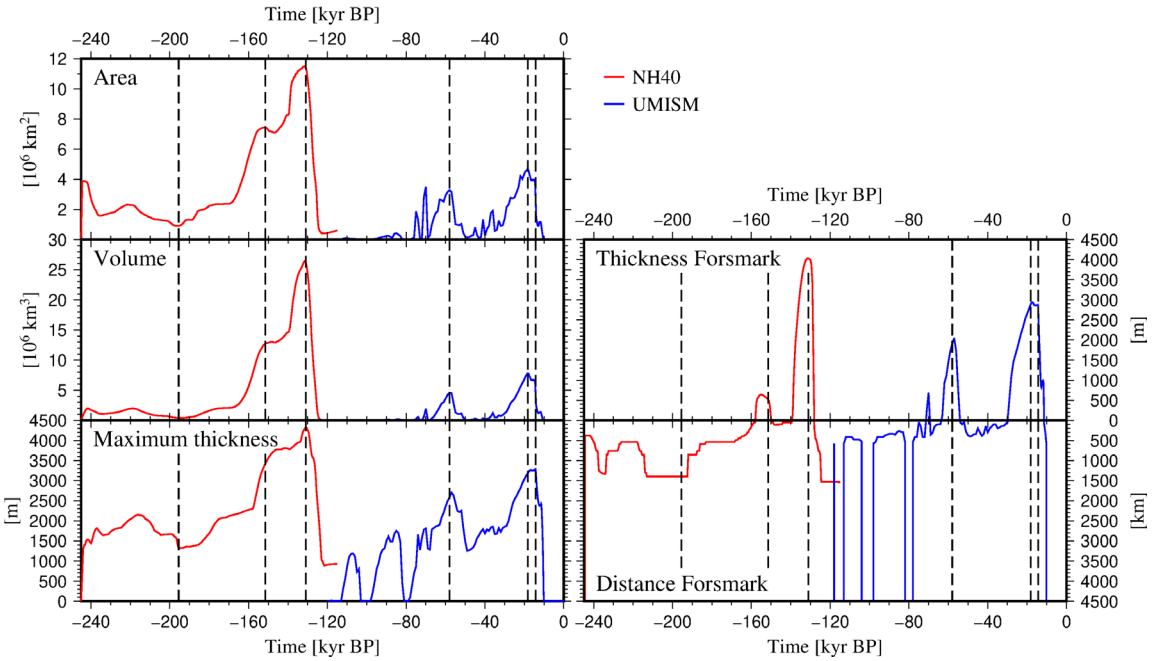

Figure 2-3. *Temporal evolution of the NH40 Saalian and UMISM Weichselian ice sheets (Figure 3-3 in Schmidt and Lund 2025)*

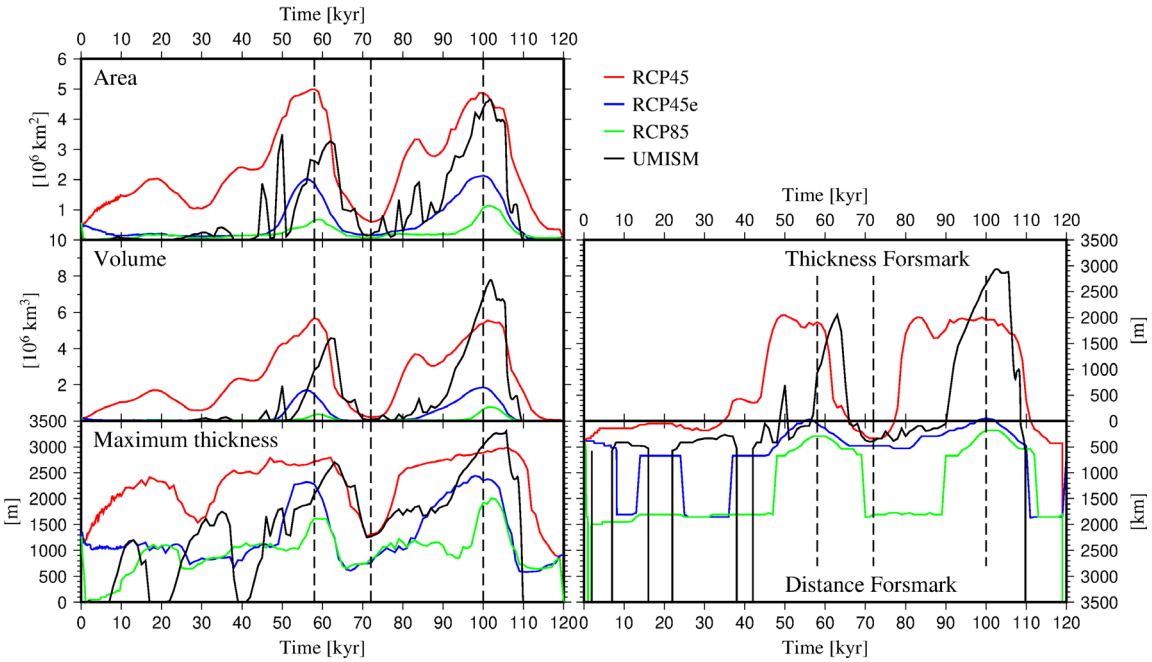

Figure 2-4. *Temporal evolution of the RCP-based ice sheets and the UMISM Weichselian ice sheet (Figure 3-4 in Schmidt and Lund 2025).*

As examples, temporal evolutions of the principal components of the glacial stresses at 1.5 km depth are shown in Figure 2-5 for the Weichselian glacial scenario and in Figure 2-6 for the corresponding scenario with 25,000 years extended ice residence time. There are two stress components which are close to horizontal at most times, $\sigma_{H,g}$ and $\sigma_{h,g}$. The third component, $\sigma_{v,g}$, is close to vertical at most times. The subscript "g" means "glacial". The $\sigma_{H,g}$ trend is taken with respect to North rotating eastwards. The $\sigma_{v,g}$ plunge means the angle of $\sigma_{v,g}$ with respect to the horizontal. Note that since the $\sigma_{v,g}$ plunge may deviate from 90°, $\sigma_{v,g}$ is not always vertical. From this it follows that the $\sigma_{H,g}$ and $\sigma_{h,g}$ components are not necessarily horizontal. Corresponding plots for all glacial scenarios are presented in Appendix 2.

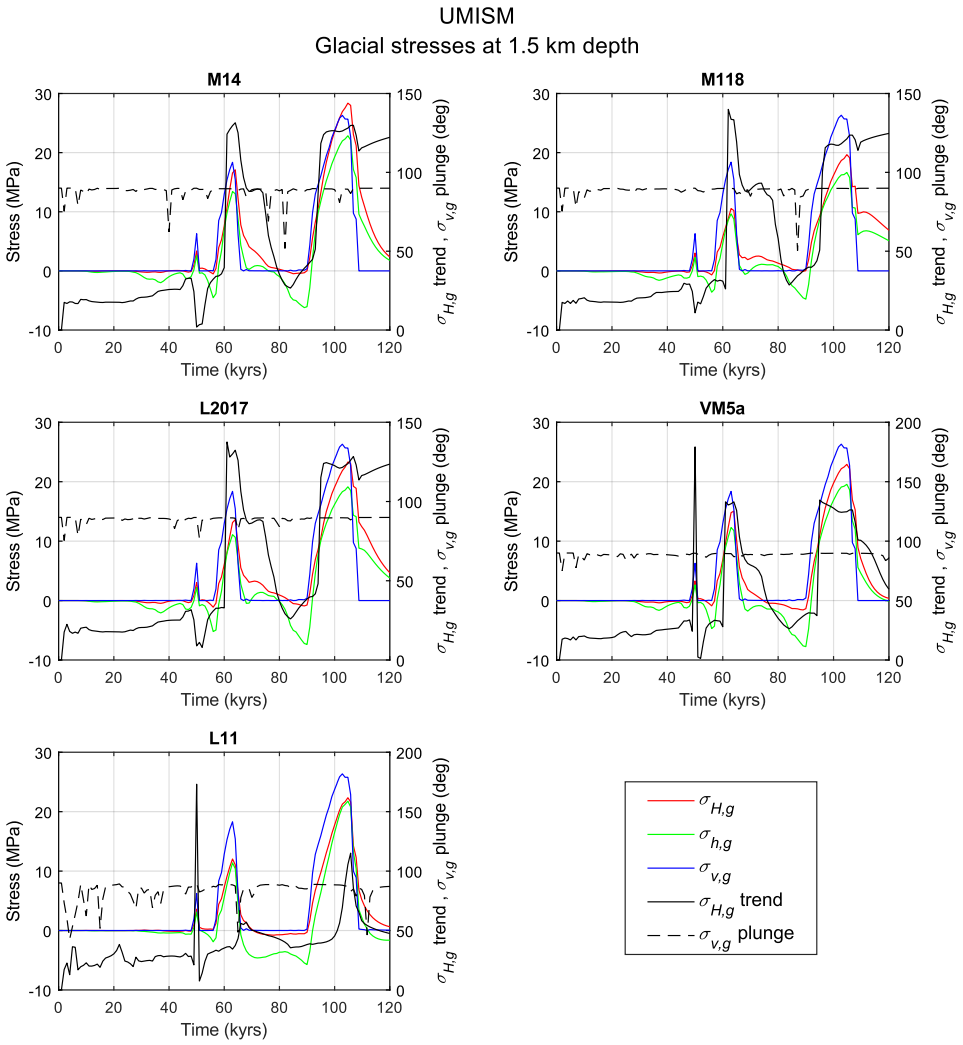

Figure 2-5. *Temporal evolution of principal stress components of the glacial stresses for the Weichselian glacial scenario. The ice model is combined with the five Earth models, cf. Table 2-3.*

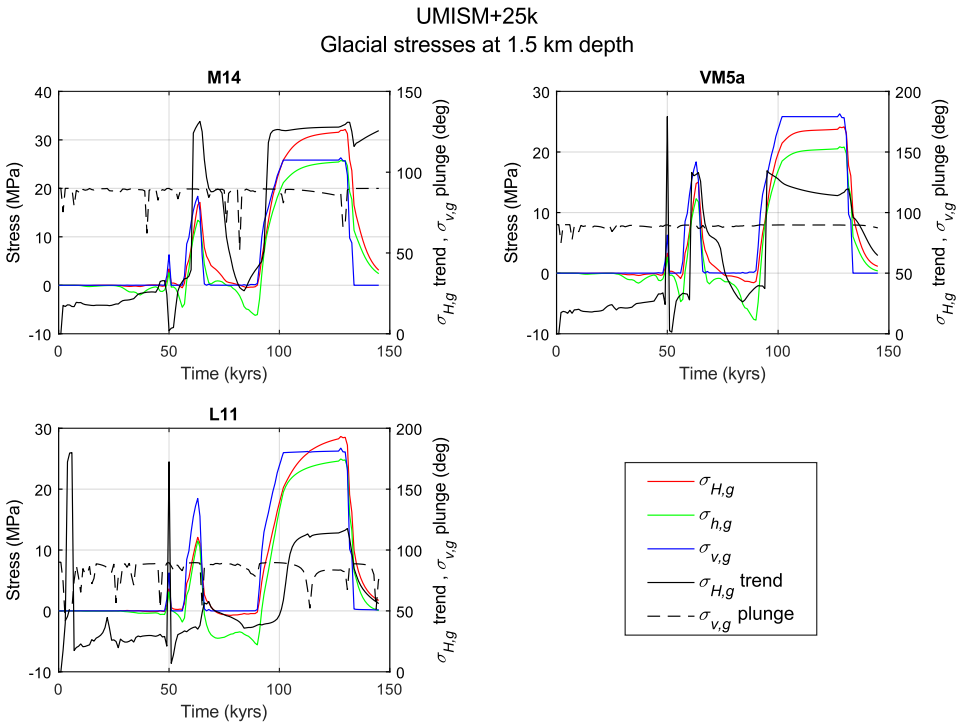

Figure 2-6. *Temporal evolution of principal stress components of the glacial stresses for the Weichselian glacial scenario with 25,000 years extended ice residence time. The ice model is combined with three of the Earth models, cf. Table 2-3.*

3 Evaluation of deformation zone stability

3.1 General

The deformation zone stability was evaluated in terms of Coulomb Failure Stress (*CFS*), which is defined as (Harris, 1998)

$$CFS = \tau - \mu(\sigma_n - P) - c. \quad (3\text{-}1)$$

Here, τ and σ_n are the shear- and normal stresses acting on a fault or fracture plane while μ is the coefficient of friction on the plane, P is pore pressure and c is cohesion. Hence, *CFS* is the difference between the shear load and the shear resistance of the fault or fracture and is thus a measure of the potential for slip. A positive *CFS* value means unstable conditions.

The pore pressure P is the sum of two components, i.e., $P = P_h + P_e$, where P_h is hydrostatic pressure while P_e is excess pressure that may develop in the crust in conjunction with a glaciation. As a base case assumption, P_e is set to zero. In all calculations made here, cohesion c is assumed to be zero. Cohesion values on the order of 1 MPa are reported for deformation zones at Forsmark (Glamheden et al. 2007). Given that the average effective stress at depths below 0.5 km is above about 30 MPa (cf. Eq. (2-1)), and given a coefficient of friction of 0.7, the frictional shear resistance of the deformation zones is on the order of 20 MPa and more. Hence, the cohesional shear resistance (which is constant with depth while the frictional resistance is not) corresponds to some 5 % or less of the total shear resistance at depths below 0.5 km. Since omitting cohesion means that lower shear resistance is modelled, it can be regarded a conservative assumption.

Since all the input parameters to the *CFS* calculation, with the exception of the pore pressure, were assumed to be distributed, the *CFS* calculations were carried out by means of Monte-Carlo simulations. For each input parameter and for each depth, N = 500,000 values were generated. The generation was set to follow the distribution that was determined for that particular parameter, i.e., the values of mean and variance were set based on the given uncertainty intervals, see e.g. Table 2-2 (the parameter distributions related to the glacial load are described in section 3.3.2). Then, the values were looped through and a corresponding array of *CFS* values was calculated using Eq. (3-1). Tests were made to ensure that the value of N gives a stable solution (Appendix 4).

In the deterministic geological modelling of the Forsmark site, the termination depth of deformation zones with surface trace lengths longer than 2.1 km are set at the base of the Forsmark regional model volume, which is -2.1 km a.s.l. (Hermanson and Petersson 2022). It is stated by Hermanson and Petersson (2022) that "the general principle is that a steeply dipping deformation zone should be modelled to a depth equal to the length of the zone's surface trace (z = 0)." This principle is here adopted schematically when evaluating zone stability. For the two longest deformation zones ZFMNW0017 and ZFMWNW0123, the stability is evaluated down to a depth of 5 km while the maximum depth of evaluation is set to 3 km for the other five zones (cf. Table 2-1).

This chapter is divided into two subsections. In the first subsection, results are presented from *CFS* calculations where only background stresses are applied, i.e., deformation zone stability was evaluated for present-day conditions. The second subsection presents *CFS* calculations where the stability was evaluated for conditions that may arise at the beginning or at the end of a period with glacial loading.

3.2 Present-day conditions

CFS was calculated for present-day conditions, i.e., when applying only the background stresses according to Eq. (2-1). For reference, *CFS* was also calculated when applying the background stress model that was adopted in the previous zone stability assessment by Fälth (2022) (applying most likely parameter values of deformation zone orientation, friction and $\sigma_{H,b}$ orientation, see Chapter 2).

The present-day *CFS* values are shown in Figure 3-1. The colour scale shows normalised probability density of *CFS*. The solid line indicates the most likely *CFS* value, and the dotted lines indicate the boundaries of the 95 % confidence interval. Based on the probability density distribution, the probability of *CFS*>0 was calculated (Figure 3-2). The following can be observed in Figure 3-1 and Figure 3-2:

- The parameter variation yields a considerable variation in *CFS* values at most depths, particularly for the steep zones (Figure 3-1). For these zones, the *CFS* variation may be ±50 % or more below 0.5 km depth. The uncertainty increases with depth. This is attributed to the increase in both stress level and deviatoric stress with depth. As these are increased, *CFS* becomes more sensitive to variations in coefficient of friction, zone orientation and stress orientation.
- For the gently dipping zone ZFMA2 the results indicate a high likelihood of instability under present-day conditions over a considerable depth range reaching down to more than 1 km depth (Figure 3-2). The probability of *CFS*>0 exceeds 0.2 down to 1 km depth.
- Despite the considerable variations in *CFS*, it appears that the steep zones all have considerable stability margins over a majority of their depth extents. The most likely *CFS* line reaches zero just at the surface for the northwest striking ZFMNW0017, ZFMNW1200, ZFMWNW0123 and ZFMWNW0809A (Figure 3-1). The 95 % confidence line crosses zero at 0.2 to 0.4 km depth in these cases. In the case with the northeast striking ZFMENE0060A and ZFMENE0062A, practically no instability is found at any depth. For all steep zones, the probability of *CFS*>0 under present-day conditions is practically zero at depths below 0.5 km (Figure 3-2).
- At depths below, say 0.5 km, there is a fairly reasonable agreement between the most likely values and the values obtained with the background stress model adopted by Fälth (2022) (Figure 3-1). Close to the surface, the most likely *CFS* values on the steep zones are higher than those based on the Fälth (2022) stress model while the opposite holds for ZFMA2. This can be explained by the fact that the horizontal stresses close to the surface are lower in the new background stress model used here (cf. Eq. (2-1) and Eq. (2-1) in Fälth (2022)).

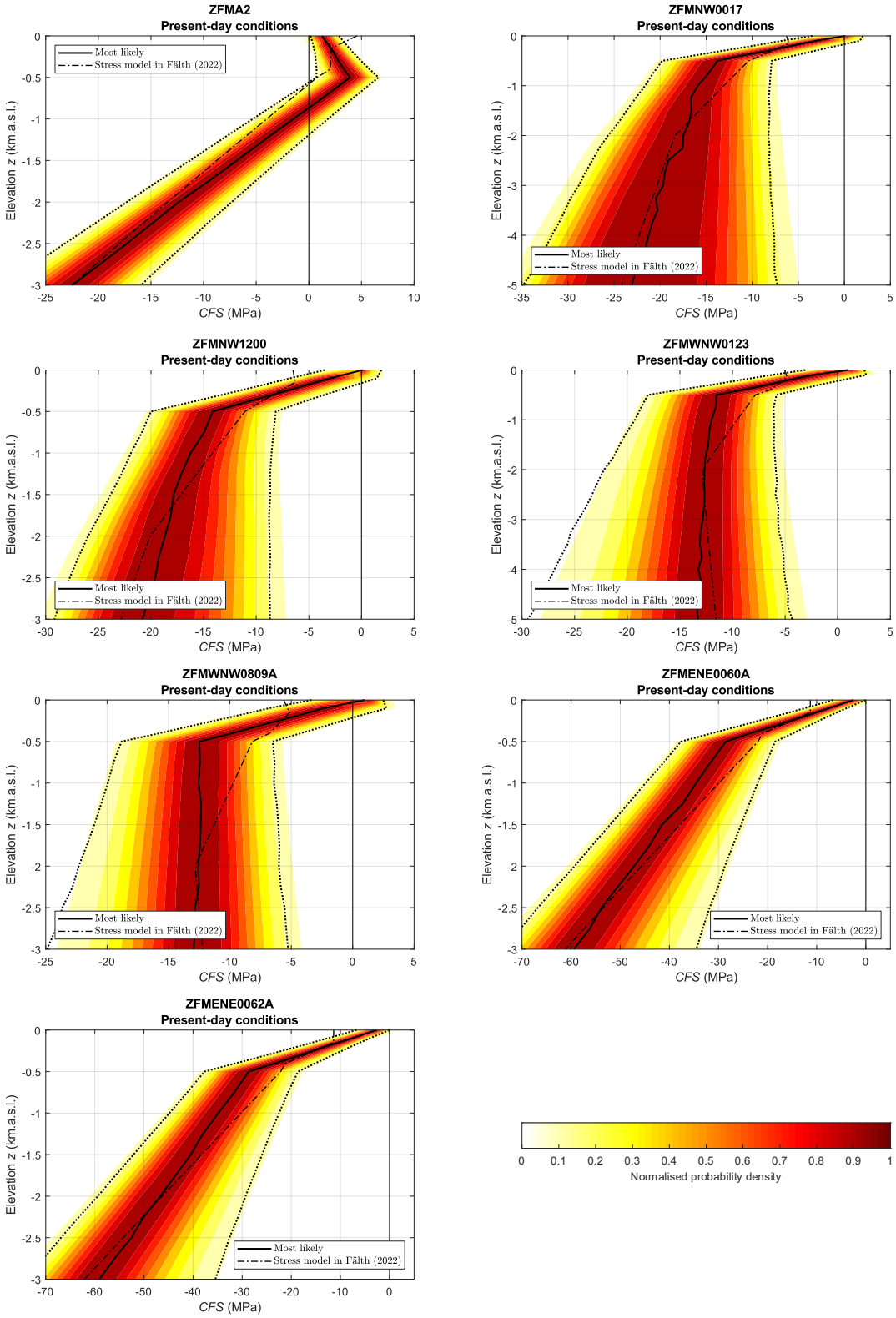

Figure 3-1. *CFS as function of depth for the seven Forsmark deformation zones under present-day conditions. The colour scale shows normalised probability density of CFS, and the dotted lines indicate the boundaries of the 95 % confidence interval. The solid line indicates the most likely CFS values. For reference, CFS values based on the background stress field adopted by Fälth (2022) are also plotted.*

The calculated instability at shallow depth on ZFMA2 (Figure 3-1, upper) could mean that the zone should be moving at present (seismically or aseismically). Alternatively, the generally high *CFS* levels at shallow depth on ZFMA2 may indicate that the horizontal stresses given by the background stress model applied here (Eq. (2-1)), as well as those given by the stress model used in Fälth (2022), are not fully compatible with the geometry of that zone. This may not necessarily mean that these stress models are wrong. The models were developed to be valid for the repository volume in the footwall of ZFMA2. Given that ZFMA2 is close to its stability limit, it may have moved previously. Such a movement would presumably relax stresses mainly in the hanging wall (see e.g. simulation results by Fälth 2022), and such potential effects are not accounted for in the present analysis.

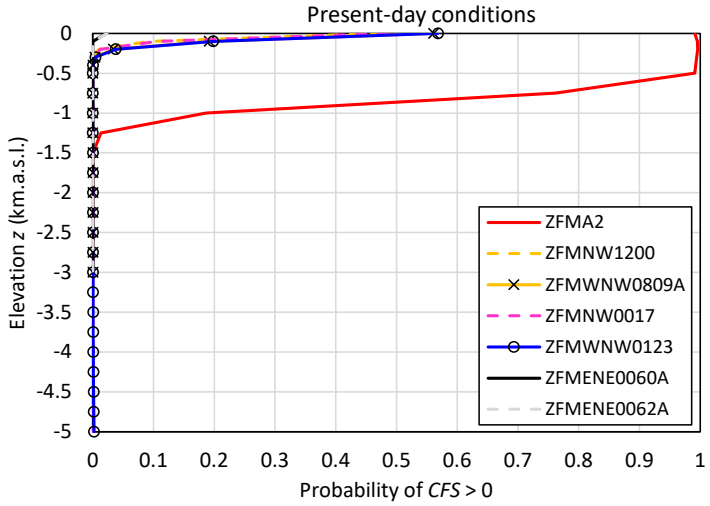

Figure 3-2. *Probability of CFS > 0 as function of depth for the seven Forsmark deformation zones under present-day conditions.*

3.3 Glacial loading

3.3.1 Temporal evolution of stability

Given the background stress field and an evolution of glacial stress additions, the temporal evolution of *CFS* can be calculated for a given zone/fracture orientation. Figure 3-3 and Figure 3-4 show the temporal evolution of *CFS* at 1.5 km depth on ZFMA2 and ZFMNW0017 for the five ice models (*CFS* evolutions for all deformation zones and ice models are presented in Appendix 3). Each ice model has been combined with the five Earth models. In the calculation, the most likely background stress field according to Eq. (2-1) was applied with the trend of $\sigma_{H,b}$ set to N145°E and the coefficient of friction set to $\mu = 0.7$. The diagrams also show the evolution of the vertical ice load, which indicates the periods with ice cover (cf. Figure 2-3 and Figure 2-4).

The diagrams in Figure 3-3 show that, on a gently dipping zone as ZFMA2, the lowest stability typically develops at the end of a glacial period. This is due to the excess in horizontal stress that remains after ice retreat (cf. section 0). The two models of the Weichselian and Saalian glaciations (Figure 3-3, upper), which simulate the largest and thickest of the ice sheets considered here, give the strongest stress effects (compare Figure 2-3 and Figure 2-4). The three projections of future glaciations, as depicted in this study, have weaker or almost negligible impact on fault stability. It can also be noted that while the *CFS* levels differ for the different Earth models, the results tend to be qualitatively similar.

Similarly, Figure 3-4 shows temporal evolution of *CFS* at 1.5 km depth on ZFMNW0017. This zone, which is steeply dipping, typically becomes destabilised at the beginning of a glacial period when the ice sheet approaches the site. This is due to the reduction of horizontal stresses in the forebulge outside the ice margin (cf. section 0). The UMISM and NH40 ice models give the strongest stress effects, as in the case with ZFMA2 (Figure 3-3).

Figure 3-5 shows the temporal evolution of *CFS* on the remaining five deformation zones for the NH40 ice model. It can be noted that the *CFS* evolution on ZFMNW1200 and on ZFMNW0017 are similar (compare Figure 3-5, top and Figure 3-4, top right) due to the similar orientations of these zones (cf. Table 2-1). Likewise, ZFMWNW0123 and ZFMWNW0809A (Figure 3-5, middle) have

similar orientations and thus similar *CFS* evolutions. The *CFS* histories of the two zones ZFMENE0060A and ZFMENE0062A are shown in Figure 3-5, bottom. What is notable in these diagrams is that these latter zones have very considerable stability margins. This is because they dip along directions sub-parallel with the background major horizontal stress $\sigma_{H,b}$ and hence are subjected to low shear stresses and high compressive stresses.

The results presented here give an overview and show how the stability of differently oriented zones develop during different periods of a glacial cycle. Furthermore, the results show which of the glaciation scenarios have the strongest impact on deformation zone stability.

The *CFS* values shown in this section were calculated at one depth and for the most likely background stress field (Eq. (2-1)). However, the stability tends to vary with depth, as shown in Figure 3-1. In addition, as indicated in Table 2-2, there are uncertainties in the magnitudes and orientations of the components in the background stress field as well as in the orientations of the deformation zones.

In next subsection, results are presented from calculations where zone stability was evaluated at different depths while considering the uncertainties in the background stress field, the orientations and property of the deformation zones as well as uncertainties in the glacial stresses.

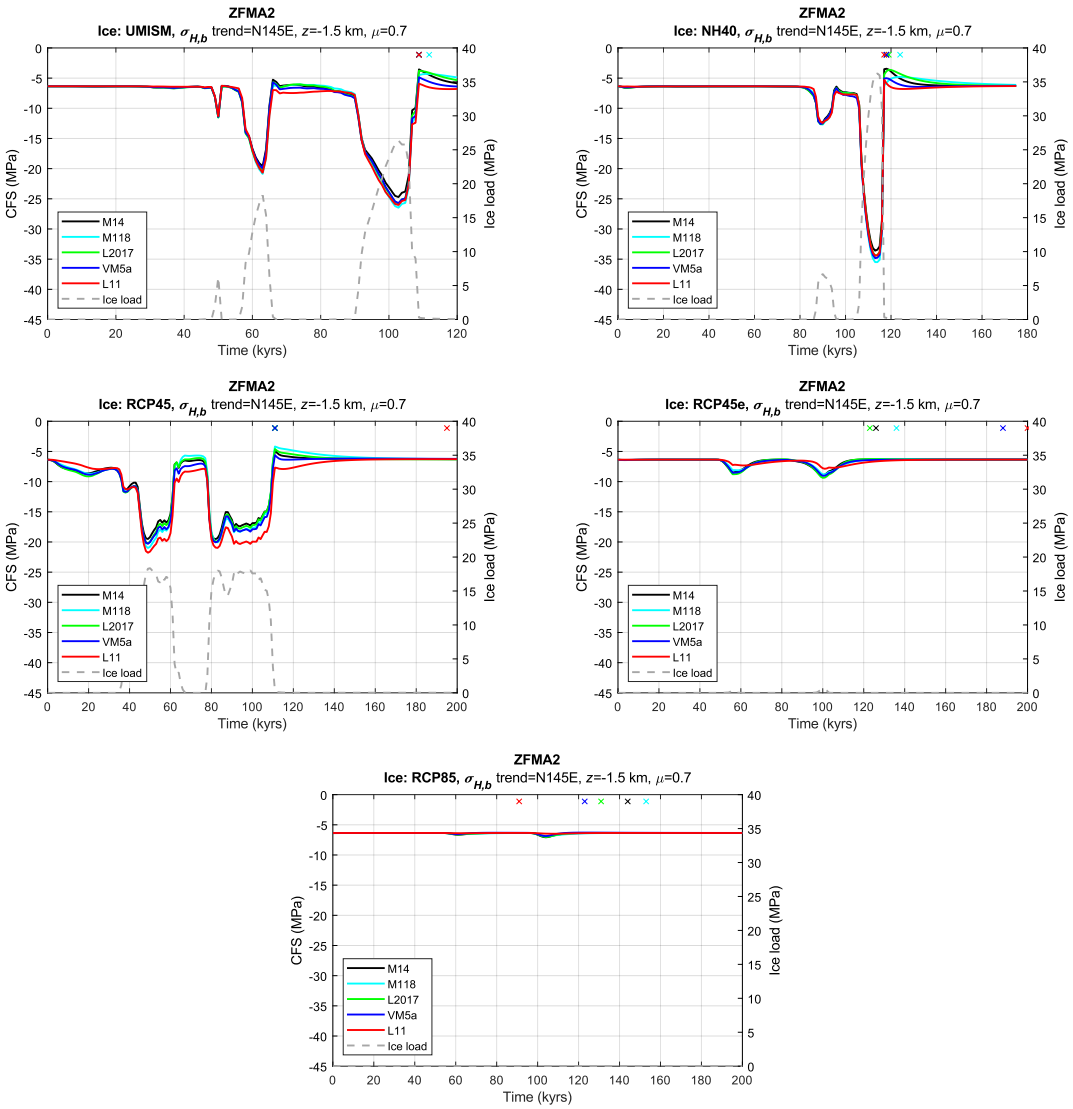

Figure 3-3. *Temporal evolutions of CFS at 1.5 km depth on ZFMA2 for the five different ice models plotted along with the vertical ice load. Each ice model is combined with the five Earth models. The coloured crosses indicate, for each Earth model, the time instance of max CFS. CFS evolutions for all deformation zones and ice models are presented in Appendix 3.*

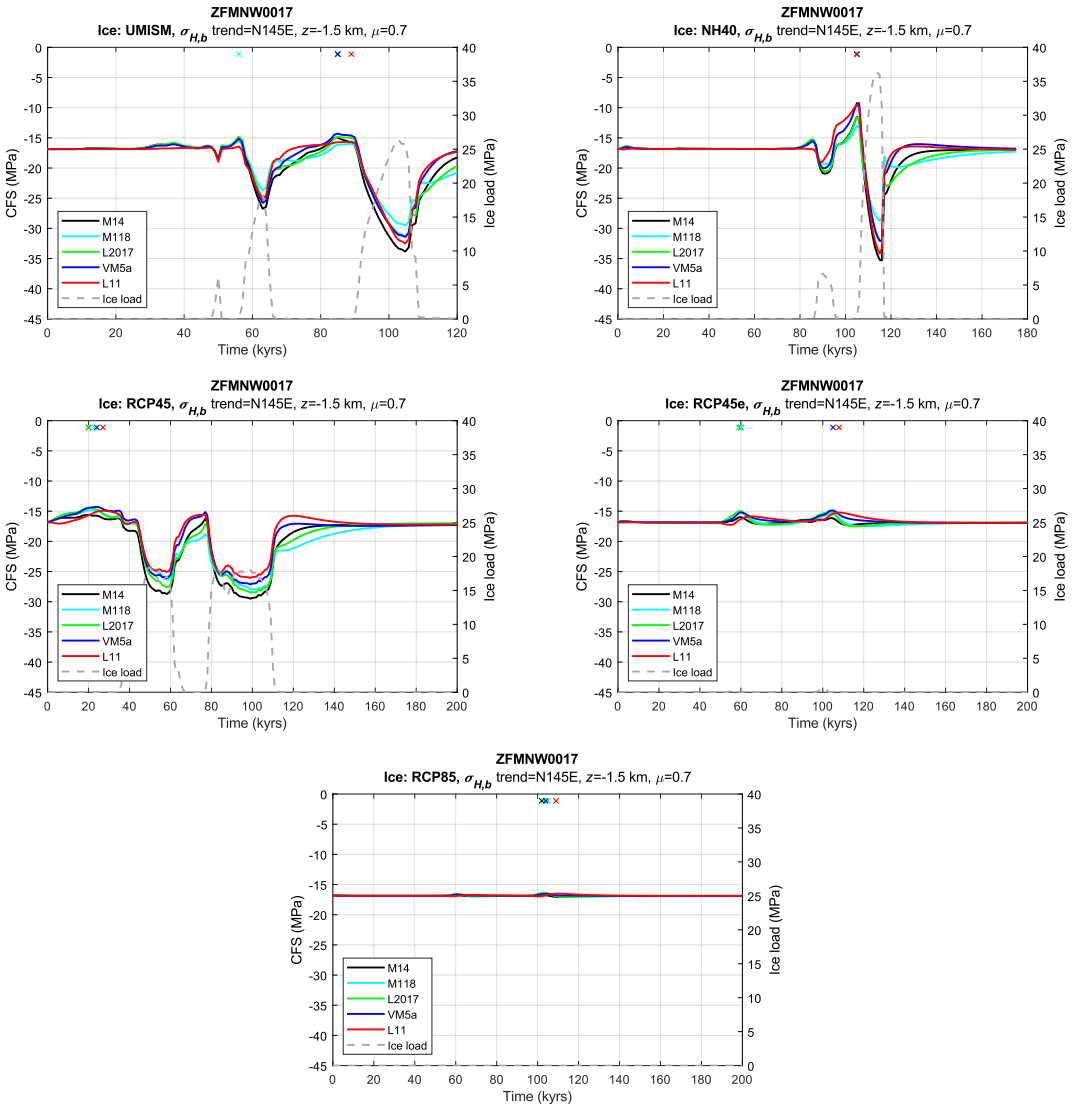

Figure 3-4. *Temporal evolutions of CFS at 1.5 km depth on ZFMNW0017 for the five different ice models plotted along with the vertical ice load. Each ice model is combined with the five Earth models. The coloured crosses indicate, for each Earth model, the time instance of max CFS. CFS evolutions for all deformation zones and ice models are presented in Appendix 3.*

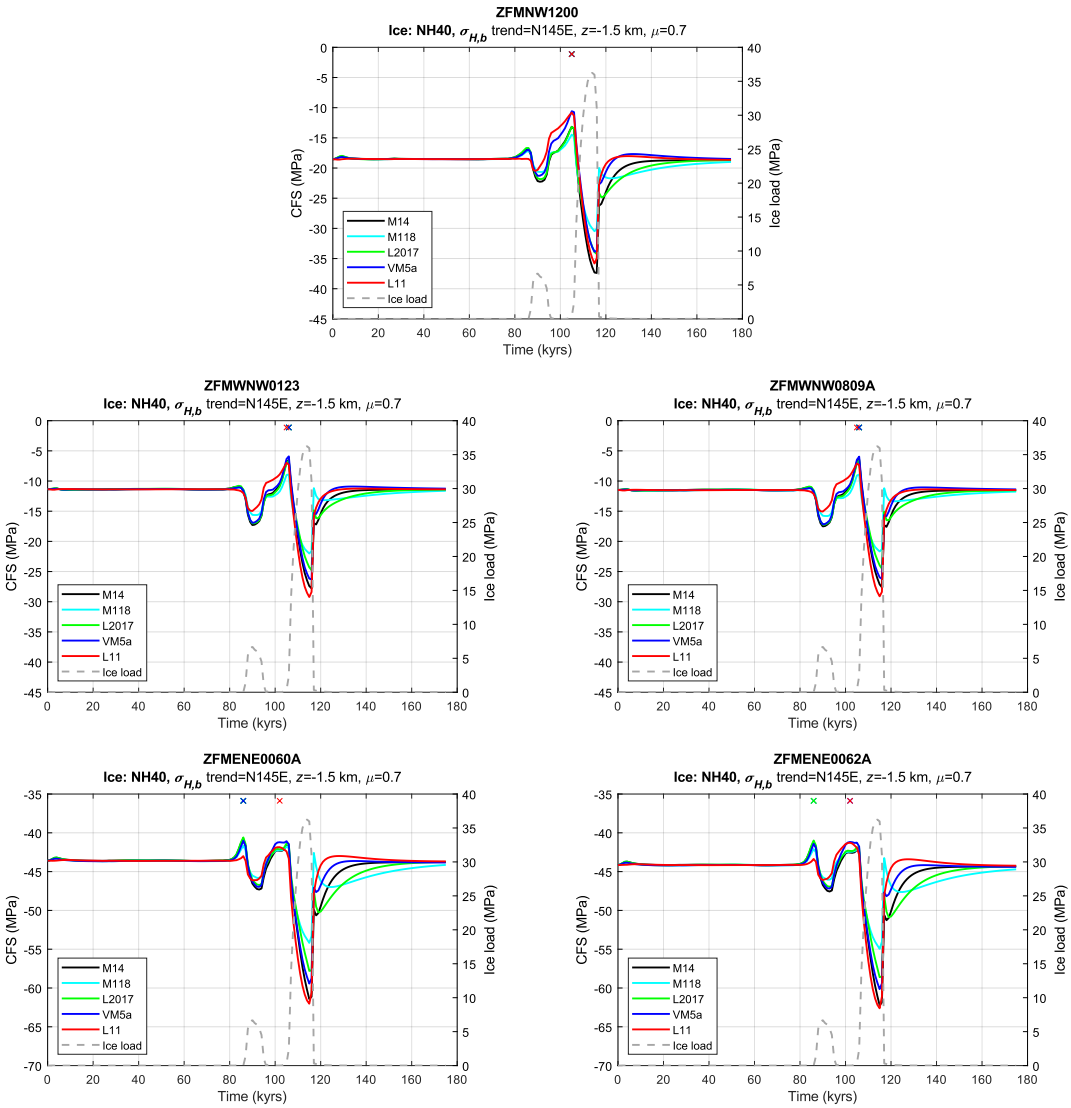

Figure 3-5. *Temporal evolutions of CFS at 1.5 km depth on ZFMNW1200, ZFMWNW0123, ZFMWNW0809A, ZFMENE0060A and ZFMENE0062A for the NH40 ice model plotted along with the vertical ice load. The ice model is combined with the five Earth models. The coloured crosses indicate, for each Earth model, the time instance of max CFS. Note the different CFS y-scale for the lower plots. CFS evolutions for all deformation zones and ice models are presented in Appendix 3.*

3.3.2 Stability under forebulge and endglacial conditions

The ice/Earth model combinations considered here represent a wide range of glacial stress addition scenarios. It is assumed here that the ranges of stress magnitudes and stress orientations included in this GIA data set can be considered relevant for the additional loading of the bedrock in Forsmark that potentially can be expected during future glaciations.

As showed by the results presented in section 3.3.1, the glacial stresses vary during a glacial cycle and lead to reduced stability at different times for differently oriented deformation zones. Using the GIA data set as input, calculations were carried out in order to determine the characteristics (i.e., the magnitudes and orientations) of the glacial stresses at the stages (time instances) when they tend to give instability of the Forsmark deformation zones. By compiling the glacial stresses at these critical stages, the ranges of magnitudes and orientations of these critical glacial stresses were determined (Table 3-1). The ranges were considered representative for potential glacial loads at Forsmark under forebulge and endglacial conditions and were used to define the glacial stress distributions as input to the Monte-Carlo simulations for determining deformation zone stability. Hence, the GIA results were not used directly as input to the *CFS* calculations but rather served as a reference when determining plausible input parameter values to the calculations.

The approach applied here means that the calculated probability is that of having unstable conditions under forebulge conditions or under endglacial conditions, given that there actually is a period with glacial load at Forsmark.

The exploration of the glacial stress characteristics is presented in the following subsection. After that follows a subsection where the results of the Monte-Carlo simulations are presented.

Exploring glacial stress characteristics

To explore the ranges of glacial stress magnitudes and orientations at the times when the Forsmark deformation zones may become unstable, the temporal evolution of *CFS* was calculated for all seven zones according to the following:

- All 25 original ice/Earth model combinations were tested. In addition, the 9 scenarios with 25,000 years extended ice residence time (+25k) at glacial maximum were also included (cf. discussion in section 2.3.2).
- For each of the 34 ice/Earth model combinations above, at each time instance during the glacial evolution, *CFS* was calculated at six depths, 0.2 km, 0.5 km, 1.5 km, 2.5 km 3.5 km and 4.5 km. The depths in the range 0.5 km to 4.5 km are depths at which GIA stresses were available as input from the simulations by Schmidt and Lund (2025). The 0.5 km GIA stresses were applied also at 0.2 km depth, which was considered a reasonable assumption because of the low depth gradient in these stresses.
- The most likely background stresses according to Eq. (2-1) were applied.
- For all ice/Earth model combinations and for all six depths, three background stress orientations were tested: N125°E, N145°E and N165°E.
- The coefficient of friction was assumed to be $\mu = 0.7$.

Given the background stress model applied here and the assumed coefficient of friction, *CFS* may be positive on parts of a deformation zone even before any glacial stresses have been added. This is typically the case for the uppermost parts of the shallow and gently dipping ZFMA2, as shown in Figure 3-1 (top).

Since unstable conditions were found initially at some locations, the time instances when the glacial loading leads to instability on a zone was determined according to the following. At each elevation z, a reference value $CFS_{ref}(z)$ was determined based on the initial *CFS* value $CFS_{ini}(z) = CFS(t{=}0, z)$ according to

$$CFS_{ref}(z) = \begin{cases} 0 + 0.2 \text{ MPa}, & CFS_{ini}(z) \leq 0 \\ CFS_{ini}(z) + 0.2 \text{ MPa}, & CFS_{ini}(z) > 0 \end{cases}. \quad (3\text{-}2)$$

During glacial loading, a deformation zone was marked as unstable if *CFS* exceeded CFS_{ref} at any depth, i.e. if $\Delta CFS(z) = CFS(t, z) - CFS_{ref}(z) > 0$. The 0.2 MPa term in Eq. (3-2) was added to avoid a deformation zone to be marked as unstable because of tiny irrelevant fluctuations in the GIA stresses that were caused by numerical "noise" in the GIA calculations. According to the chosen reference *CFS* value, an initially unstable zone (with *CFS* = 0.2 MPa) is assumed to be at the stability limit, such that any further increase of *CFS* causes instability. As a deformation zone was marked as unstable, the current glacial stress magnitudes and orientations were saved along with the current ΔCFS values on the zone.

The evolution of glacial vertical load for the ice models that yielded unstable conditions on ZFMA2 are plotted in Figure 3-6 along with markers that indicate maximum ΔCFS values and corresponding time instances for the cases where instability was found. Note that no results for the ice models RCP45e or RCP85 are included in Figure 3-6 since those ice models did not result in instability on ZFMA2 for any case. Similar to what is indicated in Figure 3-3, the results in Figure 3-6 show that ZFMA2 will become unstable during endglacial conditions as the ice retreats. For a gently dipping zone like ZFMA2, the ratio between the vertical and horizontal stress is of significant importance for the stability of the zone. It can be noted in Figure 3-6 though, that the ice load (vertical stress) was zero, or close to zero, at practically all the instances when instability was found. The ice load exceeded 0.5 MPa only by way of exception for these instances. Hence, the vertical glacial stress was not considered in the further handling or in the *CFS* calculations presented below.

The corresponding results for ZFMNW0017, ZFMNW1200, ZFMWNW0123 and ZFMWNW0809A are shown in Figure 3-7. For these zones, the NH40 and NH40+25k ice models yielded positive ΔCFS values. The results confirm that the steeply dipping zones tend to become unstable under forebulge stress conditions. No positive ΔCFS values were found on ZFMENE0060A or ZFMENE0062A.

The magnitudes, the stress ratios and trends of the glacial horizontal stress components are summarised in Figure 3-8 for all cases that gave instability on ZFMA2 (cf. Figure 3-6). The results show that the major horizontal glacial stress addition $\sigma_{H,g}$ under endglacial conditions may be in the range 0 to 20 MPa and the minor horizontal stress addition $\sigma_{h,g}$ in the range 0 to 15 MPa. The variation of stress magnitudes with depth is negligible. The ratio $\sigma_{H,g}$ / $\sigma_{h,g}$ is mainly in the range 1 to 4, with the highest ΔCFS values and the greatest depth extent of instability obtained for ratios in the range 1 to approximately 1.5. This stress ratio range corresponds to $\sigma_{H,g}$ approximately in the range 15 MPa to 20 MPa and with $\sigma_{h,g}$ 15 MPa.

In a few cases, $\sigma_{h,g}$ is negative, giving negative ratios. There were also very high irrelevant ratios (>5) caused by tiny $\sigma_{h,g}$ values. These high ratios were set to zero in the plot. The negative stress values and the highest ratios were neglected in the further analysis. The $\sigma_{H,g}$ trend falls in the range 0 to 175°. In most of the cases, the variation in trend with depth is small. Significant changes in trend with depth take place only by way of exception. Finally, it can be concluded that the highest ΔCFS values and the largest depth extent of instability arise when the stress additions are at their highest. The lowest stability is consistently found close to the ground surface.

The glacial stresses for the cases that gave instability on the steep zones (cf. Figure 3-7) are summarised in Figure 3-9 to Figure 3-12. The results indicate that the major glacial stress $\sigma_{H,g}$ may be in the range -5 to 0 MPa while the minor stress component $\sigma_{h,g}$ is in the range -11 to -5 MPa. The stress ratio $\sigma_{H,g}$ / $\sigma_{h,g}$ is in the range 0 to 0.7. There is a group of cases with stress trends below N25°E and another group with trends above N150°E. In the continued analysis, the trend is taken to vary in the two ranges 0 to N50°E and N150°E to N175°E. The lower range is extended up to N50°E even though the data in Figure 3-9 to Figure 3-12 indicate trends only up to N25°E. This means that there is some coverage for the case with the RCP45e+25k ice model (see next paragraph). As for the ZFMA2 results in Figure 3-8, the variation of the stress components with depth is modest.

It can be noted that the RCP45e+25k ice model (with extended ice residence time), gives forebulge stresses on par with those generated by the NH40 ice model (compare Figure 3-9 to Figure 3-12 with Figure 3-13). However, because of the $\sigma_{H,g}$ trend, the RCP45e+25k model did not yield any zone instability. Note in Figure 3-13 though, that the $\sigma_{H,g}$ trend at the time of minimum $\sigma_{h,g}$ and $\sigma_{H,g}$ is about N50°E for two of the Earth models, which is within the ranges that will be considered in the continued work (see previous paragraph).

In the continued work presented below, the magnitudes and orientations of the glacial stresses were varied within ranges based on the observations made here. The magnitudes and orientations of these stresses were assumed to be constant with depth.

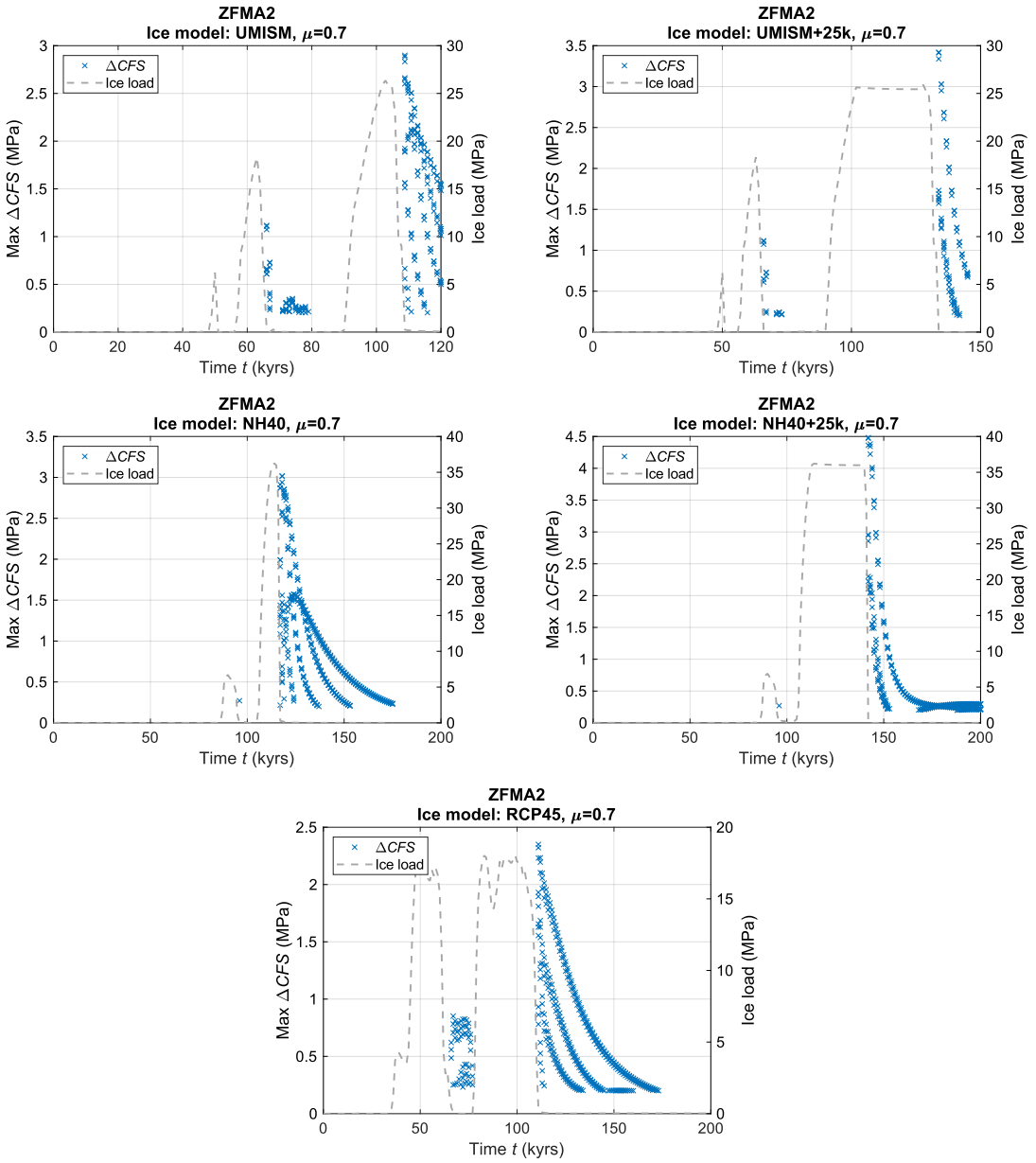

Figure 3-6. *Temporal evolution of ice load for the ice models that yielded unstable conditions on ZFMA2. The markers indicate maximum ΔCFS on the zone at the time instances when CFS_{ref} is exceeded at any depth. Note that combinations of all five Earth models and all three background stress orientations were considered when generating the results. Note that the vertical scale varies between plots.*

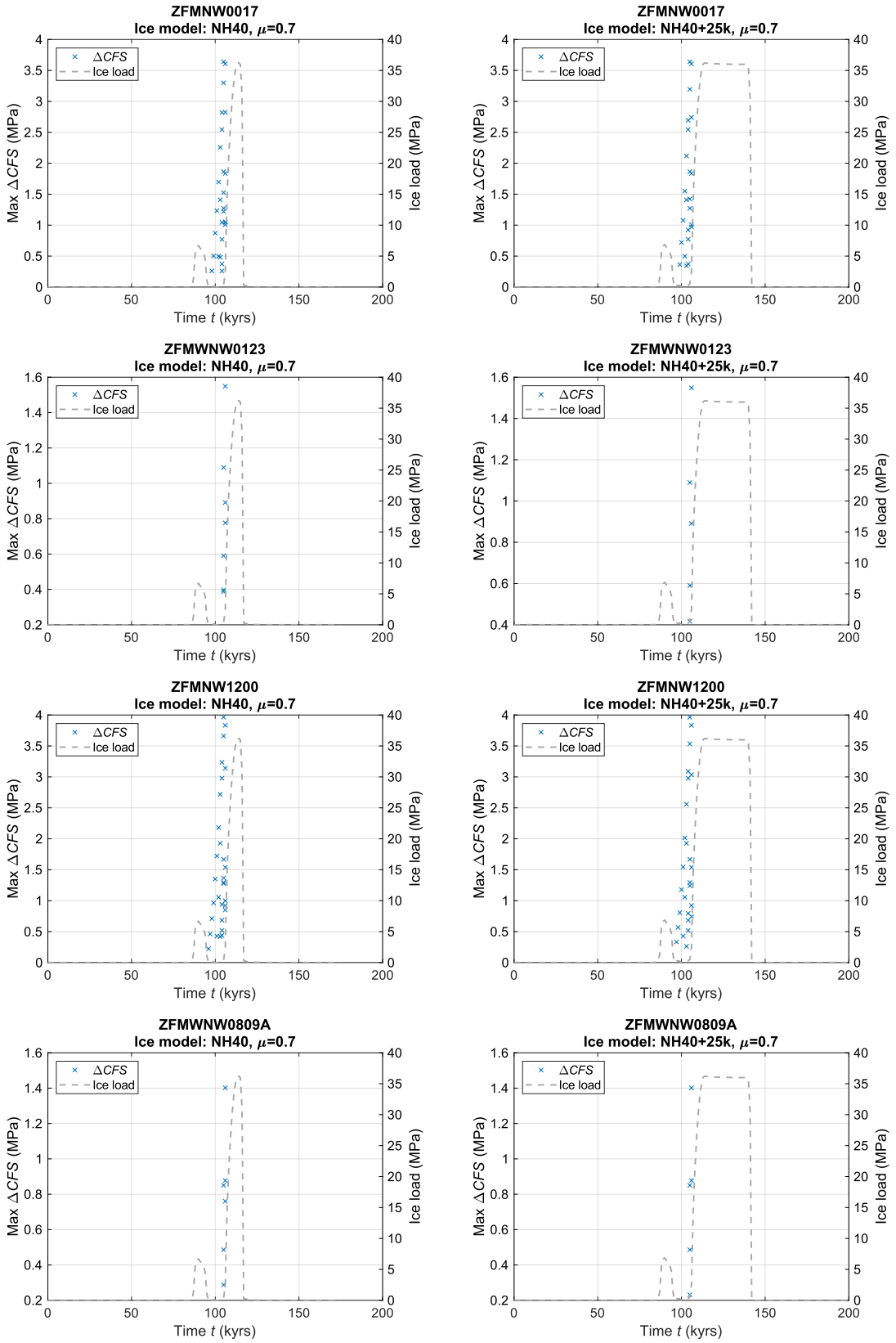

Figure 3-7. *Temporal evolution of ice load for the NH40 and NH40+25k ice models, which are the ice models that gave unstable conditions on ZFMNW0017, ZFMNW1200, ZFMWNW0123 and ZFMWNW0809A. The markers indicate maximum ΔCFS on the zones at the time instances when CFS_{ref} is exceeded at any depth. Note that combinations of all five Earth models and all three background stress orientations were considered when generating the results. Note that the vertical scale varies between plots.*

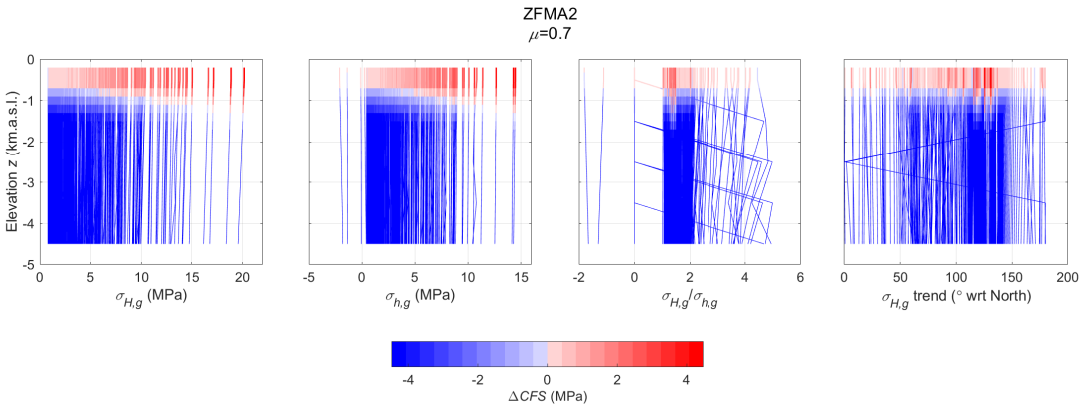

Figure 3-8. *Magnitudes, stress ratios and trends of the glacial stresses as function of depth for all time instances when ZFMA2 was marked as unstable, cf. Figure 3-6. Note that results for all five ice models depicted in Figure 3-6 are included here. Values of $\sigma_{H,g}$ / $\sigma_{h,g}$ higher than 5 were set to zero in the plot. The line colour indicates ΔCFS. The lower limit of the colour scale is limited to make the plots clearer.*

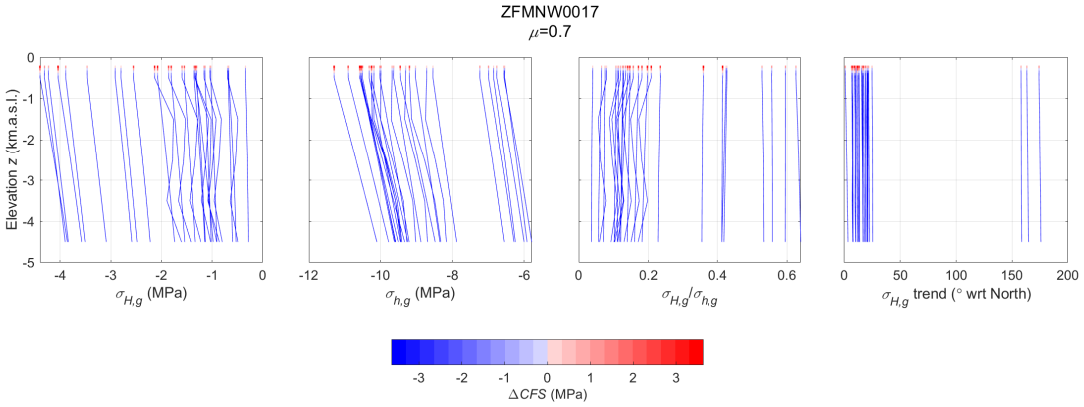

Figure 3-9. *Magnitudes, stress ratios and trends of the glacial stresses as function of depth for all time instances when ZFMNW0017 was marked as unstable, cf. Figure 3-7. Note that results for both ice models depicted in Figure 3-7 are included here. The line colour indicates ΔCFS. Note that the lower limit of the colour scale is limited to make the plot clearer.*

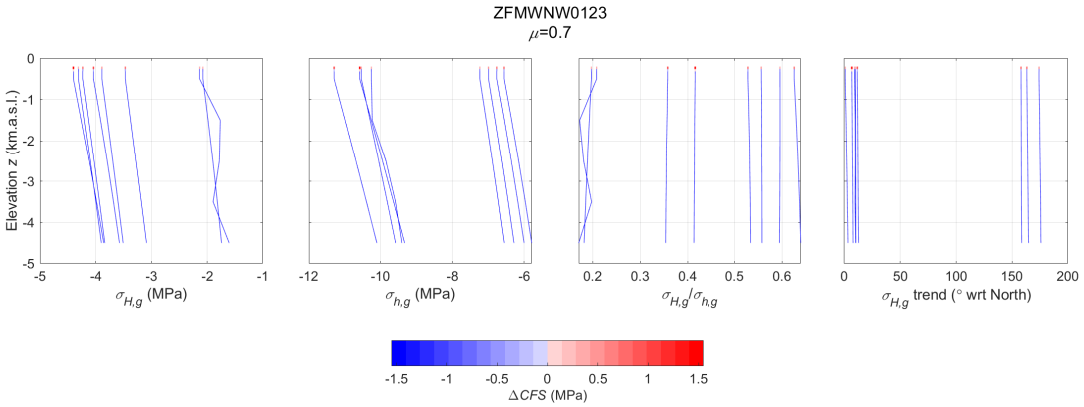

Figure 3-10. *Magnitudes, stress ratios and trends of the glacial stresses as function of depth for all time instances when ZFMWNW0123 was marked as unstable, cf. Figure 3-7. Note that results for both ice models depicted in Figure 3-7 are included here. The line colour indicates ΔCFS. Note that the lower limit of the colour scale is limited to make the plot clearer.*

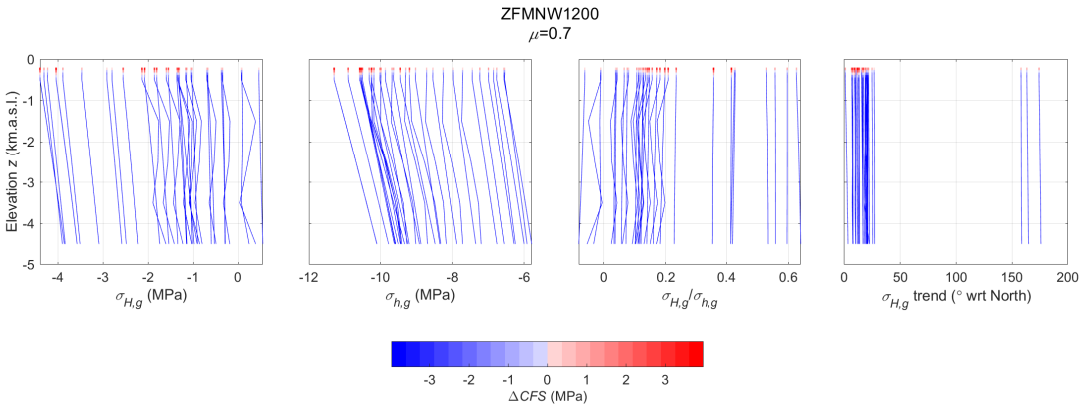

Figure 3-11. *Magnitudes, stress ratios and trends of the glacial stresses as function of depth for all time instances when ZFMNW1200 was marked as unstable, cf. Figure 3-7. Note that results for both ice models depicted in Figure 3-7 are included here. The line colour indicates ΔCFS. Note that the lower limit of the colour scale is limited to make the plot clearer.*

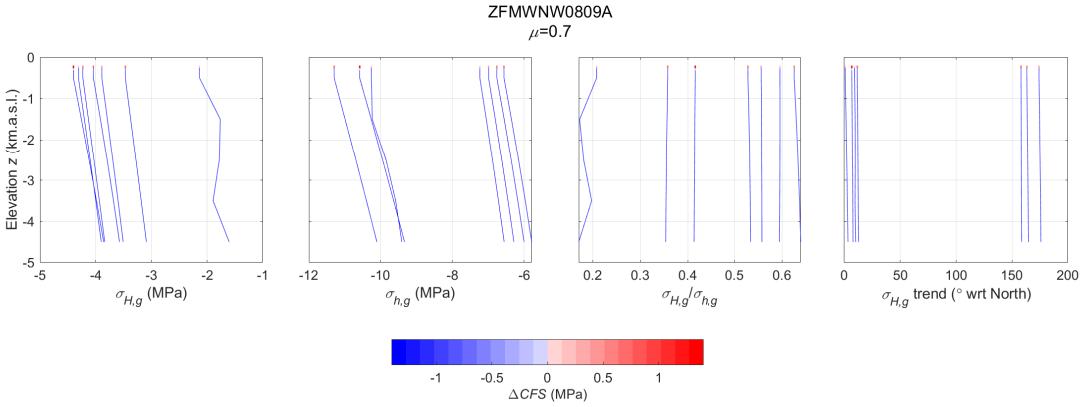

Figure 3-12. *Magnitudes, stress ratios and trends of the glacial stresses as function of depth for all time instances when ZFMWNW0809A was marked as unstable, cf. Figure 3-7. Note that results for both ice models depicted in Figure 3-7 are included here. The line colour indicates ΔCFS. Note that the lower limit of the colour scale is limited to make the plot clearer.*

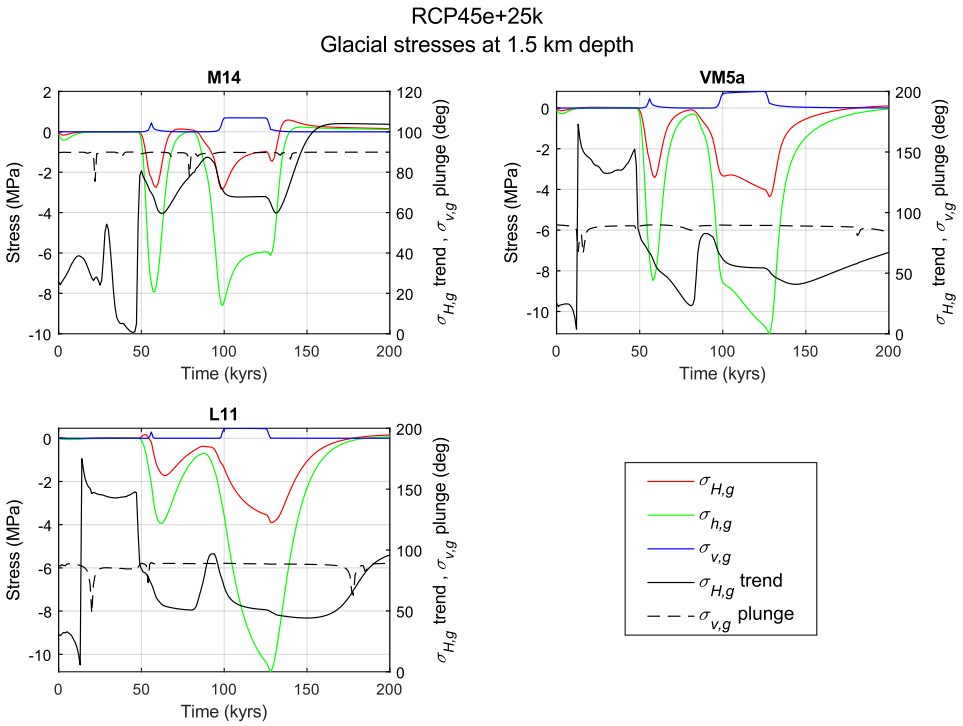

Figure 3-13. *Time evolutions at 1.5 km depth of $\sigma_{H,g}$, $\sigma_{h,g}$, $\sigma_{v,g}$, $\sigma_{H,g}$ trend and $\sigma_{v,g}$ plunge for the RCP45e ice model with 25,000 years extended ice residence time (+25k). This plot is also presented in Figure 8-8 in Appendix 2.*

Applying parameter distributions

Here, results from Monte-Carlo simulations of deformation zone stability under glacial conditions are presented. In the calculations, distributions of the background stress field parameters, of the deformation zone orientations and friction, as well as of the glacial stress parameters were considered. The parameter values related to the background stress field, as well as the deformation zone orientations and friction are presented in Table 2-2. The background stress parameters, the deformation zone orientations and friction, which are based on measurements and observations, were given normal distributions around reported most likely values.

The glacial stress parameters are summarised in Table 3-1. The parameters were varied independently within ranges that were based on the observations presented in the previous subsection. Note that the magnitudes of $\sigma_{H,g}$ and $\sigma_{h,g}$ were handled as independent parameters even though each magnitude pair in the GIA data corresponds to a specific stress ratio. However, the stress magnitude ranges considered here means that the most critical ratios, i.e., those giving the highest *CFS* values and the largest extent with instability as depicted in Figure 3-8 to Figure 3-12, were covered. Increasing the range of stress magnitudes, and hence the range of stress ratios, could possibly give a yet larger spread in the *CFS* results and an increase in the calculated probability of *CFS*>0. However, this is not necessarily true. As seen in Figure 3-8, higher stability is associated with lower stresses in the endglacial case. Hence, extending the ranges for the magnitudes of $\sigma_{H,g}$ and $\sigma_{h,g}$ in this case such that they include also lower stresses close to zero (cf. Table 3-1 and Figure 3-8) would give a slight reduction of the estimated probability of *CFS*>0.

The fact that the stress magnitudes and the stress orientation were assumed to be independent parameters, stress configurations that are not present in the GIA catalogue may be introduced. This may not necessarily mean that such stress configurations are unrealistic; the GIA catalogue data is generated by models that include the most prominent characteristics of potential glacial loads and of the crust/mantle system, but, as for all models, all details of reality are not covered. At any rate, since the assumption of independent parameters may create "outlier stress configurations", it should promote a larger spread in the simulated distribution of *CFS* values and possibly more pessimistic results, i.e., an increase in the estimated probability of zone instability.

Since probabilities of future glacial loads with different characteristics are unknown, it is difficult to determine most likely parameter values for the glacial stress input. Hence, the glacial stress parameters in Table 3-1 were assumed to have uniform probability distributions. Examples of these distributions are shown in Figure 7-4 in Appendix 1.

In accordance with the observations made above, glacial stresses typically associated with forebulge conditions were applied when the stability of the steep deformation zones was evaluated while typical endglacial stresses were applied when evaluating the stability of the gently dipping ZFMA2.

Table 3-1. Glacial stress parameter values

Parameter	Symbol	Values/range	
		Forebulge	Endglacial
Glacial major horizontal stress	$\sigma_{H,g}$	[-5 0] MPa	[15 20] MPa
Glacial minor horizontal stress	$\sigma_{h,g}$	[-11 -5] MPa	[10 15] MPa
Glacial major horizontal stress trend	-	[0 N50°E], [N150°E N175°E]	[0 N175°E]

Figure 3-14 shows *CFS* as function of depth for all seven deformation zones. The colour scale shows normalised probability density of *CFS*. The solid line indicates the most likely *CFS* value, and the dotted lines indicate the boundaries of the 95 % confidence interval.

For reference, the plots in Figure 3-14 also show two sets of *CFS* values calculated while applying the background stresses and the glacial stresses used in the stability assessment by Fälth (2022) (applying most likely parameter values of deformation zone orientation and friction, see Chapter 2). The two sets of *CFS* values correspond to (1) a base case with most likely background stresses and (2) a case where the minor horizontal background stress is reduced at depths above 2 km. The reduction was 11 % at 0.5 km depth, which corresponds to $\sigma_{H,b} / \sigma_{h,b} = 2$ at this depth. At the other depths above 2 km, the reduction was proportional to the reduction at 0.5 km depth (see Fälth (2022) for further details). Three background stress trends (N125°E, N145°E, N165°E) were tested by Fälth (2022). For each zone, the reference *CFS* results presented here were generated by applying the stress trend giving the lowest stability on that particular zone (see Fälth (2022)). The ZFMA2 zone was not included in that study. Here, background stress trend N165°E and endglacial stresses from the glacial scenario considered by Fälth (2022) were applied for that zone when generating the reference *CFS* results.

Given the probability density distributions of *CFS* depicted in Figure 3-14, the probability of having $CFS > 0$ was determined for each deformation zone. These results are shown in Figure 3-15. The following can be observed in Figure 3-14 and Figure 3-15:

- On ZFMA2 (endglacial conditions), the most likely *CFS* line indicates positive *CFS* values down to about 1.2 km depth. This is an increase from about 0.8 km depth as given by the Fälth (2022) stress model. The higher *CFS* values given by the present results can primarily be attributed to the higher horizontal stresses in the new background stress model (Figure 3-14). The probability of unstable conditions exceeds 0.2 down to about 1.4 km depth (Figure 3-15).
- The most likely *CFS* values of the steep zones (under forebulge conditions) indicate considerable stability margins over a majority of their depth ranges. The most likely values are on par or lower than the values obtained by Fälth (2022) (Figure 3-14). The diagram in Figure 3-15 shows that there is a non-zero probability of $CFS>0$ at all depths on the northwest striking ZFMNW0017, ZFMNW1200, ZFMWNW0123 and ZFMWNW0809A. However, the probability at depths below 0.5 km is low and is in the range 0.01-0.04. On the northeast striking ZFMENE0060A and ZFMENE0062A, the stability margins are high. At depths below 0.3 km, the probability of $CFS>0$ is practically zero.
- As for the case with present-day conditions, there is a considerable spread in the *CFS* values (compare Figure 3-1 and Figure 3-14), particularly for the steep zones, which are highly sensitive to variations in deformation zone strike and stress orientation.

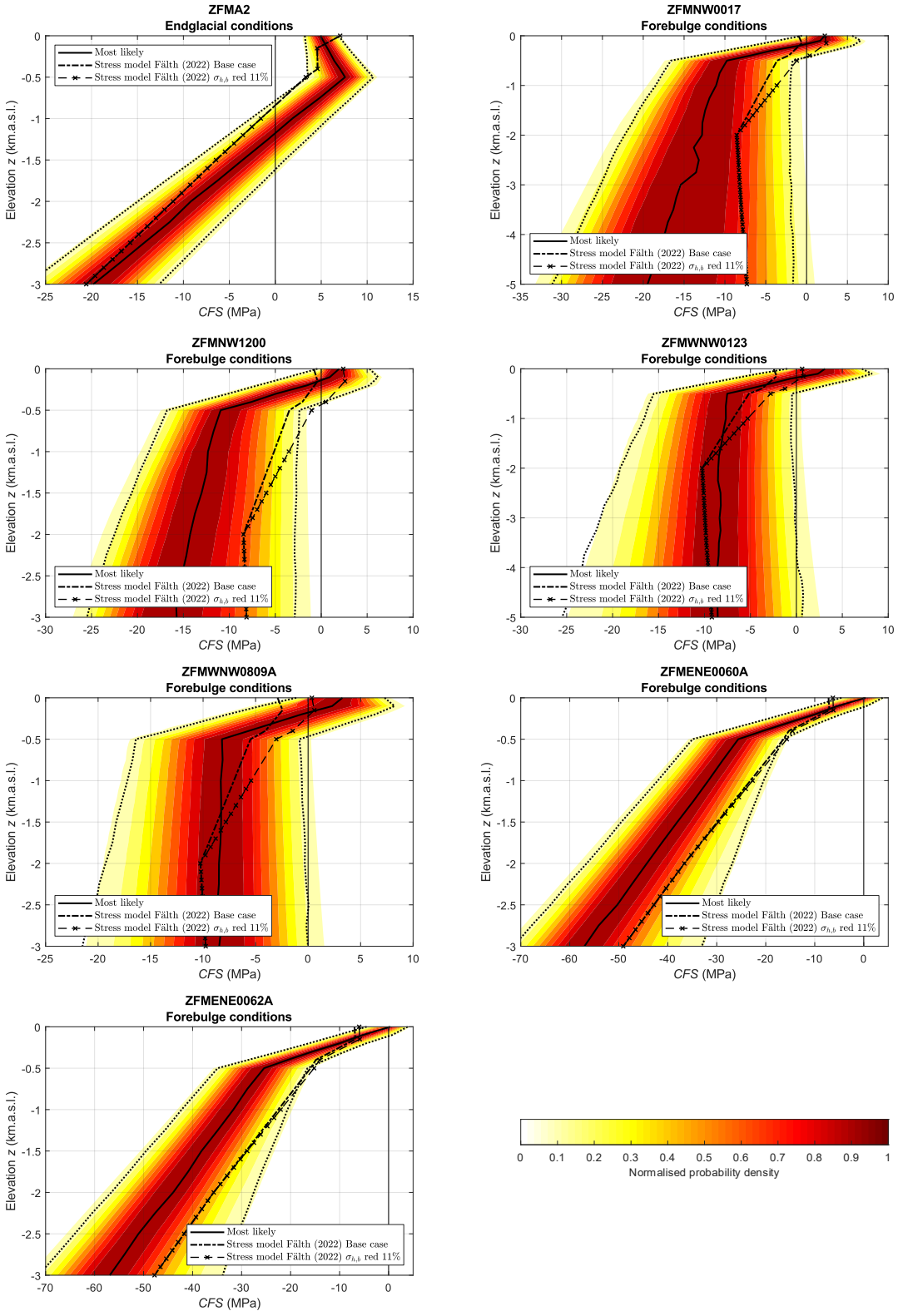

Figure 3-14. *CFS as function of depth for the ZFMA2 zone under endglacial conditions and for the six steep zones under forebulge conditions. The colour scale shows normalised probability density of CFS, and the dotted lines indicate the boundaries of the 95 % confidence interval. The solid line indicates the most likely CFS values. For reference, CFS values based on the input stresses used in the stability estimates by Fälth (2022) are also plotted.*

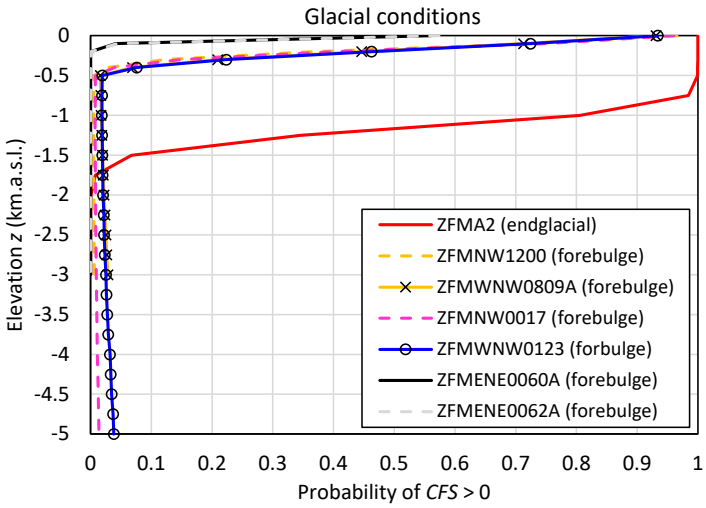

Figure 3-15. *Probability of CFS > 0 as function of depth for the ZFMA2 zone under endglacial conditions and for the six steep zones under forebulge conditions.*

3.4 Sensitivity analyses

In the following three subsections, the sensitivity in the results to different variations in input is examined.

3.4.1 Impact of excess pore water pressure P_e

Due to the considerable thickness of an ice sheet, its long duration, and the generation of glacial melt water, considerable pore water pressures may develop in the bedrock beneath the ice (e.g. Castro-Vera et al. 2025, Lönnqvist and Hökmark 2013). An increase in pore water pressure will reduce the effective normal stress and lead to reduced deformation zone stability (Eq. (3-1)).

The magnitude of the pore water excess pressure P_e and its spatial distribution are uncertain, though. Hökmark et al. (2010) considered the possibility that excess pore pressures would develop in the crust in front of an advancing ice sheet due to the presence of an impermeable permafrost layer extending outside the ice margin. They also considered the case of excess pore pressures remaining in the crust after ice retreat at the end of glaciation. They based their assumptions on numerical and analytical models presented in Lönnqvist and Hökmark (2013).

Here, when examining the potential effect of excess pore pressure, the assumptions, in general, follow those made by Hökmark et al. (2010). Their models for excess pressure extended down to 1 km depth. Here, their assumptions are, with some modifications, extended to larger depths (Figure 3-16).

For the forebulge situation, it is assumed that the excess pore pressure is 3.3 MPa at all depths. This is the same pressure as that assumed by Hökmark et al. (2010). For the endglacial stage, the model of Hökmark et al. (2010) was based on numerical results, which indicate a non-linear depth dependence with a gradient that tapers off with depth, i.e., slower pressure increase at larger depths. Hence, it appears that an extrapolation of the linear model of Hökmark et al. (2010) to larger depths, as indicated by the dotted line in Figure 3-16, would result in pressures that presumably could be regarded unrealistically high. Therefore, two linear models were applied here, which also yield considerable pressures at depth, but lower than those of the Hökmark et al. (2010) model (Figure 3-16). Note that the gradients of these models (3 MPa/km and 6 MPa/km) were arbitrarily chosen.

The effects of applying the forebulge excess pore pressure model are shown in Figure 3-17. The probability of *CFS*>0 on the steep zones increase, as expected. The increase is most significant below 0.5 km depth where the base case probability is low. At 5 km depth the highest probability increases from about 0.04 to 0.09. Above 0.5 km depth the increase is also visible. However, in this shallow depth range the probability is high irrespective of the pore pressure assumption made. Hence, the change is of minor practical importance in that shallow depth range. For ZFMENE0060A and ZFMENE0062A, the assumption of excess pore pressure appears to be without practical importance.

The effect of endglacial excess pore pressure on ZFMA2 is illustrated in Figure 3-18. The excess pressure has a significant effect on the *CFS* values. For the two assumptions of excess pore pressure, the probability of *CFS*>0 at 1.5 km depth increases from about 0.1 to 0.4 and 0.9, respectively.

It is judged that the assumptions of excess pore pressure made here can be regarded as low-probability bounding cases. For instance, the forebulge pressure is based on a pessimistic assumption that there is an unbroken and tight lid of continuous permafrost that locks in considerable pressures in the crust outside the margin of an approaching ice cap. The endglacial pore pressure models, in which the pressure is schematically modelled to increase with constant gradient to large depths may possibly also be regarded as pessimistic.

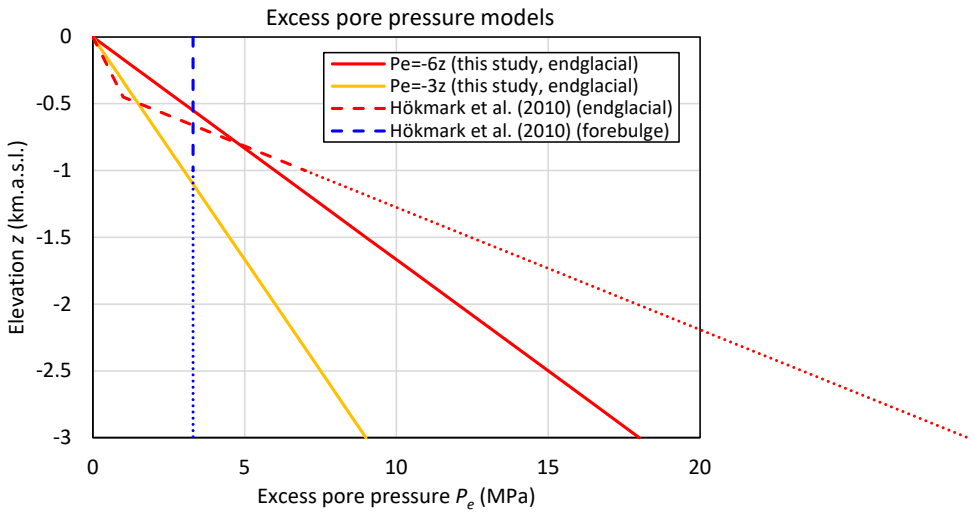

Figure 3-16. *Excess pore water pressure models. The dotted lines indicate extrapolations of the Hökmark et al. (2010) models.*

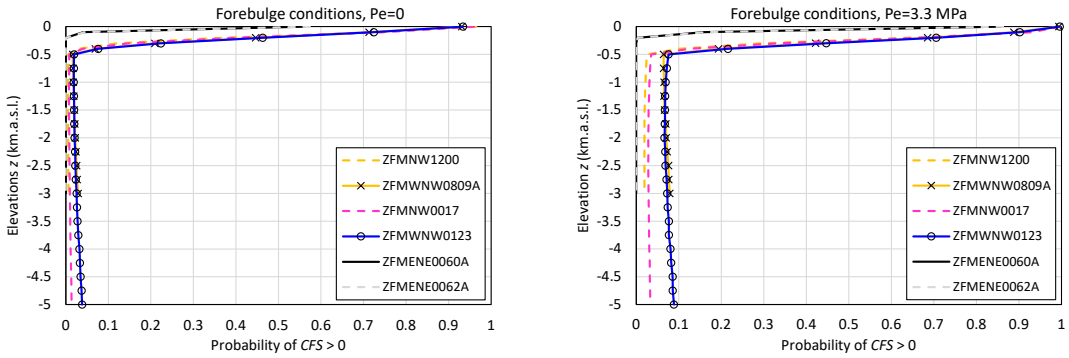

Figure 3-17. *Probability of CFS > 0 as function of depth for the six steep Forsmark deformation zones under forebulge load conditions. Left: Hydrostatic pore pressure (same results as in Figure 3-15). Right: P_e = 3.3 MPa at all depths.*

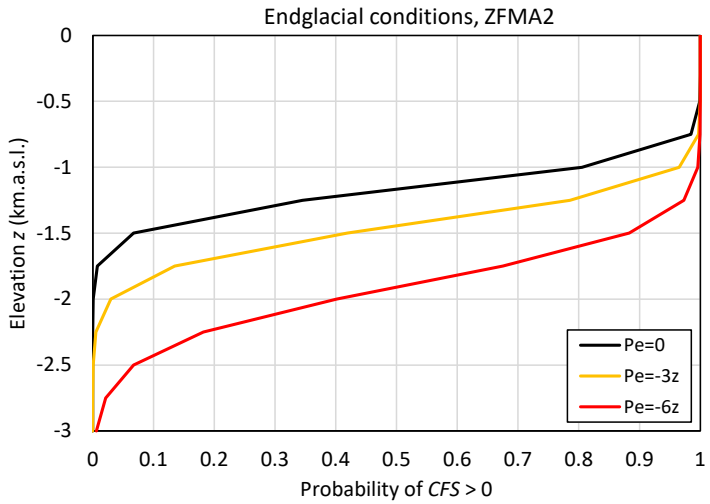

Figure 3-18. *Probability of CFS > 0 as function of depth for ZFMA2 under endglacial load conditions with the application of the excess pore pressure models.*

3.4.2 Impact of longer ice residence time

The effect of extending the ice residence at the time of ice maximum load contribution from 25,000 years to 50,000 years was examined. The extended residence time was tested for the UMISM, NH40 and RCP45e ice models in combination with three of the Earth models (cf. Table 2-3).

The effect on the glacial stresses of extending the ice residence time is demonstrated by the plots in Figure 3-19. The plots show results for the UMISM ice model and the cases without extension (+0k), with 25,000 years extension time (+25k) and with 50,000 years extension time (+50k). For this ice model, the glacial maximum occurs when the ice covers the site. Hence, the extension has potential implications only for the endglacial stresses. The same holds for the NH40 ice model. The diagrams show that assuming 25,000 years extension time leads to a significant increase of the horizontal stress components relative to the case without extension. For the ice/Earth model combinations shown in Figure 3-19, the maximum values of $\sigma_{H,g}$ and $\sigma_{h,g}$ become 5 %-30 % higher with 25,000 years extension time. Then, increasing the extension of the ice up to 50,000 years gives only marginal additions (2 %-4 %) to the stresses relative to the 25,000 years case.

The modest impact of extending the ice residence time from 25,000 years to 50,000 years is reflected by the results shown in Figure 3-20. The characteristics of the glacial stresses that give unstable conditions on ZFMA2 when assuming 50,000 years (lower panel) ice extension time are effectively the same as those of the base case models (upper panel), which include the cases with 25,000 years extension time.

In contrast to the UMISM and NH40 ice models, the RCP45e ice model, in which the ice margin barely reaches the site at its maximum extent (see section 2.3.2), generates typical forebulge stresses which tend to reduce stability on steep zones. For this ice model, the effects on the glacial stresses of and extended ice residence time is demonstrated in Figure 3-21. For the M14 Earth model, the extended ice residence time gives an increase of the stresses (i.e. less negative) and hence does not mean any potential reduction of zone stability. However, for the other two Earth models, the extension means significantly stronger forebulge effects. The minimum values of $\sigma_{H,g}$ and $\sigma_{h,g}$ become 20 %-90 % lower with the 25,000 years extension of the residence time. Then, increasing the residence time up to 50,000 years gives 5 %-9 % further reductions of the stresses relative to the 25,000 years case.

Comparing the results in Figure 3-21 with the results in Figure 3-9 to Figure 3-12, it can be noted that the minimum values of $\sigma_{H,g}$ and $\sigma_{h,g}$ obtained with both 25,000 years and 50,000 years extension times are on par with the lowest forebulge values generated with the NH40 ice model and which were included in the stability calculations presented in section 3.3.2.

The 25,000 years extension case, which is regarded to be pessimistic but within the frame of possible future developments, was included in the base case model catalogue applied in the calculations presented in section 3.3.2. The results presented here indicate that the 50,000 years extension case gives only modest additions to the glacial stresses relative to the 25,000 years case. Hence, it appears that the base case catalogue covers for longer glacial loading times up to 50,000 years. It can be concluded that the 50,000 years case does not add any information that needs to be included in any additional stability calculation.

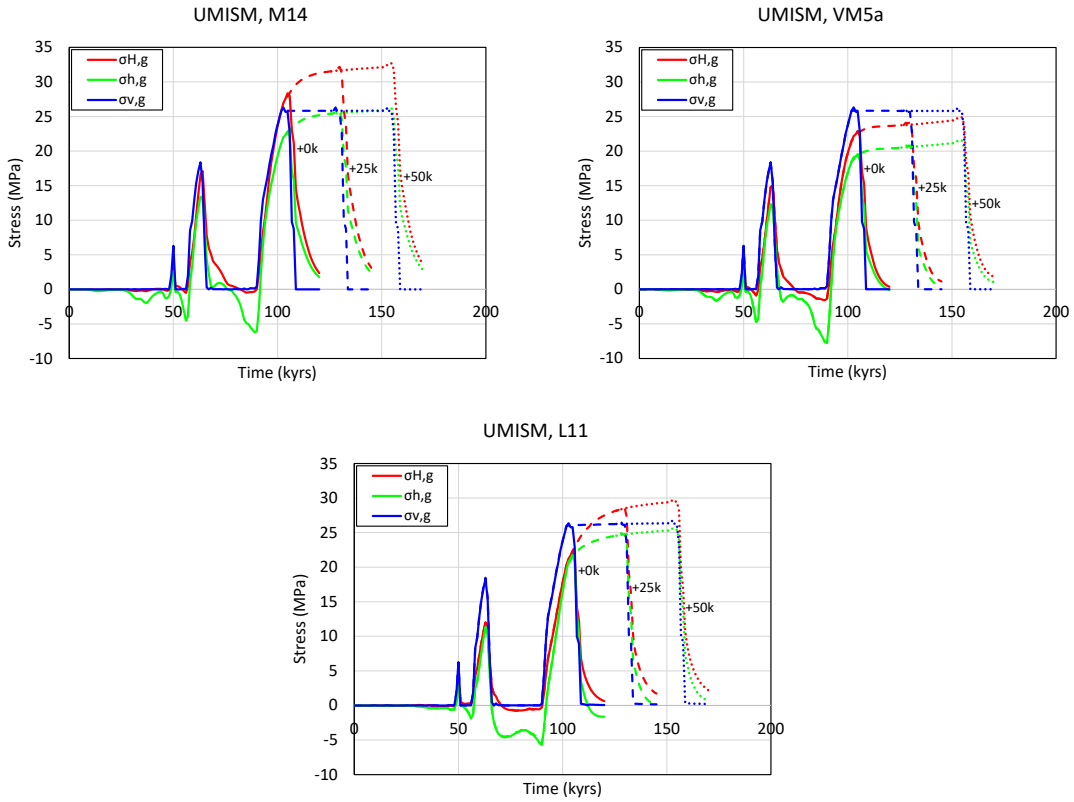

Figure 3-19. *Temporal evolution of principal stress components of the glacial stresses for the UMISM glacial scenario and three Earth models. The diagrams demonstrate the effects of 25,000 years extended ice residence time (+25k) (dashed lines) and 50,000 years extended ice residence time (+50k) (dotted lines).*

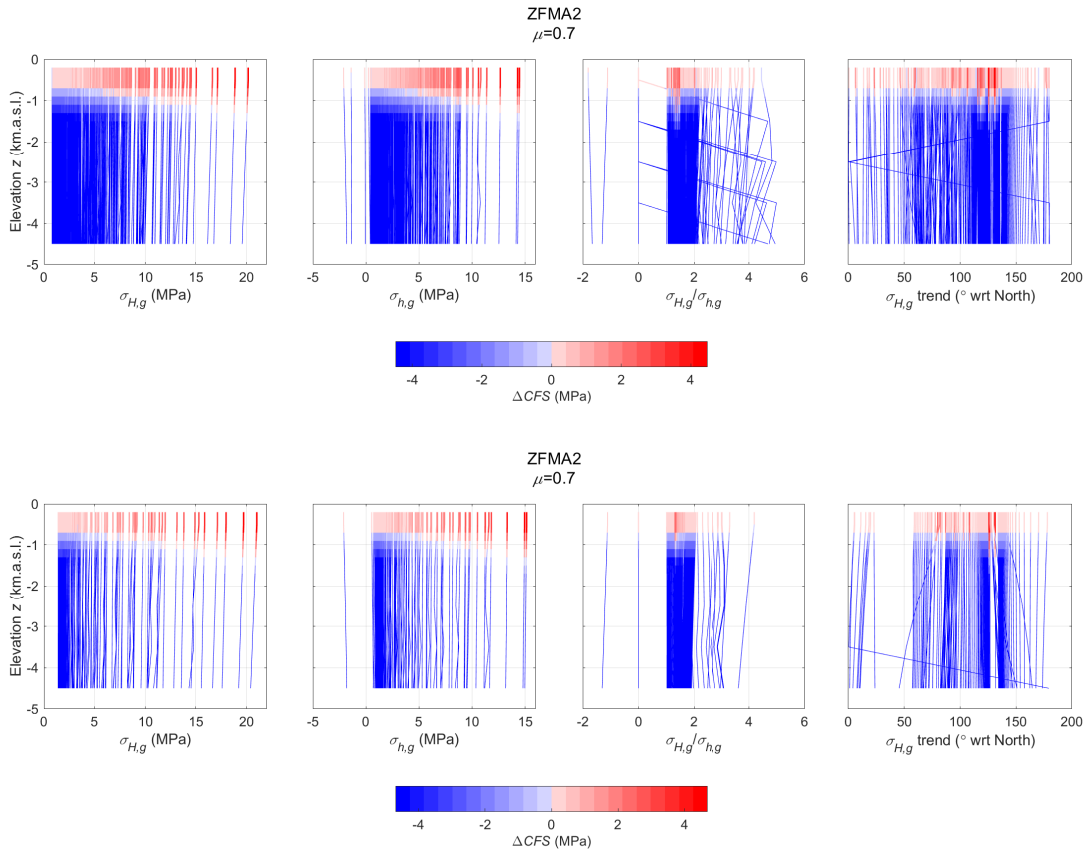

Figure 3-20. *Magnitudes, stress ratios and trends of the glacial stresses as function of depth for all time instances when ZFMA2 was marked as unstable. Upper: same plot as in Figure 3-8, i.e., all base case ice/Earth model combinations (including 25,000 years ice extension). Lower: ice/Earth model combinations with 50,000 years ice extension (Table 2-3). Values of $\sigma_{H,g}$ / $\sigma_{h,g}$ higher than 5 were set to zero in the plot. The line colour indicates ΔCFS. The lower limit of the colour scale is limited to make the plots clearer.*

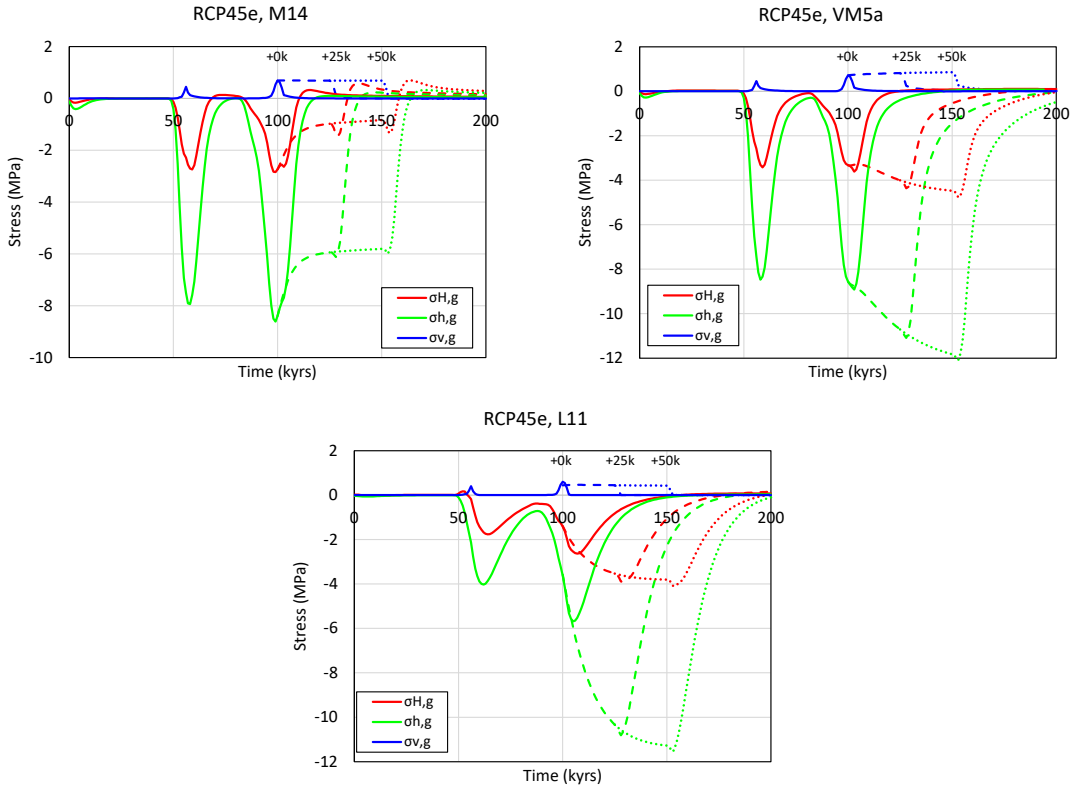

Figure 3-21. *Temporal evolution of principal stress components of the glacial stresses for the RCP45e glacial scenario and three Earth models. The diagrams demonstrate the effects of 25,000 years extended ice residence time (+25k) (dashed lines) and 50,000 years extended ice residence time (+50k) (dotted lines).*

3.4.3 Impact of the confidence level for the input parameters

All input parameters except for those related to the glacial stresses and the pore pressure were assumed to have normal probability distributions around their most likely values. For all parameters with normal distributions, it was basically assumed that the uncertainty limits given by site data correspond to a 95 % confidence interval. Here, it is examined how sensitive the end result is to changes to this assumption. A lower confidence level in the input implies that the uncertainty is larger. This is reflected as a larger spread in the output *CFS* values and a corresponding increase in the probability of *CFS*>0. This is demonstrated by the results in Figure 3-22, where results for ZFMNW0017 are shown. From the results it appears that the sensitivity to changes in the confidence level in the input parameters is modest. Reducing the input confidence level from χ = 95 % to χ = 80 % gives an increase in the *CFS*>0 probability of about 0.03 at 5 km depth. Reducing χ down to 70 % gives an increase in the *CFS*>0 probability of about 0.05.

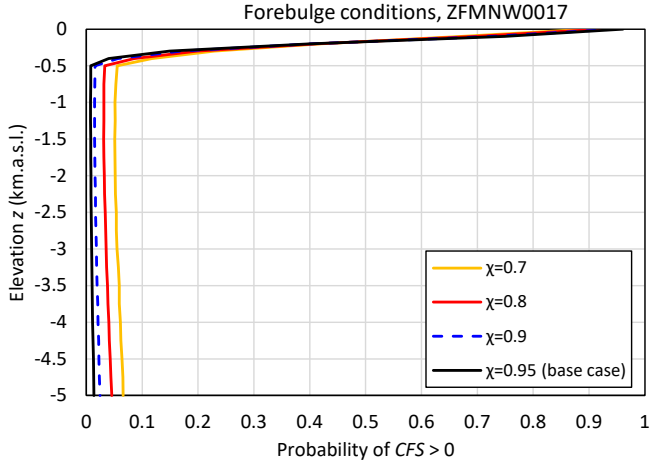

Figure 3-22. *Probability of CFS > 0 as function of depth for ZFMNW0017 under forebulge conditions. Different confidence levels in the input parameters are tested.*

4 Discussion

The stability calculations presented here means a significant development relative to previous stability evaluations carried out by e.g. Hökmark et al. (2019) and Fälth (2022). There are two main features of the present work that distinguishes it from the previous studies:

- In the previous studies, one set of GIA results based on the UMISM reconstruction of the Weichselian glaciation was considered. In the present work, this ice reconstruction was considered as well. However, four additional ice models were also included when the GIA results catalogue was developed. These five ice models were combined with five Earth models. For some ice/Earth model combinations, the effect of having an extended time of maximum glacial load was examined. This resulted in a base case GIA model catalogue that included a total of 34 cases. In addition, to get perspectives on the base case input, nine additional ice/Earth model combinations with an extra-long time of maximum glacial load were considered, resulting in a total of 43 studied cases.
- The uncertainties in the input were handled in a statistical manner by recognising that properties in nature typically do not take single values but rather tend to be distributed around some most likely or average value. Parameters based on site data were assumed to have normal probability distributions around most likely values while parameter values related to the glacial loading, due to the lack of observations, were given uniform likelihood. The stability calculations were carried out by means of Monte-Carlo simulations, which means that the likelihood of the results could be quantified.

The five glacial reconstructions used here cover a broad range of ice sheet possibilities of relevance for potential future glacial loads at Forsmark. These were combined with several models for the rheological structure of the lithosphere and the underlaying mantle. Hence, it could arguably be anticipated that the GIA results catalogue gives a representative state-of-the-art case coverage for the loading of the bedrock in Forsmark that potentially can be expected during future glaciations. In addition, including the cases with extended ice residence times at maximum ice load means that the range of glacially induced stress was expanded further.

It should be pointed out that the probability of $CFS > 0$ during forebulge and endglacial conditions, as calculated here, not is a probability in a general and strict sense that a zone becomes unstable during some given period of time. To make such an estimate one must have some notion about the probability that a glacial load reaches the Forsmark site and then include that in the calculation. The probability of glacial loads at Forsmark was not considered here. In the Monte-Carlo simulations it was implied that there actually is a period with glacial load at Forsmark.

Another aspect of the simulations is how the input was selected from the GIA model catalogue. The input was based on those GIA scenarios that appeared to have the potential to yield instability; the scenarios with minor impact were omitted. There are no notions about the likelihood of the different glacial scenarios in the GIA model catalogue. However, assuming that the likelihood is the same for all scenarios, the approach taken here, i.e., to systematically choosing scenarios with the strongest impact, suggests that the calculated probability of instability under forebulge and endglacial conditions is overestimated rather than underestimated.

Accounting for the uncertainty in the input parameters means that a considerable spread was obtained in the calculated *CFS* values. However, the fact that the effects of uncertainties in the input were considered in a systematic way should contribute to an increased confidence in the conclusions that are drawn based on the results.

The variation in *CFS* typically becomes larger at larger depths where higher stress levels and larger deviatoric stresses lead to higher sensitivity to variations in zone orientation, stress orientation and coefficient of friction. The spread tends to be larger for the steep zones, for which the results are particularly sensitive to the relative orientations of the background stresses and the glacial stresses (see discussion on this in Hökmark and Fälth (2014)). Here it is worth noting that the background stress anisotropy and stress level at the largest depth considered here (5 km) appear to be on par with observations made by Lund and Zoback (1999) (see section 2.3.1). It was further noted in section 2.3.1 that the uncertainty ranges applied for the horizontal background stresses imply an uncertainty in stress anisotropy that appears to be large rather than small when compared to the observations by Lund and Zoback (1999). However, it was also noted in section 2.3.1 that the uncertainty in the background stress orientation assumed here appears to be small (standard deviation 10°) when compared with the uncertainties (standard deviations 15° to 25°) associated with the data points for southern Sweden reported in the World Stress Map database (Heidbach et al. 2016).

Hence, when comparing with observations, it appears that some assumptions made here tend to give an overestimated variation in the *CFS* results while other assumptions tend to give an underestimated variation.

The potential effects of tectonic strain accumulation beneath a stabilizing ice cover were not considered here. This would have an impact primarily on the endglacial stresses and hence on the stability estimate for ZFMA2. The results indicate that ZFMA2 has low stability under present-day conditions and that it will be further destabilised during an endglacial stage. The probability that there will be unstable conditions is here estimated to be high over a large part of ZFMA2 during an endglacial stage. The possible impact of tectonic strain accumulation on the endglacial stress field can be estimated as follows. According to the Forsmark stress model, the major horizontal background stress at 0.5 km depth amounts to 56 MPa with the most likely trend assumed to be in accordance with the direction of the push from the Mid-Atlantic ridge (see section 2.3.1). The highest endglacial horizontal stress additions applied here are typically in the range 15 to 20 MPa. Assuming a relatively high tectonic strain rate of 10^{-9}/year (cf. section 2.3), a time period with ice cover of 50,000 years and that Young's modulus in the crust is 70 GPa yields 3.5 MPa of stress increase due to tectonic strain accumulation. This would correspond to about 5 % (3.5/(56+15)) increase of the endglacial horizontal stresses applied here. Thus, accounting for possible tectonic strain accumulation would have only a minor impact on the estimated ZFMA2 stability, and, given the low stability estimated for ZFMA2, it is judged that it wouldn't change the conclusions drawn here.

It is uncertain how possible tectonic strain accumulation would affect the stress conditions in the forebulge outside the ice sheet margin. However, since strain accumulation will work to increase horizontal stresses in the crust, there are good reasons to believe that it would promote stability on steep zones under these conditions. Hence, omitting potential strain accumulation effects when estimating forebulge stability on steep zones should be conservative.

The results presented here typically indicate that the stability of the Forsmark deformation zones located close to the repository will be lower at shallow depths, and that the probability of having unstable conditions may be considerable close to the ground surface. However, it should be pointed out that, even if instability is indicated by the calculations presented here, it does not necessarily mean that a dynamic earthquake rupture would be initiated. The results provide a quantitative estimate of the probability that a deformation zone becomes unstable. This is different from the probability of having an initiation of a dynamic rupture on that zone. The nucleation of an earthquake rupture is a complex process that is difficult to understand in detail. The process may also evolve differently in different cases.

A basic condition for the initiation of a dynamic rupture is that there is a certain amount of area on the zone or fault with low-enough stability. This is what can be estimated from the type of results presented here. It appears that this condition is not enough, though. From theoretical considerations, the smallest length L_c of a fracture for which the fracture growth will be unstable and accelerate can be estimated (Andrews 1976, Scholz 2002). This kind of estimate indicates that $L_c \sim 1/\sigma_n$, where σ_n is the normal stress on the fracture. This means that, for given fault properties and rock mass properties, rupture nucleation occurs easier at larger depths where stresses are higher. This finding is supported by observations of nucleation depths of crustal earthquakes (e.g. Figure 4-1 or data from SNSN 1904) and by dynamic simulations of shallow forebulge earthquake ruptures (Fälth 2022).

It appears that an initiation of a dynamic earthquake rupture above approximately 2 km depth would be a scenario with very low probability. Hence, there are good reasons to believe that *CFS* values at depths above 0.5 km will be of little importance when assessing the risk of earthquake ruptures.

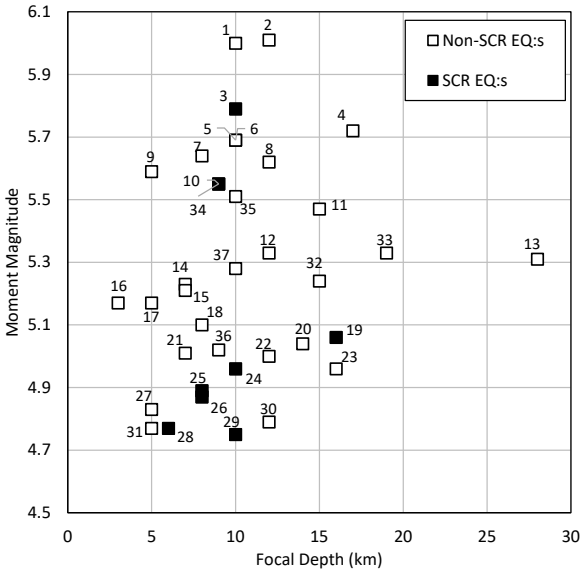

Figure 4-1. *Moment magnitude versus focal depth for crustal earthquakes from the Wells and Coppersmith (1994) catalogue. The catalogue events are limited to a maximum rupture area of 40 km^2. "SCR" means "Stable Continental Region". The data labels refer to the references in Table 4-1 supporting the given focal depths.*

Table 4-1. Focal depth references in Figure 4-1.

Ref no.	EQ no. in W&C 1994*	Reference	Ref no.	EQ no. in W&C 1994*	Reference
1	180	(Westaway et al. 1989)	20	149	(Frankel 1984)
2	214	(Hauksson et al. 1988)	21	212	(Wei and Chung 1993)
3	197	(USGS 2020)	22	110	(Hartzell and Brune 1979)
4	97	(Ellsworth et al. 1973)	23	224	(Ma and Kanamori 1991)
5	77	(Thatcher and Hamilton 1973)	24	211	(Langer and Bollinger 1991)
6	242	(Walter 1993)	25	173	(Nabelek and Suarez 1989)
7	198	(Zhou et al. 1993)	26	195	(Ohio Geological Survey 1986)
8	236	(Dreger and Helmberger 1991)	27	93	(Johnson and McEvilly 1974)
9	231	(Hauksson and Jones 1991)	28	176	(Moreno and Camelbeeck 2013)
10	165	(Choy et al. 1983)	29	142	(Hasegawa and Wetmiller 1980)
11	136	(Peppin et al. 1989)	30	166	(Frankel 1984)
12	234	(Horton et al. 1997)	31	94	(Johnson and McEvilly 1974)
13	184	(Spence et al. 1996)	32	126	(USGS 2020)
14	88	(Ellsworth 1975)	33	226	(USGS 2020)
15	133	(Haessler et al. 1980)	34	138	(USGS 2020)
16	59	(Evans and McEvilly 1982)	35	207	(USGS 2020)
17	150	(Courjault-Radé et al. 2009)	36	213	(USGS 2020)
18	237	(Hardebeck 2010)	37	235	(USGS 2020)
19	155	(Mauk et al. 1982)			

* Earthquake number in the earthquake catalogue of Wells and Coppersmith (1994).

Except for the depth at which unstable conditions may develop, there are also other factors of importance for the possibility that an earthquake rupture is initiated. Consider the temporal evolutions of *CFS* for the UMISM, NH40 and RCP45 ice reconstructions depicted in Figure 4-2. The dotted lines indicate the approximate rates at which *CFS* is increased on the gently ZFMA2 during the endglacial stage and on the steep ZFMNW0017 under forebulge conditions. It appears that the englacial *CFS* rate would be several times higher than the forebulge rate. The instability increase leading up to maximum forebulge instability is caused by slow crustal flexure, which is, in turn, directly controlled by the properties of the viscous mantle, whereas the endglacial instability increases fast due to the direct elastic response of the crust to the loss of vertical load. The rate at which the ice load increases/decreases also has some influence on the *CFS* change rate. However, as can be noted when comparing the ice load curves and the corresponding *CFS* curves in Figure 4-2, the time scale of the glacial loading/unloading is significantly shorter than the time scale of mantle deformation. Hence, the slow response of the mantle is the main reason for the difference between the forebulge *CFS* change rate and the *CFS* change rate during the endglacial stage. Similar observations were made by Hökmark and Fälth (2014) for the stability evolutions on Olkiluoto deformation zones. The slower loss of stability during the forebulge stage should promote slow aseismic strain energy release and lead to a lower probability of dynamic earthquake ruptures than during the endglacial stage.

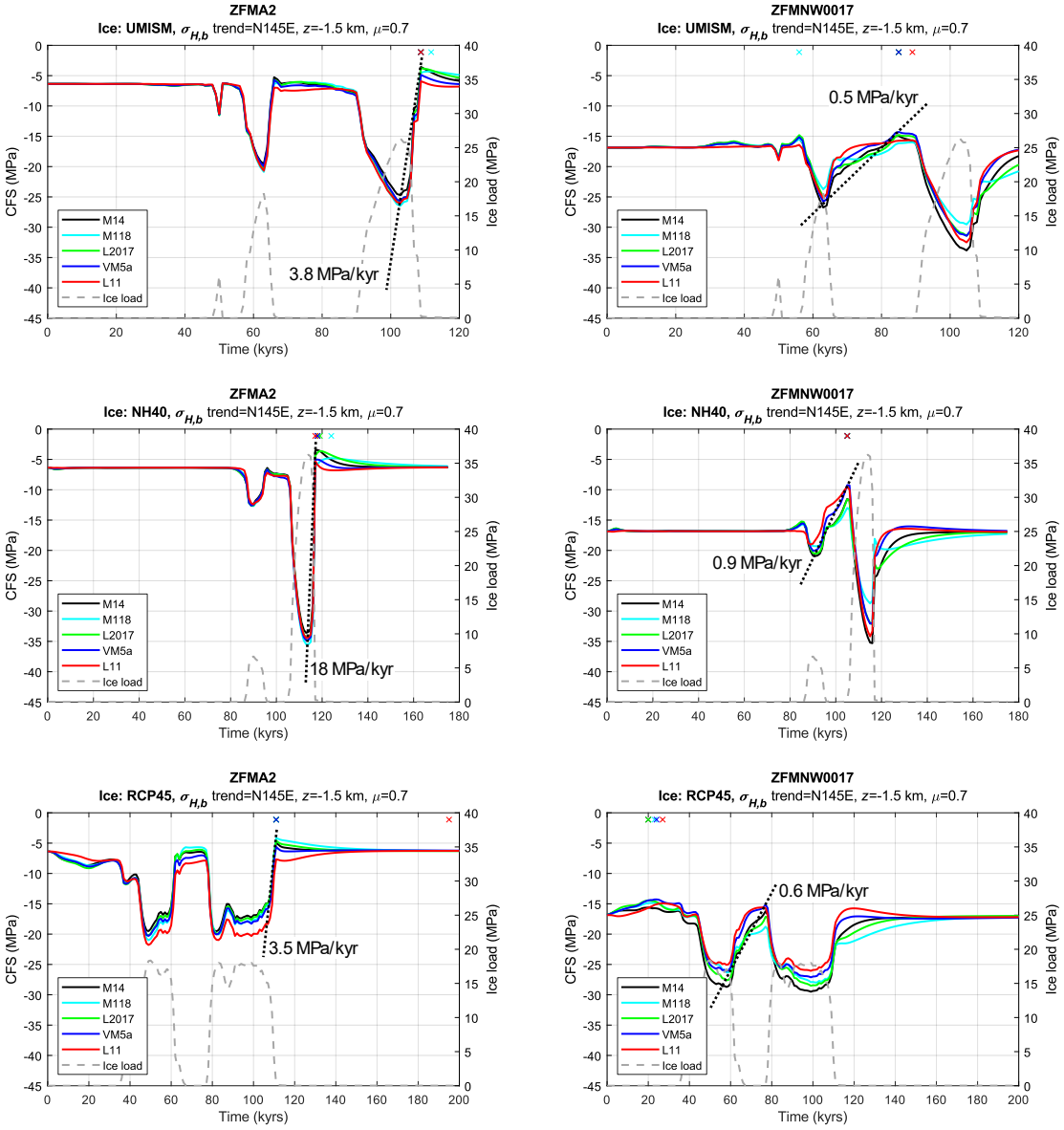

Figure 4-2. *CFS evolutions at 1.5 km depth on the gently dipping ZFMA2 (left) and on the steeply dipping ZFMNW0017 (right) for the UMISM, NH40 and RCP45 ice reconstructions. The dotted lines and the corresponding numbers indicate the approximate CFS loss rates during the endglacial (ZFMA2) and forebulge (ZFMNW0017) stages.*

5 Conclusions

The objective of the work presented in this report was to evaluate the stability of the seven local Forsmark deformation zones ZFMA2, ZFMNW0017, ZFMNW1200, ZFMWNW0123, ZFMWNW0809A, ZFMENE0060A and ZFMENE0062A, located close to or within the repository layout. The stability of these particular zones was considered since the reactivation of one of these zones may potentially have implications for the repository safety (SKB 2022). The stability was evaluated for present-day conditions as well as for conditions that may arise at the beginning or at the end of a glacial period.

The background stress model for Forsmark applied in the present study is a newly developed model (Hakami et al. 2025), which is mainly based on the recent ranking results of the reliability assessment of overcoring stress measurements at Forsmark (Sjöberg et al. 2025). According to this model, the horizontal stresses at repository depth are more than 30 % higher than those given by the previous model (Martin 2007). The glacially induced stresses were based on results from a new catalogue of GIA models of which 34 ice/Earth model combinations were included in the base case set.

The zone stability was evaluated in terms of the Coulomb Failure Stress (*CFS*) measure, which is defined as the difference between the shear load and the shear resistance on a fault/fracture-plane. A positive value of *CFS* means instability.

The *CFS* measure indicates if unstable conditions exist and also quantifies the "severity" of the instability. However, it does not provide any information about the character of a potential reactivation event, i.e., if it will take place as a seismic event or as a slow, aseismic movement. It is stated in this report, though, based on theory and data, that, particularly at shallow depths above some 2 km, the initiation of a seismic event would be a scenario with low probability even if *CFS* is estimated to be positive in this depth range.

The uncertainty in the input was considered by assuming that the input parameters are random variables. Parameters based on site investigation data were assumed to have normal probability distributions while glacial stress parameters were given uniform distributions. The *CFS* calculations were performed by means of Monte-Carlo simulations and thereby the uncertainty in the input was reflected in the output results.

Based on the results from the calculations made for present-day conditions, the following can be concluded:

- The shallow and gently dipping ZFMA2 has low stability over a significant part of its depth extent. The results indicate that the probability of $CFS>0$ is higher than 0.2 down to about 1 km depth. Below 1.5 km depth, there is zero probability of $CFS>0$.
- Due to the high horizontal background stresses at Forsmark, the steep zones ZFMNW0017, ZFMNW1200, ZFMWNW0123, ZFMWNW0809A, ZFMENE0060A and ZFMENE0062A are clamped by high normal stresses. Hence, in general these zones have high stability under present-day conditions. The probability that these zones would be unstable below 0.5 km depth, under these conditions, is practically zero.
- The parameter variation yields a considerable variation in *CFS* values at most depths, particularly for the steep zones. For these zones, the *CFS* variation may be ±50 % or more below 0.5 km depth. The uncertainty increases with depth. This is attributed to the increase in both stress level and deviatoric stress with depth.
- In general, there is a fairly reasonable agreement between the most likely *CFS* values and the values obtained with the background stress model adopted by Fälth (2022).

When the probability of CFS>0 was estimated for conditions that may arise at the beginning or at the end of a glacial period, it was implied that there actually is a glacial load that influences the stress conditions in Forsmark; the probability of having such load conditions was not considered. The following conclusions can be made:

- In the forebulge, at the beginning of a glacial period, the stability tends to be reduced on the steep zones ZFMNW0017, ZFMNW1200, ZFMWNW0123, ZFMWNW0809A, ZFMENE0060A and ZFMENE0062A relative to what is found for present-day conditions. There is a non-zero probability of *CFS*>0 at all depths on the northwest striking zones ZFMNW0017, ZFMNW1200, ZFMWNW0123 and ZFMWNW0809A. However, the probability at depths below 0.5 km is modest and is in the range 0.01 to 0.04. On the northeast striking zones ZFMENE0060A and ZFMENE0062A, the stability margins are high. At depths below 0.3 km, the probability of *CFS*>0 is practically zero on these two zones. The most likely *CFS* values on the steep zones are on par or lower than the values obtained by Fälth (2022).
- Under endglacial conditions, at the end of a glacial period, the stability tends to be reduced on the gently dipping zone ZFMA2 relative to what is found for present-day conditions. The probability of *CFS*>0 exceeds 0.2 down to about 1.4 km depth. The stability estimated here for this zone is in general lower than the stability estimated when applying the stress conditions considered by Fälth (2022). This is attributed to the higher horizontal stresses in the new background stress model.
- As for the case with present-day conditions, there is a considerable spread in the *CFS* values, particularly for the steep zones, which are highly sensitive to variations in deformation zone strike and stress orientation.
- Applying excess pore pressure assumptions that are judged to be low-probability bounding cases has a clear impact on the calculated zone stability. For ZFMA2, the two assumptions of endglacial excess pore pressure considered here, the probability of *CFS*>0 at 1.5 km depth increases from 0.1 to 0.4 and 0.9, respectively. When applying the forebulge pore pressure assumption to the steep zones the probability of *CFS*>0 increases from low levels and stays in the range 0.02 to 0.09 at depths below 0.5 km (except for the northeast striking ZFMENE0060A and ZFMENE0062A). Due to the high stability margins on ZFMENE0060A and ZFMENE0062A the excess pore pressure is without practical importance for these zones.
- Extending the ice residence time at maximum ice load from 25,000 years to 50,000 years gives only minor additions to the glacial stresses. This indicates that the base case GIA model catalogue, which includes the case of extending the ice residence time by 25,000 years, covers for situations where a large ice sheet remains stationary for times up to at least 50,000 years.
- The sensitivity to the assumed confidence level of the normally distributed input parameters appears to be modest. Reducing the input confidence level from 95 % to 80 % gives an increase in the *CFS*>0 probability of about 0.03 at 5 km depth on ZFMNW0017 under forebulge conditions.

To summarise, the gently dipping ZFMA2 has low stability under present-day conditions and will be further destabilised under endglacial conditions. All steep zones are stable under present-day conditions. Under forebulge conditions, it cannot be excluded that the northwest striking steep zones ZFMNW0017, ZFMNW1200, ZFMWNW0123 and ZFMWNW0809A may become unstable. Regardless of the load conditions, the probability of instability on the northeast striking steep zones ZFMENE0060A and ZFMENE0062A appears to be very low.

6 References

SKB's (Svensk Kärnbränslehantering AB) publications can be found at www.skb.com/publications.

Andrews D J, 1976. Rupture propagation with finite stress in antiplane strain. Journal of Geophysical Research (1896-1977) 81 (20), 3575–3582, doi:10.1029/JB081i020p03575.

Benn D, Evans D J A, 2010. Glaciers and Glaciation, 2nd edition. London: Routledge. https://doi.org/10.4324/9780203785010

Byerlee J, 1978. Friction of rocks. Pure Appl. Geophys. 116 (4–5), 615–626, doi:10.1007/bf00876528

Castro-Vera L, Gaus G, Colling Cassel M, Amberg S, Littke R, 2025. 3D basin modeling of the Lower Saxony Basin, Germany: the role of overpressure in Mesozoic claystones with implications for nuclear waste storage. International Journal of Earth Sciences 114 (2), 221–247, doi:10.1007/s00531-024-02484-w

Choy G L, Boatwright J, Dewey J W, Sipkin S A, 1983. A teleseismic analysis of the New Brunswick Earthquake of January 9, 1982. Journal of Geophysical Research: Solid Earth 88 (B3), 2199–2212, doi:10.1029/JB088iB03p02199

Colleoni F, Liakka J, 2020. Transient simulations of the Eurasian ice sheet during the Saalian glacial cycle. SKB TR-19-17, Svensk Kärnbränslehantering AB.

Courjault-Radé P, Darrozes J, Gaillot P, 2009. The M = 5.1 1980 Arudy earthquake sequence (western Pyrenees, France): a revisited multi-scale integrated seismologic, geomorphologic and tectonic investigation. International Journal of Earth Sciences 98 (7), 1705–1719, doi:10.1007/s00531-008-0320-5

Dreger D, Helmberger D, 1991. Source parameters of the Sierra Madre Earthquake from regional and local body waves. Geophysical Research Letters 18 (11), 2015–2018, doi:10.1029/91GL02366

Ellsworth W L, 1975. Bear Valley, California, earthquake sequence of February-March 1972. Bulletin of the Seismological Society of America 65 (2), 483–506, doi:10.1785/BSSA0650020483

Ellsworth W L, Campbell R H, Hill D P, Page R A, Alewine R W, Hanks T C, Heaton T H, Hileman J A, Kanamori H, Minster B, Whitcomb J H, 1973. Point Mugu, California, Earthquake of 21 February 1973 and Its Aftershocks. Science 182 (4117), 1127–1129, doi:10.1126/science.182.4117.1127

Evans D G, McEvilly T V, 1982. A note on relocating the 1963 Watsonville earthquakes. Bulletin of the Seismological Society of America 72 (4), 1309–1316, doi:10.1785/BSSA0720041309

Frankel A, 1984. Source parameters of two ML ~ 5 earthquakes near Anza, California, and a comparison with an Imperial Valley aftershock. Bulletin of the Seismological Society of America 74 (5), 1509–1527, doi:10.1785/BSSA0740051509

Fälth B, 2018. Simulating earthquake rupture and near-fault fracture response. Doctoral Thesis. Uppsala University, Uppsala.

Fälth B, 2022. Deformation zone stability and co-seismic secondary fracture displacements at Forsmark. SKB TR-22-13, Svensk Kärnbränslehantering AB.

Fälth B, Hökmark H, Munier R, 2010. Effects of large earthquakes on a KBS-3 repository. Evaluation of modelling results and their implications for layout and design. SKB TR-08-11. Svensk Kärnbränslehantering AB.

Fälth B, Hökmark H, Lund B; 2016. Simulation of co-seismic secondary fracture displacements for different earthquake rupture scenarios at the proposed nuclear waste repository site in Forsmark. International Journal of Rock Mechanics and Mining Sciences 84, 142–158, doi:10.1016/j.ijrmms.2016.02.009

Glamheden R, Fredriksson A, Röshoff K, Karlsson J, Hakami H, Christiansson R; 2007. Rock Mechanics Forsmark. Site descriptive modelling Forsmark stage 2.2. SKB R 07-31. Svensk Kärnbränslehantering AB.

Gregersen S, Lindholm C, Korja A, Lund B, Uski M, Oinonen K, Voss P H, Keiding M, 2021. Seismicity and Sources of Stress in Fennoscandia. Glacially-Triggered Faulting. Cambridge University Press. https://doi.org/10.1017/9781108779906.014

Haessler H, Hoang-Trong P, Schick R, Schneider G, Strobach K, 1980. The September 3, 1978, Swabian Jura earthquake. Tectonophysics 68 (1), 1–14, doi:10.1016/0040-1951(80)90005-0

Hakami E, Sánchez Juncal A, Mas Ivars D, 2025. Baseline Forsmark – Rock Mechanics. SKB R-23-05, Svensk Kärnbränslehantering AB.

Hardebeck J L, 2010. Seismotectonics and Fault Structure of the California Central Coast. Bulletin of the Seismological Society of America 100 (3), 1031–1050, doi:10.1785/0120090307

Harris R A, 1998. Introduction to special section: Stress triggers, stress shadows, and implications for seismic hazard. J. Geophys. Res. 103 (B10), 24,347-24,358, doi:10.1029/98jb01576

Hartzell S, Brune J N, 1979. The horse canyon earthquake of August 2, 1975—Two-stage stress-release process in a strike-slip earthquake. Bulletin of the Seismological Society of America 69 (4), 1161–1173, doi:10.1785/BSSA0690041161

Hasegawa H S, Wetmiller R J, 1980. The Charlevoix Earthquake of 19 August 1979 and its Seismo-Tectonic Environment*. Seismological Research Letters 51 (4), 23–38, doi:10.1785/gssrl.51.4.21

Hauksson E, Jones L M, 1991. The 1988 and 1990 upland earthquakes: Left-lateral faulting adjacent to the central transverse ranges. Journal of Geophysical Research: Solid Earth 96 (B5), 8143–8165, doi:10.1029/91JB0048

Hauksson E, Jones L M, Davis T L, Hutton L K, Williams P, Bent A L, Brady A G, Reasenberg P A, Michael A J, Yerkes R F, Etheredge E, Porcella R L, Johnston M J S, Reagor G, Stover C W, Bufe C G, Cranswick E, Shakal A K, 1988. The 1987 Whittier Narrows Earthquake in the Los Angeles Metropolitan Area, California. Science 239 (4846), 1409–1412, doi:10.1126/science.239.4846.1409

Heidbach O, Rajabi M, Reiter K, Ziegler M, 2016. World Stress Map 2016. GFZ Data Services. https://doi.org/10.5880/WSM.2016.002

Hermanson J, Petersson J, 2022. Methodology for deterministic geological modelling of the Forsmark site. Application to the development of the final repository for spent nuclear fuel. SKB R-20-10, Svensk Kärnbränslehantering AB.

Horton S P, dePolo D M, Walter W R, 1997. Source parameters and tectonic setting of the 1990 Lee Vining, California, earthquake sequence. Bulletin of the Seismological Society of America 87 (4), 1035–1045, doi:10.1785/BSSA0870041035

Hökmark H, Fälth B, 2014. Approach to Assessing the Stability of Olkiluoto Deformation Zones During a Glacial Cycle. Posiva Working Report 2013-37. Posiva Oy, Eurajoki, Finland.

Hökmark H, Lönnqvist M, Fälth B, **2010**. THM-issues in repository rock. Thermal, mechanical, thermo-mechanical and hydro-mechanical evolution of the rock at the Forsmark and Laxemar sites. SKB TR-10-23. Svensk Kärnbränslehantering AB.

Hökmark H, Fälth B, Lönnqvist M, Munier R, 2019. Earthquake simulations performed to assess the long-term safety of a KBS-3 repository. Overview and evaluation of results produced after SR-Site. SKB TR-19-19, Svensk Kärnbränslehantering AB.

Jaeger J C, Cook N G W, 1979. Fundamentals of rock mechanics. Third ed. Science Paperbacks/Chapman and Hall, London, UK, ISBN: 978-0-412-22010-4

Johnson L R, McEvilly T V, 1974. Near-field observations and source parameters of central California earthquakes. Bulletin of the Seismological Society of America 64 (6), 1855–1886, doi:10.1785/BSSA0640061855

Lagerbäck R, Sundh M, 2008. Early Holocene faulting and paleoseismicity in northern Sweden. Research Paper C 836. Sveriges geologiska undersökning.

Langer C J, Bollinger G A, 1991. The southeastern Illinois earthquake of 10 June 1987: The later aftershocks. Bulletin of the Seismological Society of America 81 (2), 423–445, doi:10.1785/BSSA0810020423

Lund B, Zoback M D, 1999. Orientation and magnitude of in situ stress to 6.5 km depth in the Baltic Shield. International Journal of Rock Mechanics and Mining Sciences 36 (2), 169–190, doi:10.1016/S0148-9062(98)00183-1

Lund B, Schmidt P, Hieronymus C, 2009. Stress evolution and fault stability during the Weichselian glacial cycle. SKB TR-09-15. Svensk Kärnbränslehantering AB (SKB), Stockholm, Sweden.

Lönnqvist M, Hökmark H, 2013. Approach to estimating the maximum depth for glacially induced hydraulic jacking in fractured crystalline rock at Forsmark, Sweden. J. Geophys. Res. 118 (3), 1777–1791, doi:10.1002/jgrf.20106

Ma K-F, Kanamori H, 1991. Aftershock sequence of the 3 December 1988 Pasadena earthquake. Bulletin of the Seismological Society of America 81 (6), 2310–2319, doi:10.1785/BSSA0810062310

Martin C D, 2007. Quantifying in situ stress magnitudes and orientations for Forsmark. Forsmark stage 2.2. SKB R-07-26, Svensk Kärnbränslehantering AB.

MathWorks, 2020. MATLAB R2019a, Update 9.

Mauk F J, Christensen D, Henry S, 1982. The Sharpsburg, Kentucky, earthquake 27 July 1980: Main shock parameters and isoseismal maps. Bulletin of the Seismological Society of America 72 (1), 221–236, doi:10.1785/BSSA0720010221

Moreno D G, Camelbeeck T, 2013. Comparison of ground motions estimated from prediction equations and from observed damage during the M = 4.6 1983 Liège earthquake (Belgium). Natural Hazards and Earth System Sciences 13 (8), 1983–1997, doi:10.5194/nhess-13-1983-2013

Muir Wood R, 1995. Reconstructing the tectonic history of Fennoscandia from its margins: The past 100 million years. SKB TR-95-36, Svensk Kärnbränslehantering AB.

Munier R, Adams J, Brandes C, Brooks G, Dehls J, Einarsson P, Gibbons S J, Hjartardóttir Á R, Hogaas F, Johansen T A, Kvaerna T, Mattila J, Mikko H, Müller K, Nikolaeva S B, Ojala A E K, Olesen O, Olsen L, Palmu J-P, Ruskeeniemi T, Ruud B O, Sandersen P B E, Shvarev S V, Smith C A, Steffen H, Steffen R, Sutinen R, Tassis G, 2020. International database of Glacially Induced Faults, doi:10.1594/PANGAEA.922705

Nabelek J, Suarez G, 1989. The 1983 Goodnow earthquake in the central Adirondacks, New York: Rupture of a simple, circular crack. Bulletin of the Seismological Society of America 79 (6), 1762–1777, doi:10.1785/BSSA0790061762

Ohio Geological Survey, 1986. Northeastern Ohio Quake, January 1986. Available at http://geosurvey.ohiodnr.gov/quakes-1950-to-1999-pgs/northeastern-ohio-january-1986.

Peppin W A, Honjas W, Somerville M R, Vetter U R, 1989. Precise master-event locations of aftershocks of the 4 October 1978 Wheeler Crest earthquake sequence near Long Valley, California. Bulletin of the Seismological Society of America 79 (1), 67–76, doi:10.1785/BSSA0790010067

Petersson J, Hultgren P, Hermanson J, Isaksson H, Sarlus Z, Stigsson M, Markström I, 2024. Baseline Forsmark - Geology. Updating of existing site descriptive models. SKB R-24-07. Svensk Kärnbränslehantering AB.

Scherneck H-G, Lidberg M, Haas R, Johansson J M, Milne G A, 2010. Fennoscandian strain rates from BIFROST GPS: A gravitating, thick-plate approach. Journal of Geodynamics 50 (1), 19–26, doi:10.1016/j.jog.2009.11.005

Schmidt P, Lund B, 2025. The glacially induced stress field in Forsmark. Simulations with past and future ice sheet models and various earth models. SKB TR-25-03. Svensk Kärnbränslehantering AB.

Scholz C H, 2002. The Mechanics of Earthquakes and Faulting. Cambridge University Press, ISBN: 0 521 655540 4

Sjöberg J, Figueiredo B, Hakala M, 2025. Reliability ranking of overcoring stress measurements at Forsmark. SKB R-21-08. Svensk Kärnbränslehantering AB.

SKB, 2010a. Buffer, backfill and closure process report for the safety assessment SR-Site. SKB TR-10-47. Svensk Kärnbränslehantering AB.

SKB, 2010b. Climate and climate-related issues for the safety assessment SR-Site. SKB TR-10-49. Svensk Kärnbränslehantering AB.

SKB, 2011. Long-term safety for the final repository for spent nuclear fuel at Forsmark. Main report of the SR-Site project. SKB TR-11-01. Svensk Kärnbränslehantering AB.

SKB, 2022. Post-closure safety for the final repository for spent nuclear fuel at Forsmark. Main report, PSAR version. SKB TR-21-01. Svensk Kärnbränslehantering AB.

Slunga R S, 1991. The Baltic Shield earthquakes. Tectonophysics 189 (1), 323–331, doi:10.1016/0040-1951(91)90505-M

SNSN, 1904. Swedish National Seismic Network. Dataset/Seismic network. Uppsala University, Uppsala, Sweden. (www.snsn.se). https://doi.org/10.18159/SNSN

Spence W, Langer C J, Choy G L, 1996. Rare, large earthquakes at the Laramide deformation front—Colorado (1882) and Wyoming (1984). Bulletin of the Seismological Society of America 86 (6), 1804–1819, doi:10.1785/BSSA0860061804

Steffen R, Steffen H, 2021. Reactivation of Non-Optimally Orientated Faults Due to Glacially Induced Stresses. Tectonics 40 (11), e2021TC006853, doi:https://doi.org/10.1029/2021TC006853

Stephansson O, Ljunggren C, Jing L, 1991. Stress measurements and tectonic implications for Fennoscandia. Tectonophysics 189 (1), 317–322, doi:10.1016/0040-1951(91)90504-L

Stephens M B, Simeonov A, 2015. Description of deformation zone model version 2.3, Forsmark. SKB R-14-28. Svensk Kärnbränslehantering AB.

Thatcher W, Hamilton R M, 1973. Aftershocks and source characteristics of the 1969 Coyote Mountain earthquake, San Jacinto Fault zone, California*. Bulletin of the Seismological Society of America 63 (2), 647–661, doi:10.1785/BSSA0630020647

Thölix L, Korhonen H, Ruosteenoja K, 2019. Climate Projections for Olkiluoto. Posiva Working Report 2018-09. Posiva Oy, Eurajoki, Finland.

USGS, 2020. U.S Geological Survey WebSite: https://earthquake.usgs.gov/earthquakes/search/

Walter W R, 1993. Source parameters of the June 29, 1992 Little Skull Mountain Earthquake from complete regional waveforms at a single station. Geophysical Research Letters 20 (5), 403–406, doi:10.1029/92GL03031

Wei B-Z, Chung W-Y, 1993. Regional waveform constraints on the source parameters of the Xunwu, China, earthquake of 2 August 1987, with implications for mid-plate seismotectonics. Physics of the Earth and Planetary Interiors 78 (1), 57–68, doi:10.1016/0031-9201(93)90084-M

Wells D L, Coppersmith K J, 1994. New empirical relationships among magnitude, rupture length, rupture width, rupture area and surface displacement. Bull. Seism. Soc. Am. 84 (4), 974–1002.

Westaway R, Gawthorpe R, Tozzi M, 1989. Seismological and field observations of the 1984 Lazio-Abruzzo earthquakes: implications for the active tectonics of Italy. Geophysical Journal International 98 (3), 489–514, doi:10.1111/j.1365-246X.1989.tb02285.x

Zhou Y, McNally K C, Lay T, 1993. Analysis of the 1986 Mt. Lewis, California, earthquake: preshock sequence-mainshock-aftershock sequence. Physics of the Earth and Planetary Interiors 75 (4), 267–288, doi:10.1016/0031-9201(93)90005-T

Zoback M D, Townend J, 2001. Implications of hydrostatic pore pressures and high crustal strength for the deformation of intraplate lithosphere. Tectonophysics 336 (1–4), 19–30, doi:10.1016/S0040-1951(01)00091-9

7 Appendix 1

Probability distributions of input parameters

Here, examples of probability distributions of input parameters are presented.

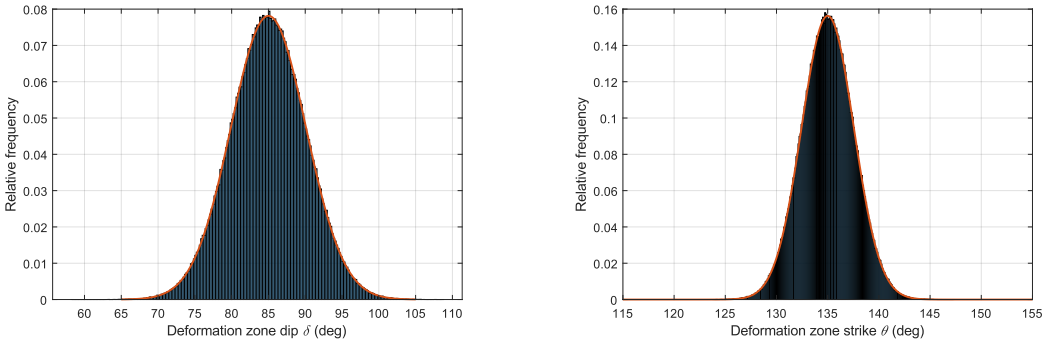

Figure 7-1. *Histograms showing applied normal distributions of ZFMNW0017 dip and strike plotted along with corresponding theoretical probability density functions.*

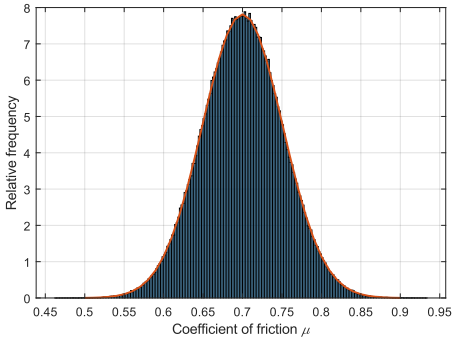

Figure 7-2. *Histogram showing the normal distributions of the coefficient of friction plotted along with the corresponding theoretical probability density function.*

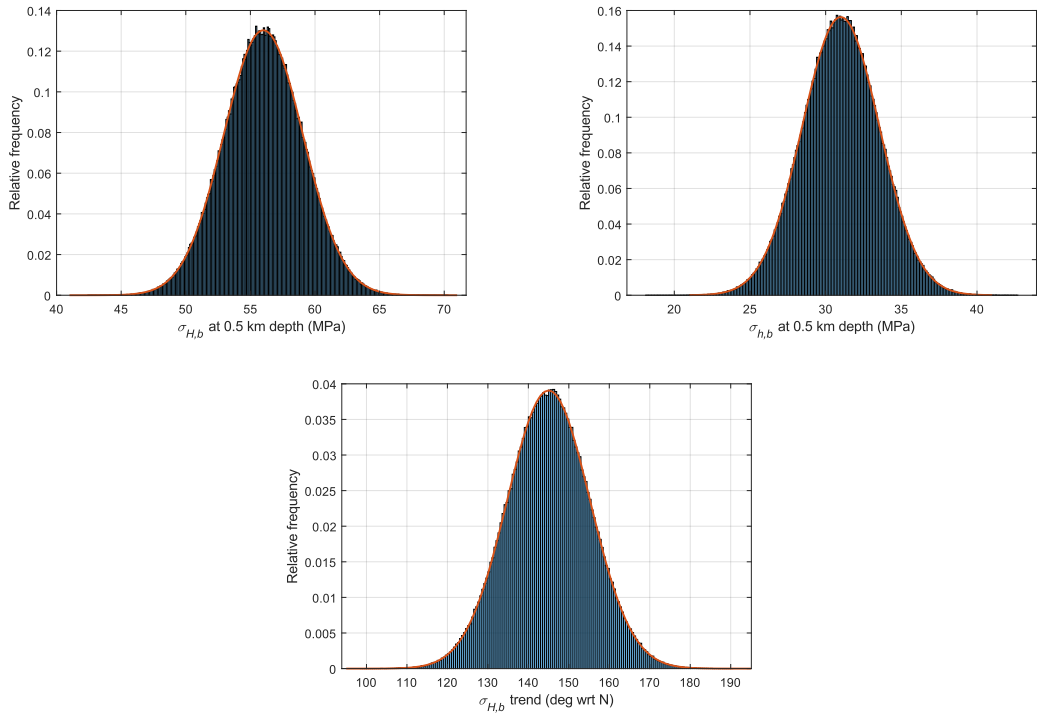

Figure 7-3. *Histograms showing applied normal distributions of $\sigma_{H,b}$, $\sigma_{h,b}$ and $\sigma_{H,b}$ trend at 0.5 km depth plotted along with corresponding theoretical probability density functions.*

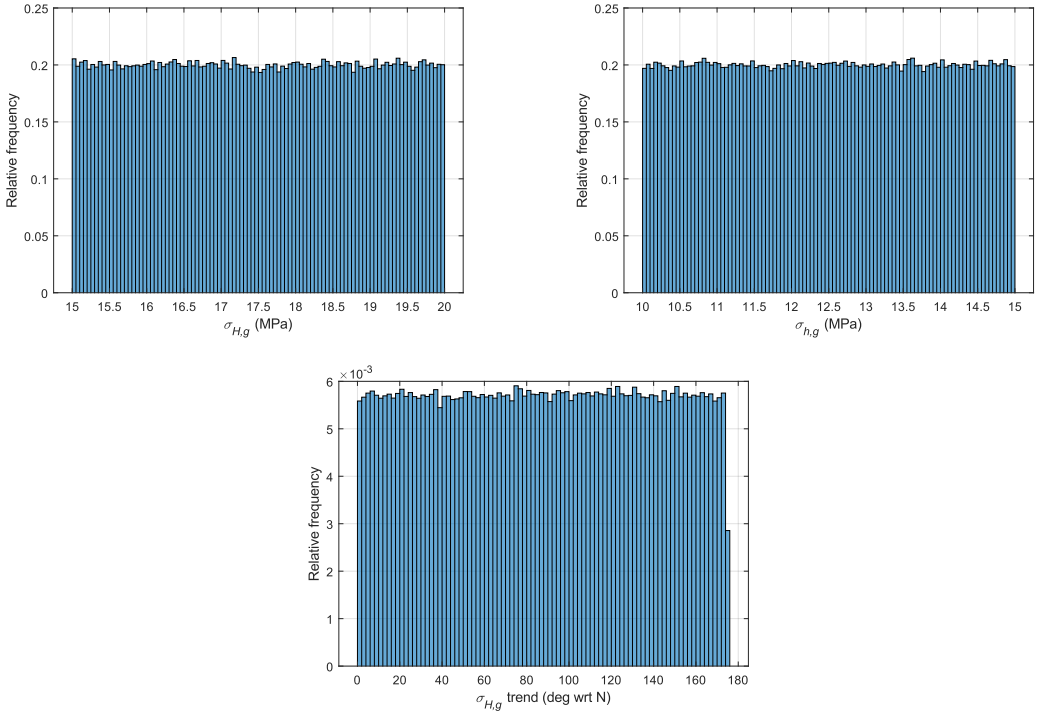

Figure 7-4. *Histograms showing the uniform distributions of $\sigma_{H,g}$, $\sigma_{h,g}$ and $\sigma_{H,g}$ trend for endglacial conditions.*

8 Appendix 2

Glacial stress evolutions

Here, temporal evolutions of the glacial stresses and their orientations for all ice models are presented. There are two stress components which are mainly horizontal, $\sigma_{H,g}$ and $\sigma_{h,g}$. The third component, $\sigma_{v,g}$, is mainly vertical. The subscript "g" means "glacial". The $\sigma_{H,g}$ trend is taken with respect to North rotating eastwards. The $\sigma_{v,g}$ plunge means the angle of $\sigma_{v,g}$ with respect to the horizontal. Note that since the $\sigma_{v,g}$ plunge may deviate from 90°, $\sigma_{v,g}$ is not always vertical. From this it follows that the $\sigma_{H,g}$ and $\sigma_{h,g}$ components are not necessarily horizontal. The results are generated from the GIA results at 1.5 km depth.

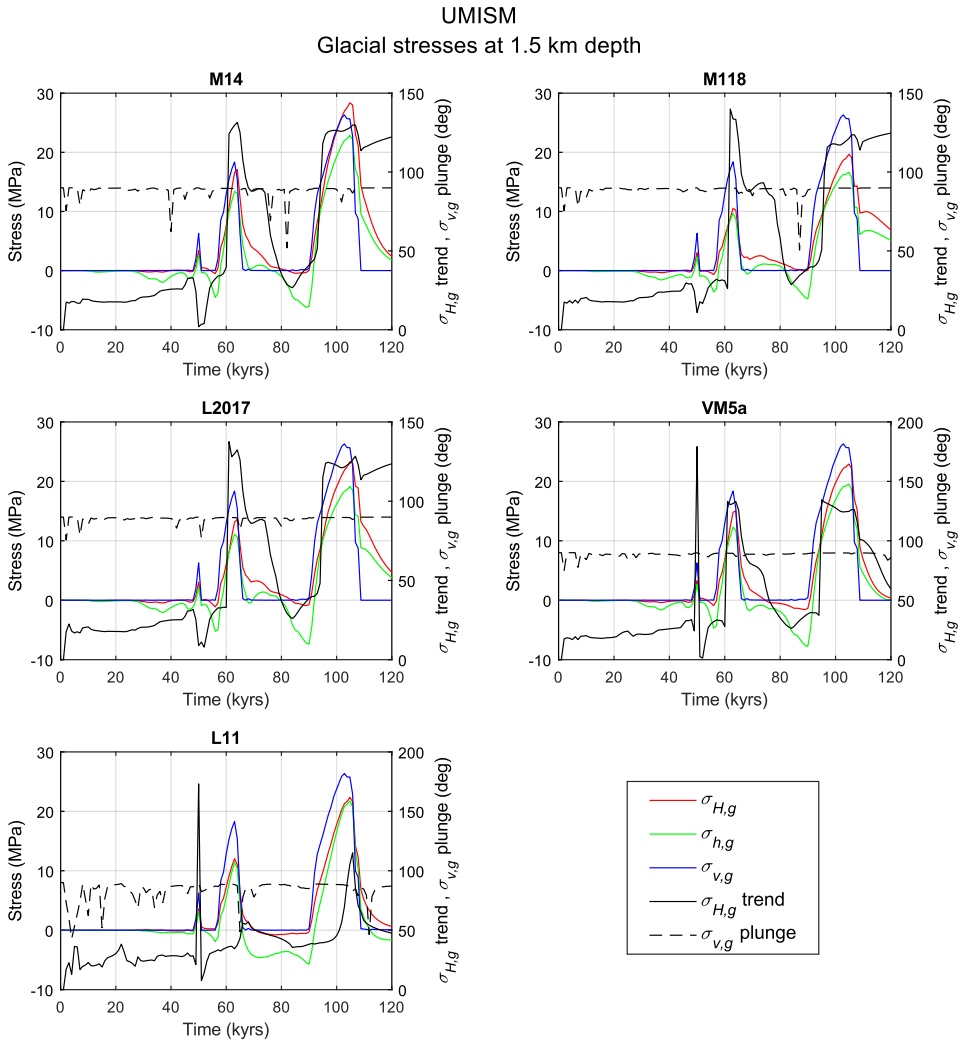

Figure 8-1. *Time evolutions at 1.5 km depth of $\sigma_{H,g}$, $\sigma_{h,g}$, $\sigma_{v,g}$, $\sigma_{H,g}$ trend and $\sigma_{v,g}$ plunge for the UMISM ice model and all five Earth models.*

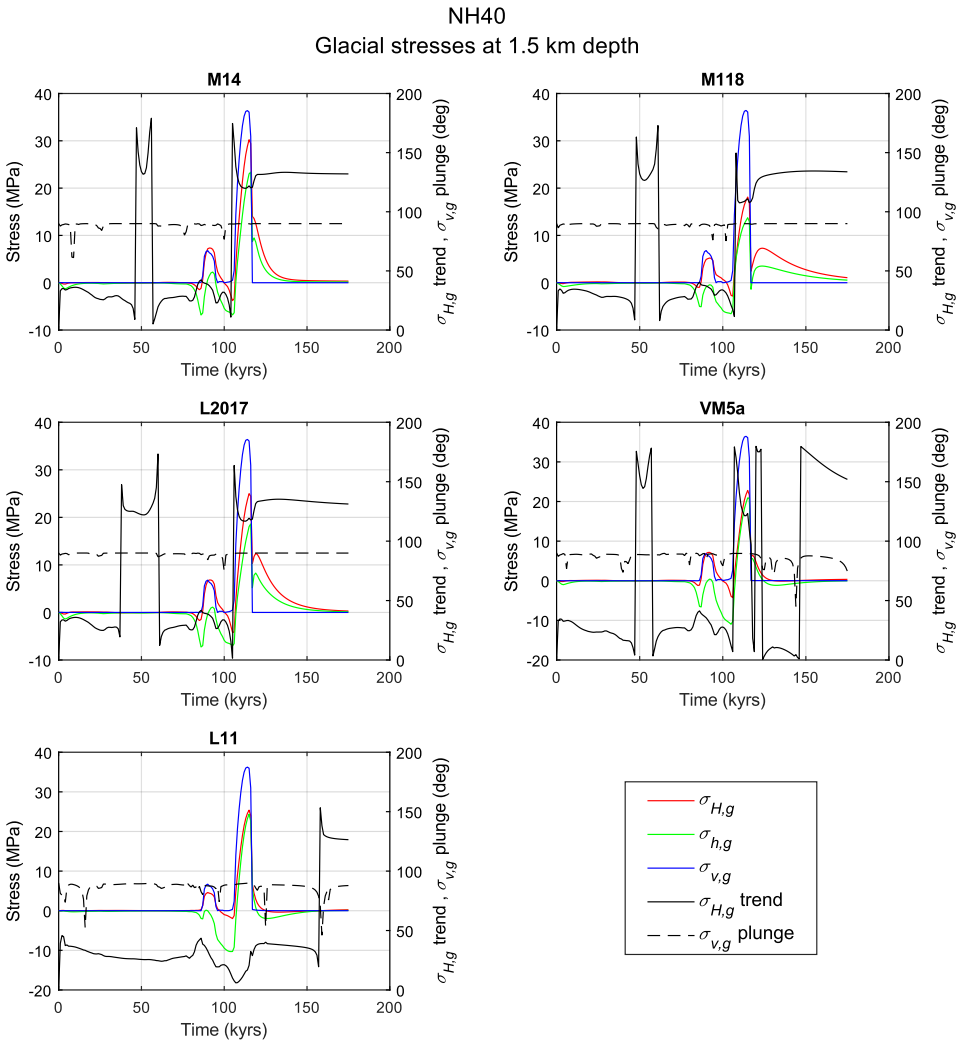

Figure 8-2. *Time evolutions at 1.5 km depth of $\sigma_{H,g}$, $\sigma_{h,g}$, $\sigma_{v,g}$, $\sigma_{H,g}$ trend and $\sigma_{v,g}$ plunge for the NH40 ice model and all five Earth models.*

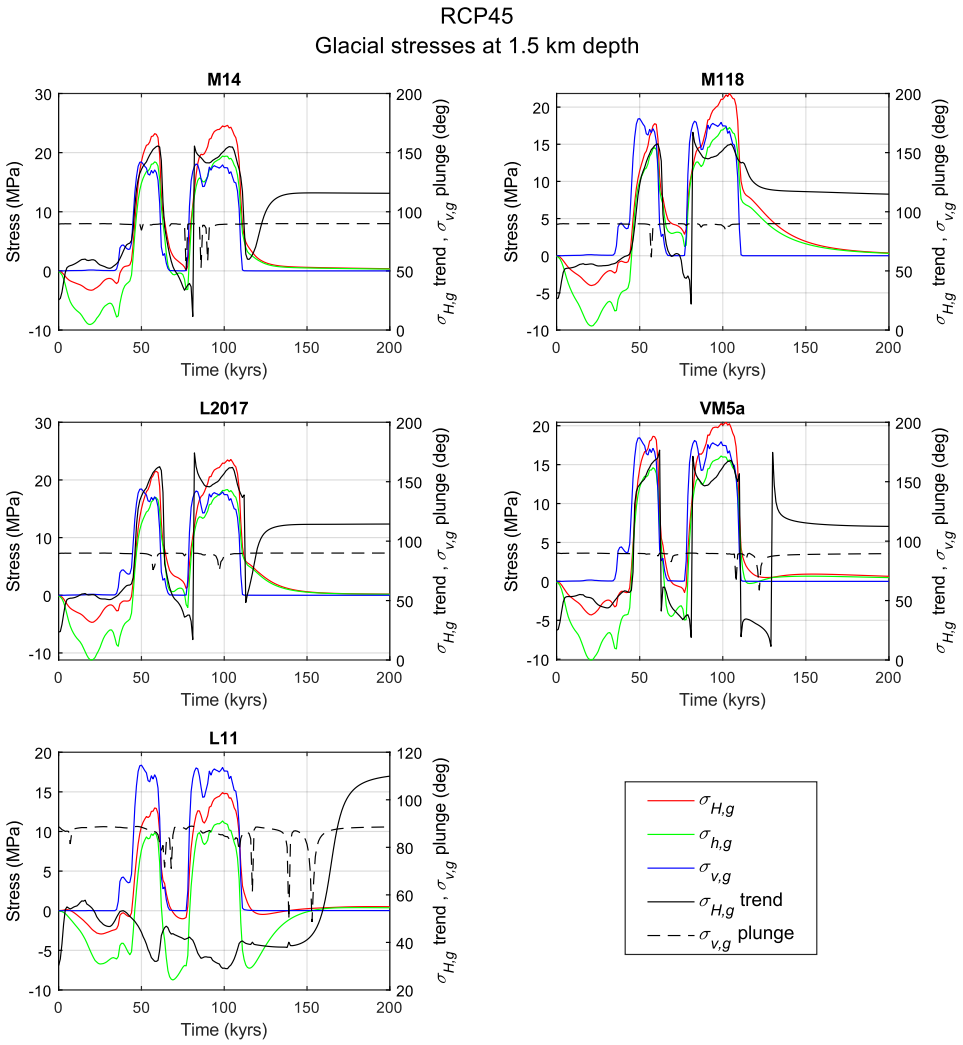

Figure 8-3. *Time evolutions at 1.5 km depth of $\sigma_{H,g}$, $\sigma_{h,g}$, $\sigma_{v,g}$, $\sigma_{H,g}$ trend and $\sigma_{v,g}$ plunge for the RCP45 ice model and all five Earth models.*

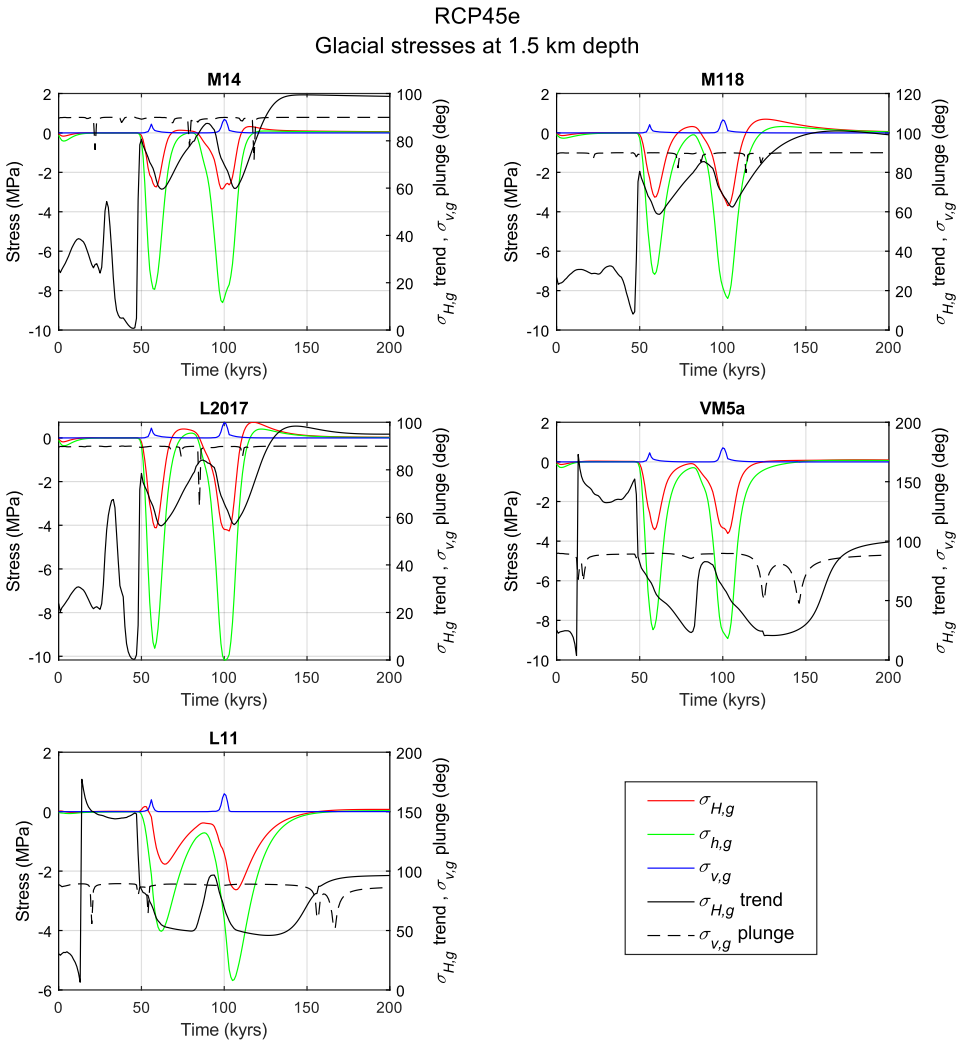

Figure 8-4. *Time evolutions at 1.5 km depth of $\sigma_{H,g}$, $\sigma_{h,g}$, $\sigma_{v,g}$, $\sigma_{H,g}$ trend and $\sigma_{v,g}$ plunge for the RCP45e ice model and all five Earth models.*

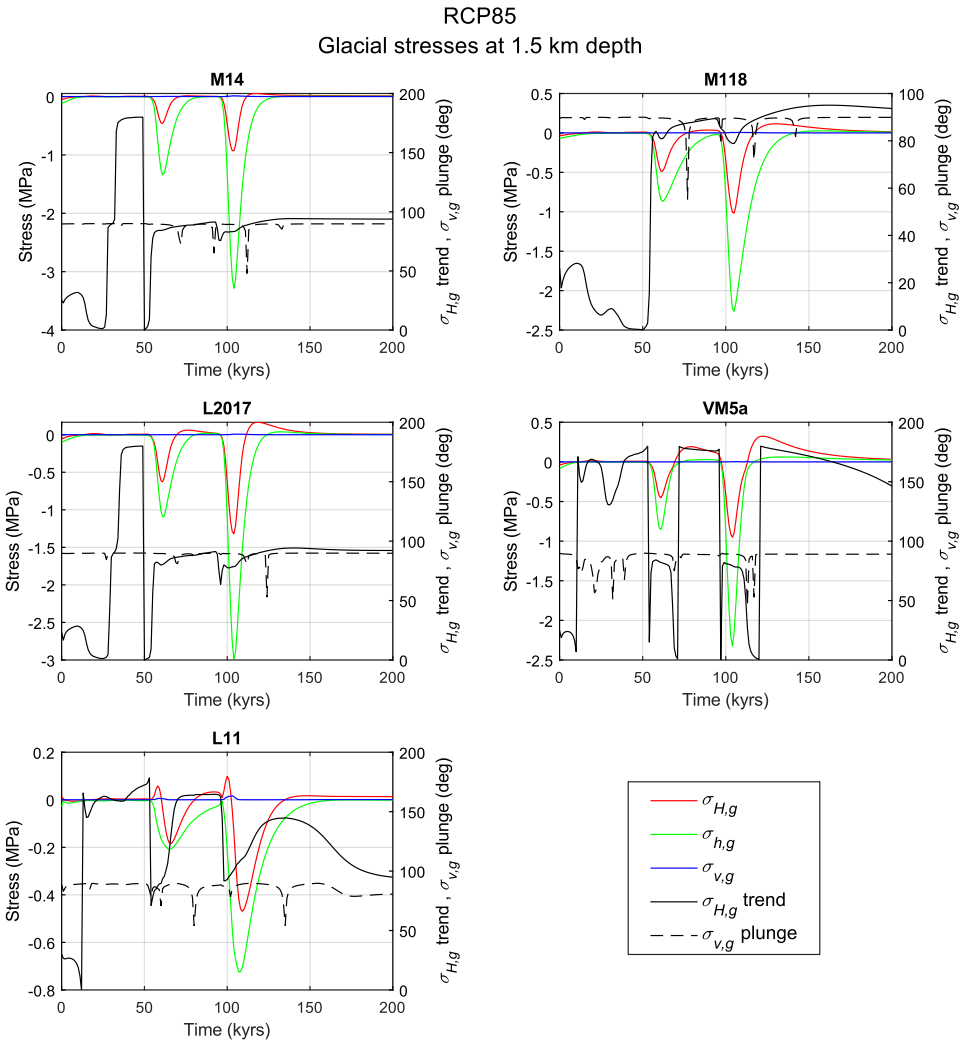

Figure 8-5. *Time evolutions at 1.5 km depth of $\sigma_{H,g}$, $\sigma_{h,g}$, $\sigma_{v,g}$, $\sigma_{H,g}$ trend and $\sigma_{v,g}$ plunge for the RCP85 ice model and all five Earth models.*

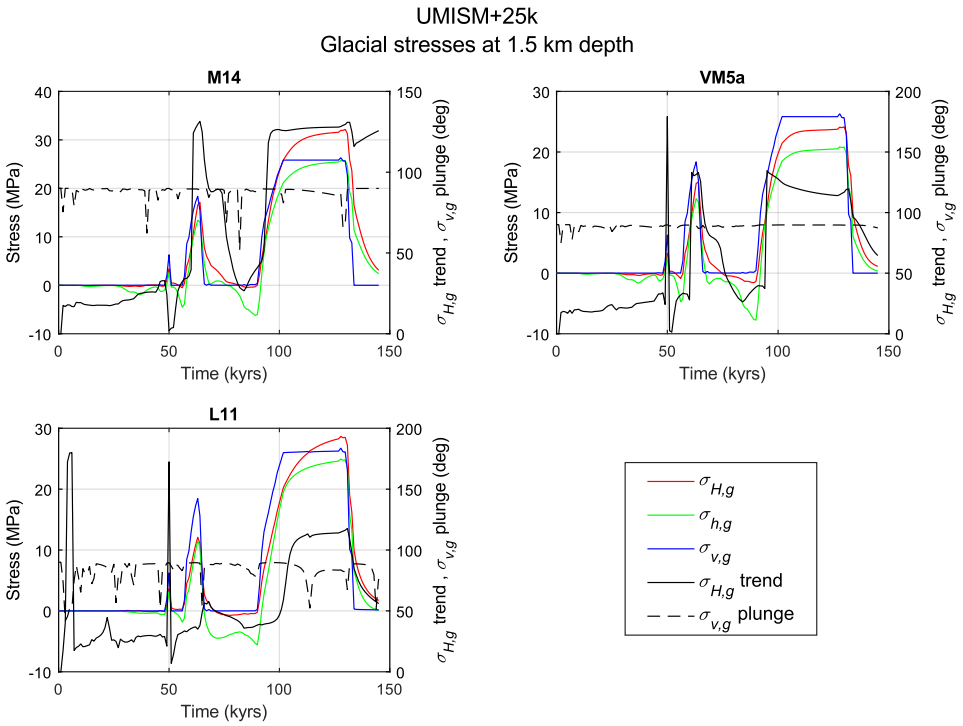

Figure 8-6. *Time evolutions at 1.5 km depth of $\sigma_{H,g}$, $\sigma_{h,g}$, $\sigma_{v,g}$, $\sigma_{H,g}$ trend and $\sigma_{v,g}$ plunge for the UMISM ice model with 25,000 years extended ice residence time (+25k).*

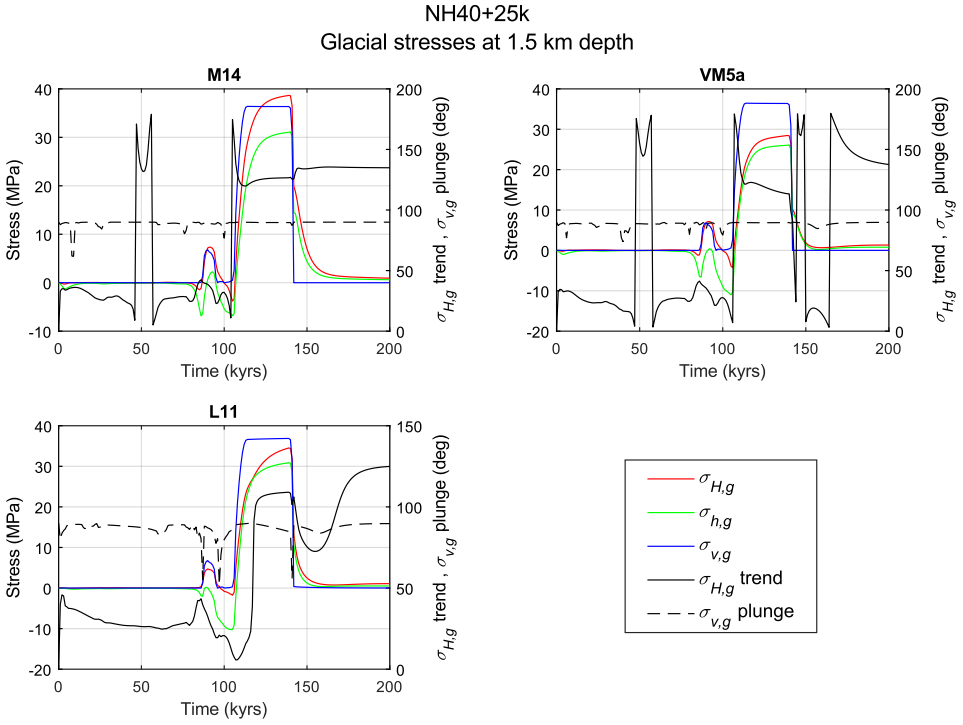

Figure 8-7. *Time evolutions at 1.5 km depth of $\sigma_{H,g}$, $\sigma_{h,g}$, $\sigma_{v,g}$, $\sigma_{H,g}$ trend and $\sigma_{v,g}$ plunge for the NH40 ice model with 25,000 years extended ice residence time (+25k).*

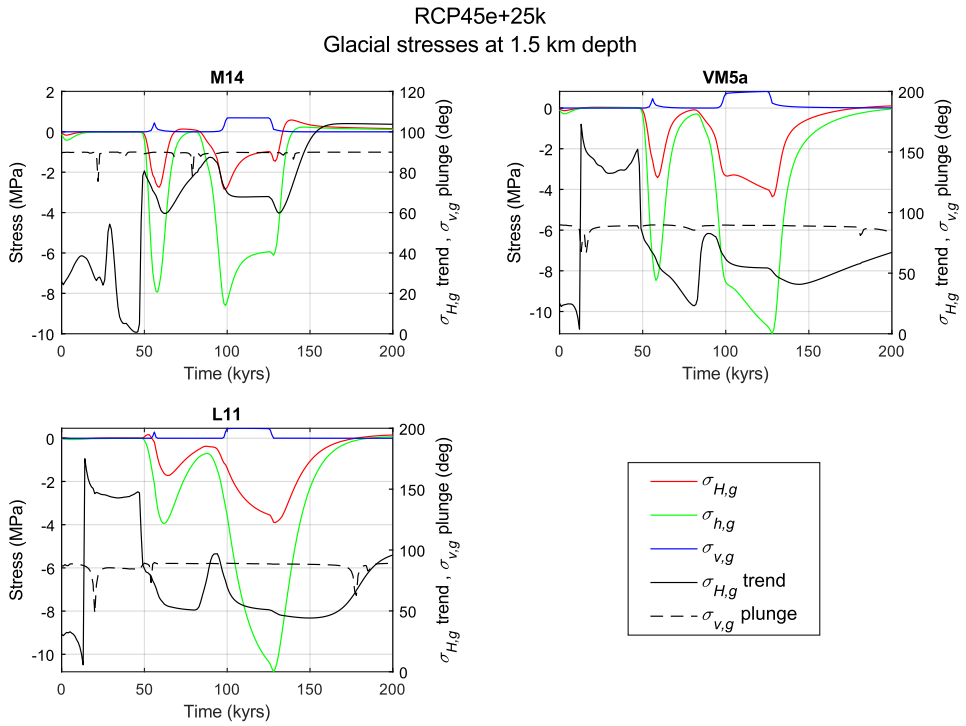

Figure 8-8. *Time evolutions at 1.5 km depth of $\sigma_{H,g}$, $\sigma_{h,g}$, $\sigma_{v,g}$, $\sigma_{H,g}$ trend and $\sigma_{v,g}$ plunge for the RCP45e ice model with 25,000 years extended ice residence time (+25k).*

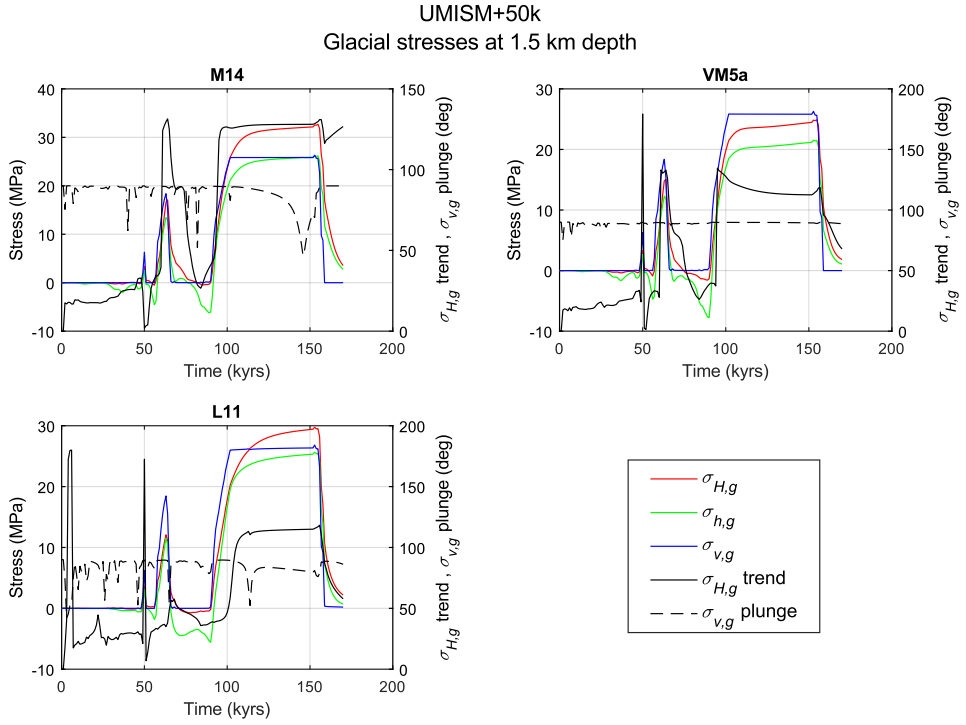

Figure 8-9. *Time evolutions at 1.5 km depth of $\sigma_{H,g}$, $\sigma_{h,g}$, $\sigma_{v,g}$, $\sigma_{H,g}$ trend and $\sigma_{v,g}$ plunge for the UMISM ice model with 50,000 years extended ice residence time (+50k).*

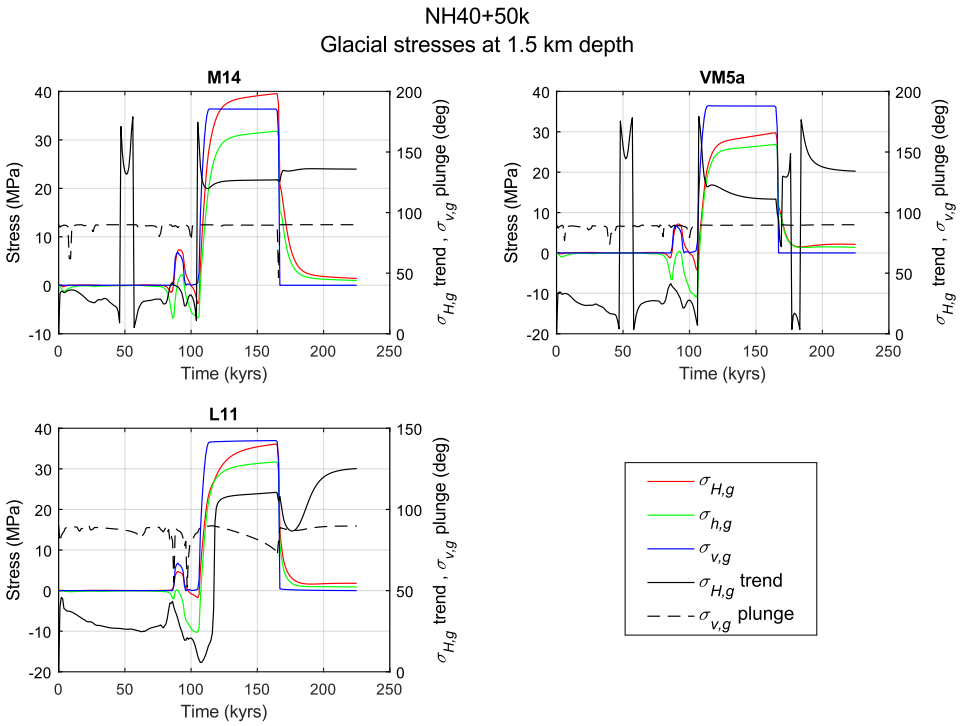

Figure 8-10. *Time evolutions at 1.5 km depth of $\sigma_{H,g}$, $\sigma_{h,g}$, $\sigma_{v,g}$, $\sigma_{H,g}$ trend and $\sigma_{v,g}$ plunge for the NH40 ice model with 50,000 years extended ice residence time (+50k).*

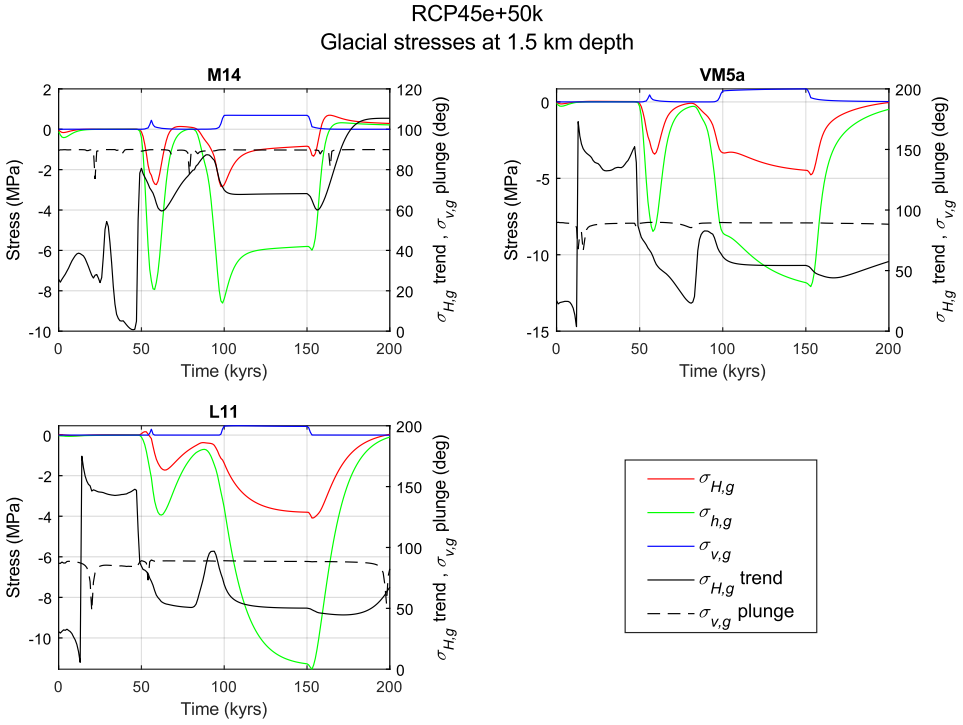

Figure 8-11. *Time evolutions at 1.5 km depth of $\sigma_{H,g}$, $\sigma_{h,g}$, $\sigma_{v,g}$, $\sigma_{H,g}$ trend and $\sigma_{v,g}$ plunge for the RCP45e ice model with 50,000 years extended ice residence time (+50k).*

9 Appendix 3

Temporal evolution of CFS

Here, temporal evolutions of *CFS* on all deformation zones are shown. Results for all ice/Earth model combinations are included. The results were calculated at 1.5 km depth.

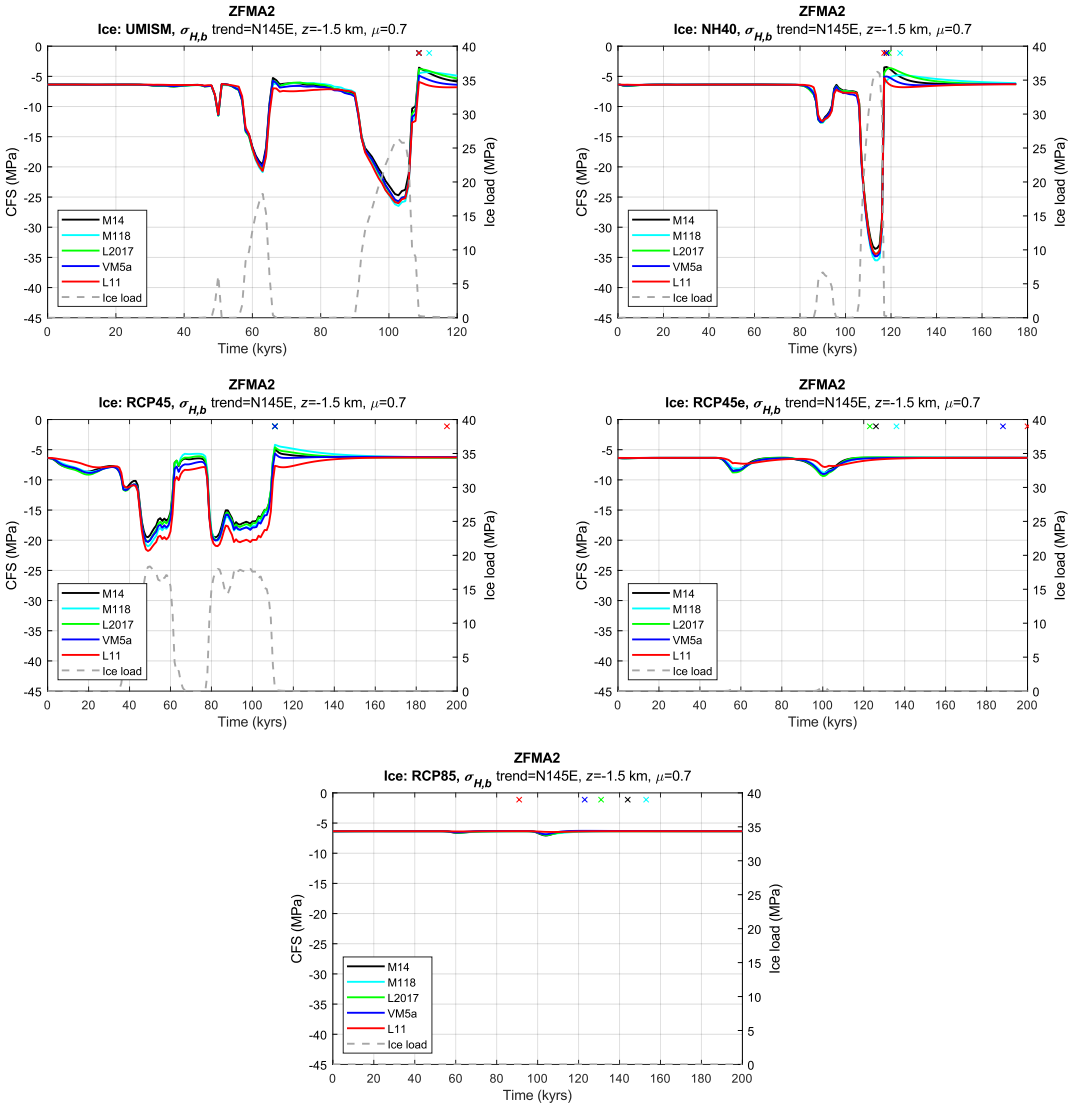

Figure 9-1. *Temporal evolutions of CFS at 1.5 km depth on ZFMA2 for the five different ice models plotted along with the vertical ice load. Each ice model is combined with the five Earth models. The coloured crosses indicate, for each Earth model, the time instance of max CFS.*

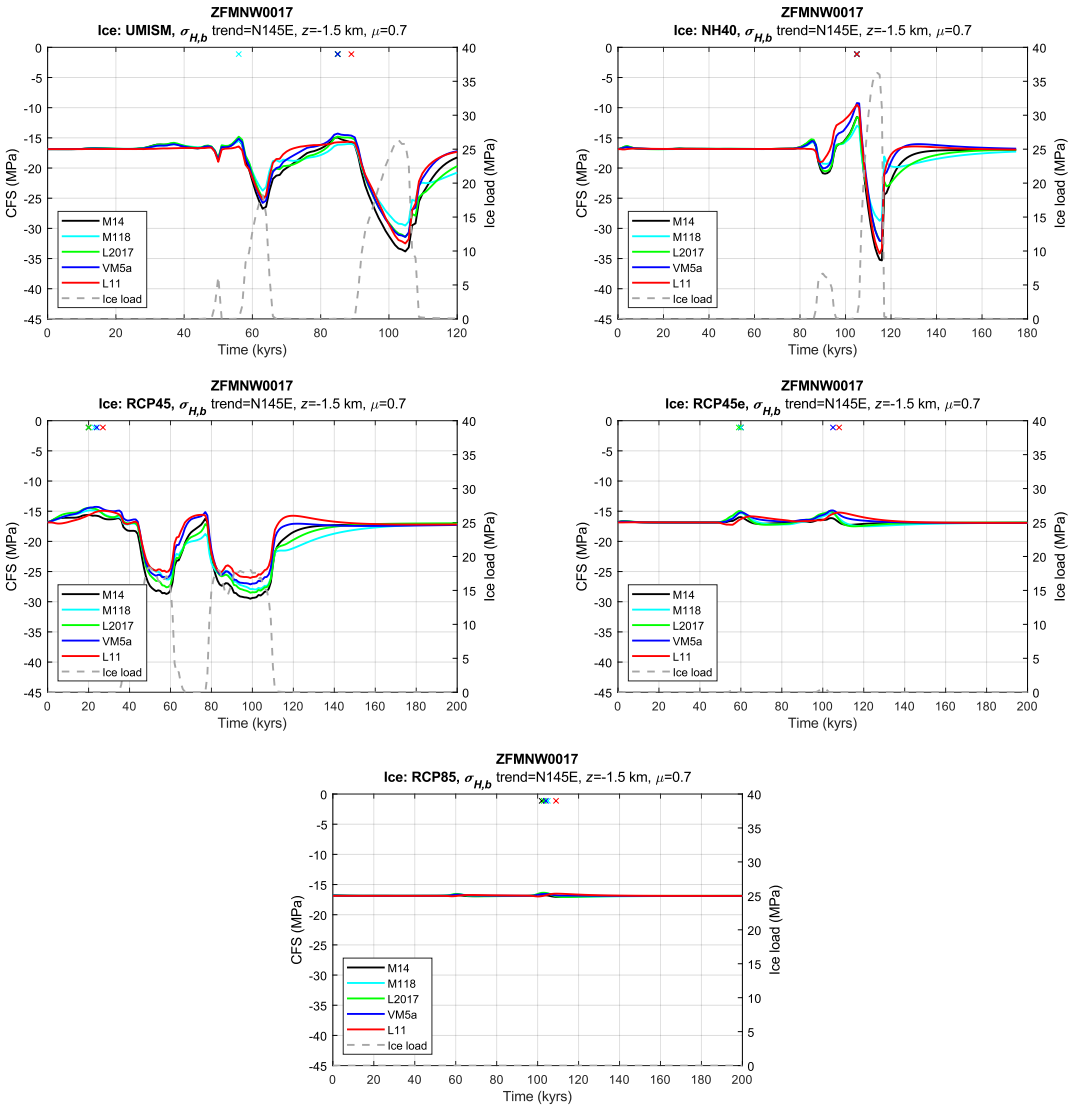

Figure 9-2. *Temporal evolutions of CFS at 1.5 km depth on ZFMNW0017 for the five different ice models plotted along with the vertical ice load. Each ice model is combined with the five Earth models. The coloured crosses indicate, for each Earth model, the time instance of max CFS.*

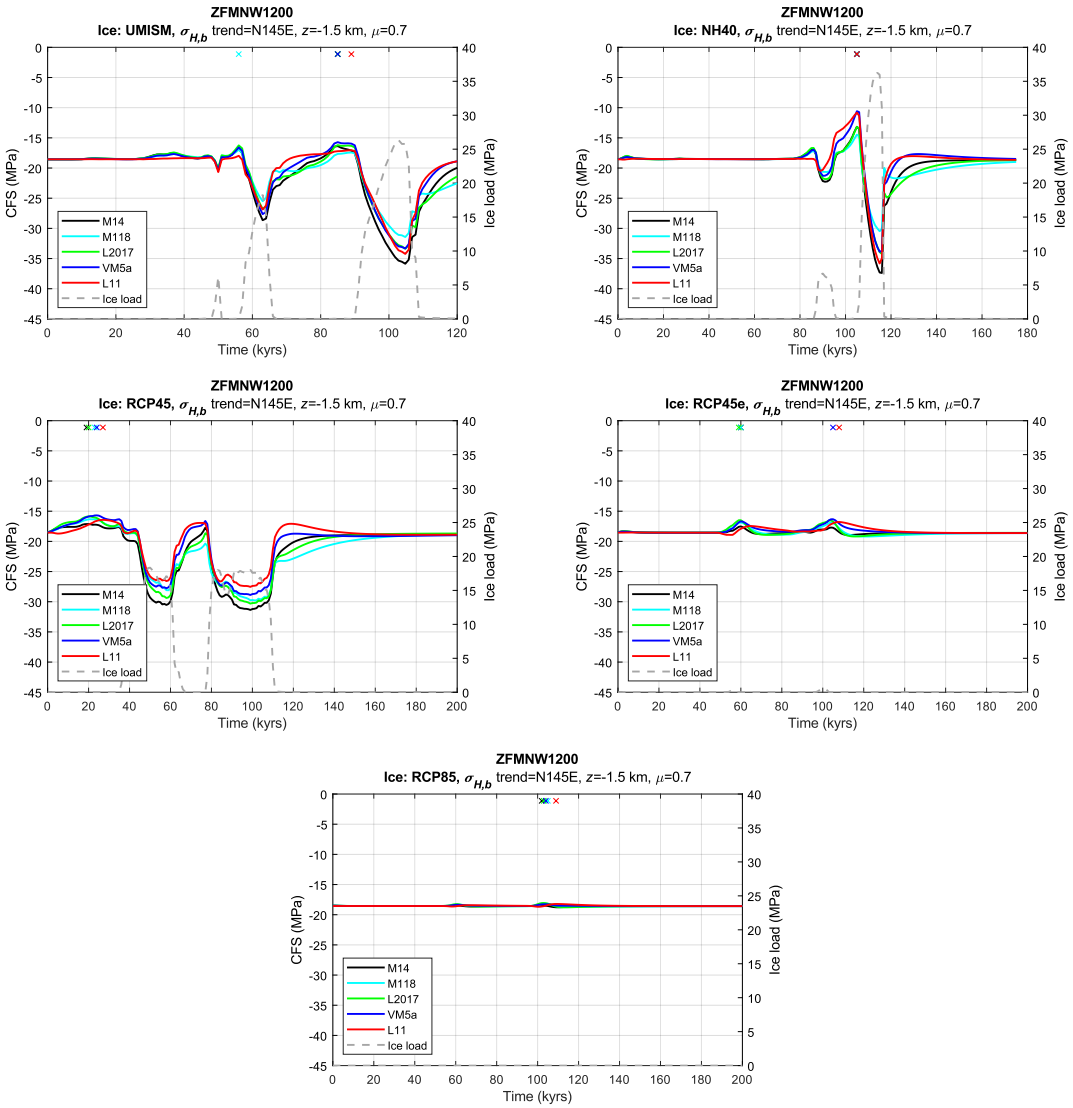

Figure 9-3. *Temporal evolutions of CFS at 1.5 km depth on ZFMNW1200 for the five different ice models plotted along with the vertical ice load. Each ice model is combined with the five Earth models. The coloured crosses indicate, for each Earth model, the time instance of max CFS.*

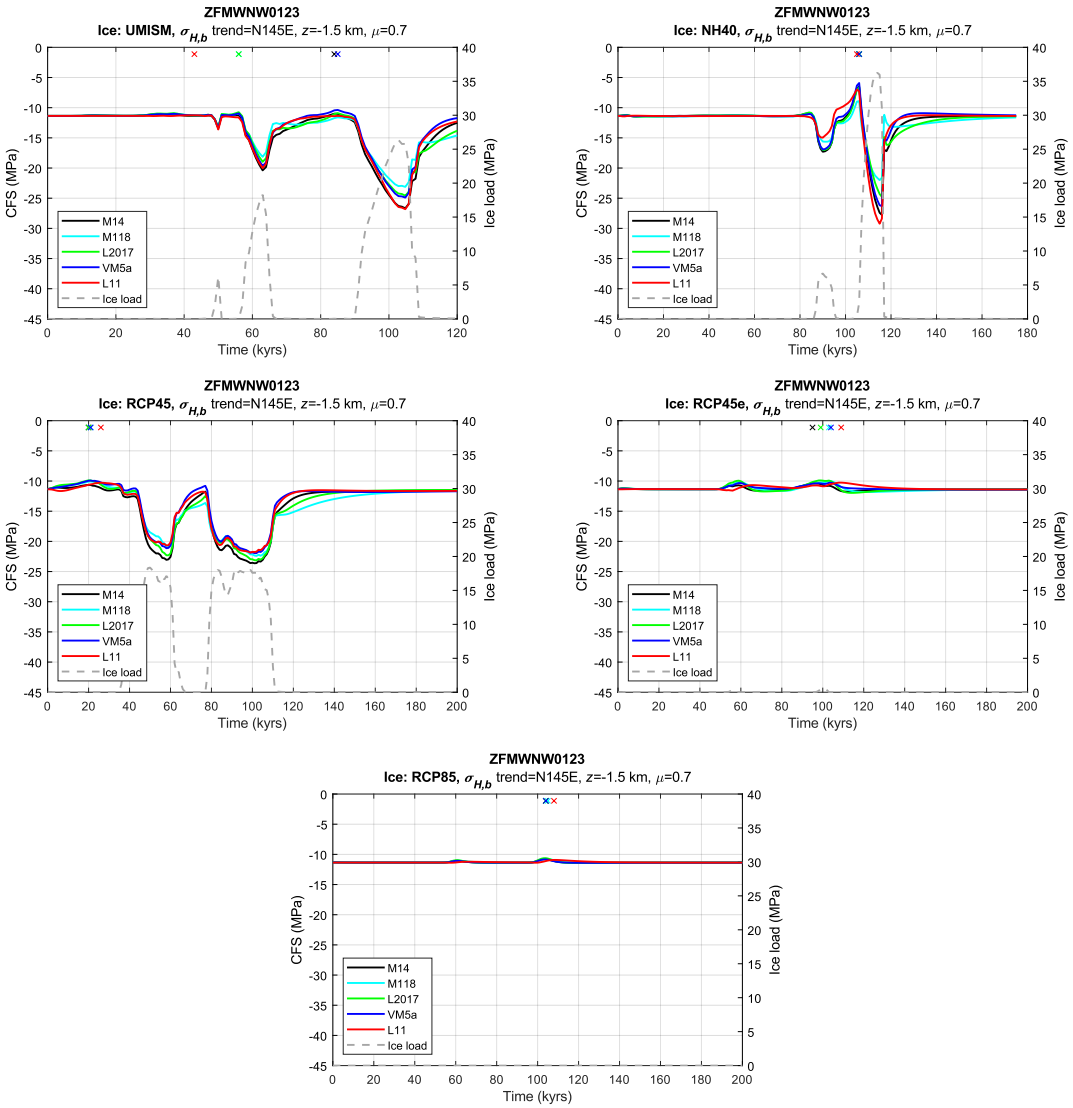

Figure 9-4. *Temporal evolutions of CFS at 1.5 km depth on ZFMWNW0123 for the five different ice models plotted along with the vertical ice load. Each ice model is combined with the five Earth models. The coloured crosses indicate, for each Earth model, the time instance of max CFS.*

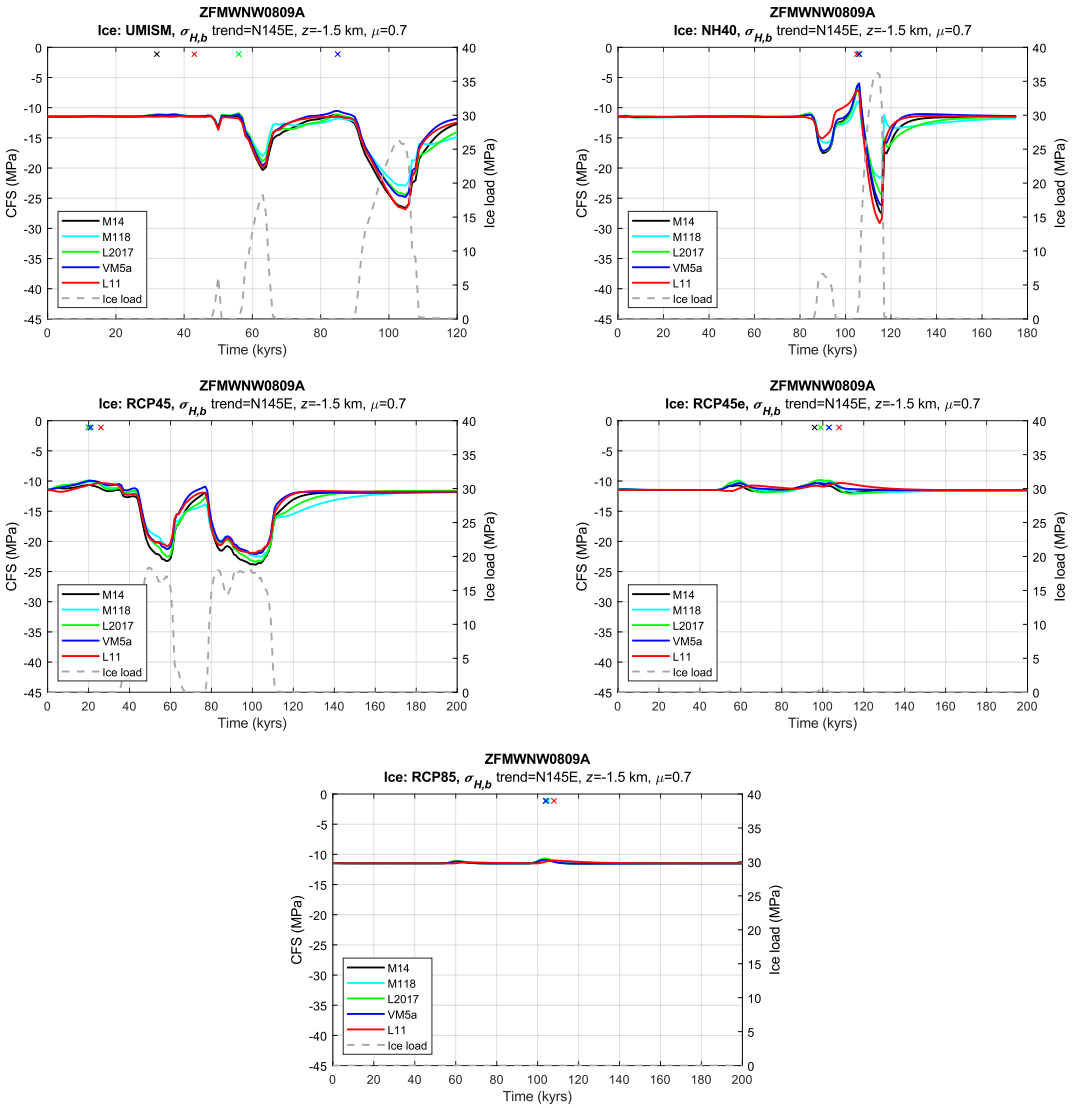

Figure 9-5. *Temporal evolutions of CFS at 1.5 km depth on ZFMWNW0809A for the five different ice models plotted along with the vertical ice load. Each ice model is combined with the five Earth models. The coloured crosses indicate, for each Earth model, the time instance of max CFS.*

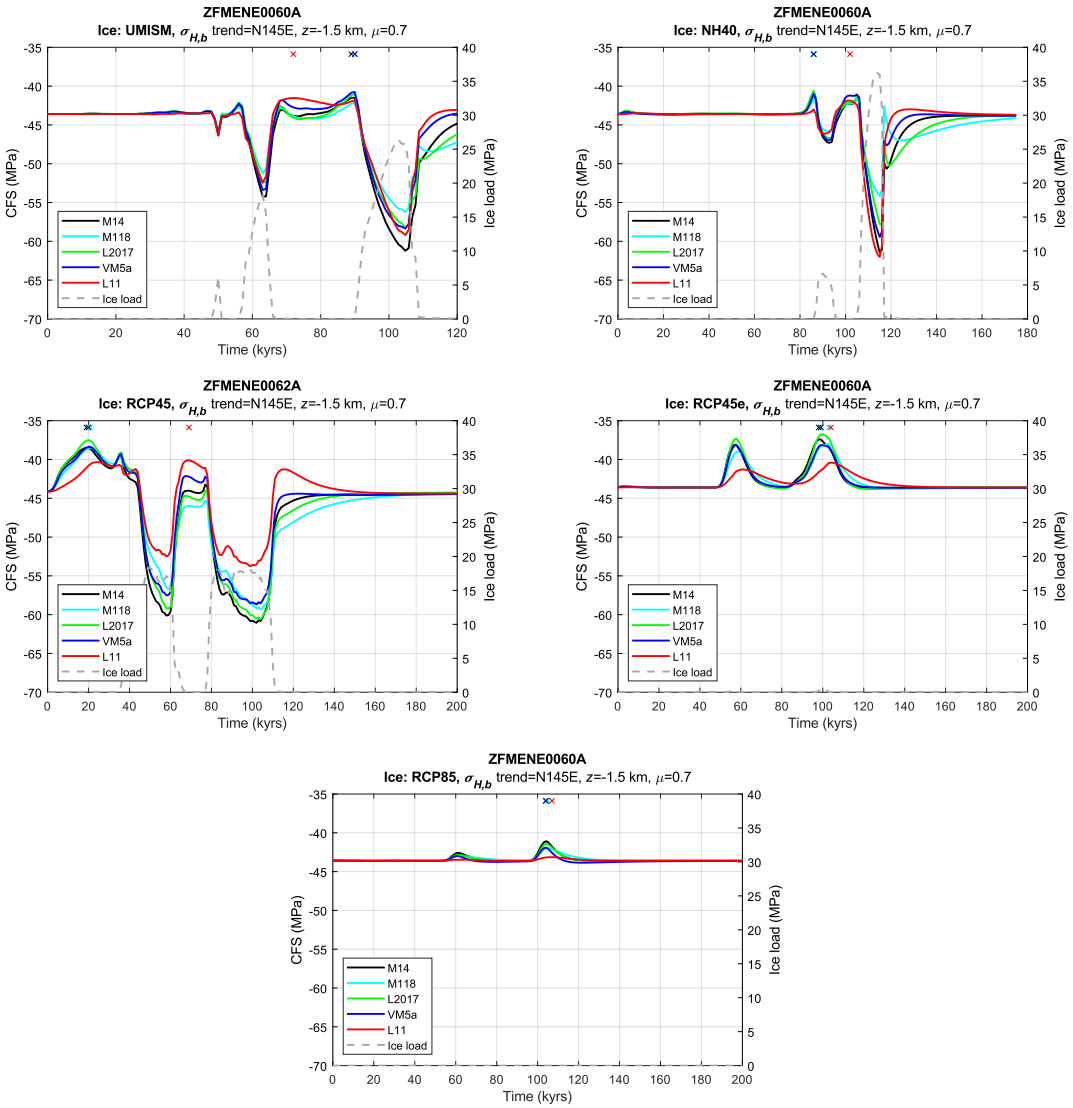

Figure 9-6. *Temporal evolutions of CFS at 1.5 km depth on ZFMENE0060A for the five different ice models plotted along with the vertical ice load. Each ice model is combined with the five Earth models. The coloured crosses indicate, for each Earth model, the time instance of max CFS.*

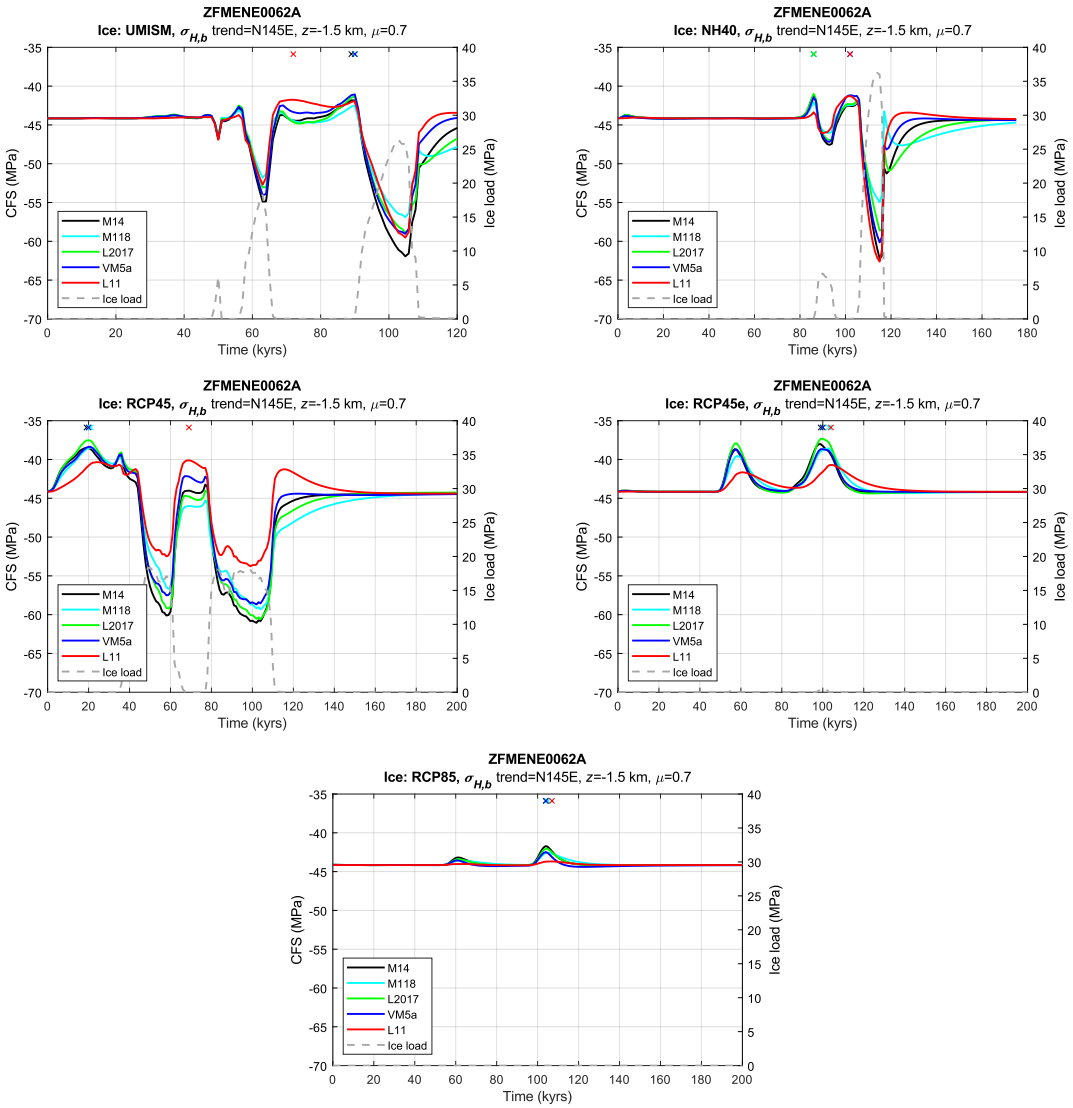

Figure 9-7. *Temporal evolutions of CFS at 1.5 km depth on ZFMENE0062A for the five different ice models plotted along with the vertical ice load. Each ice model is combined with the five Earth models. The coloured crosses indicate, for each Earth model, the time instance of max CFS.*

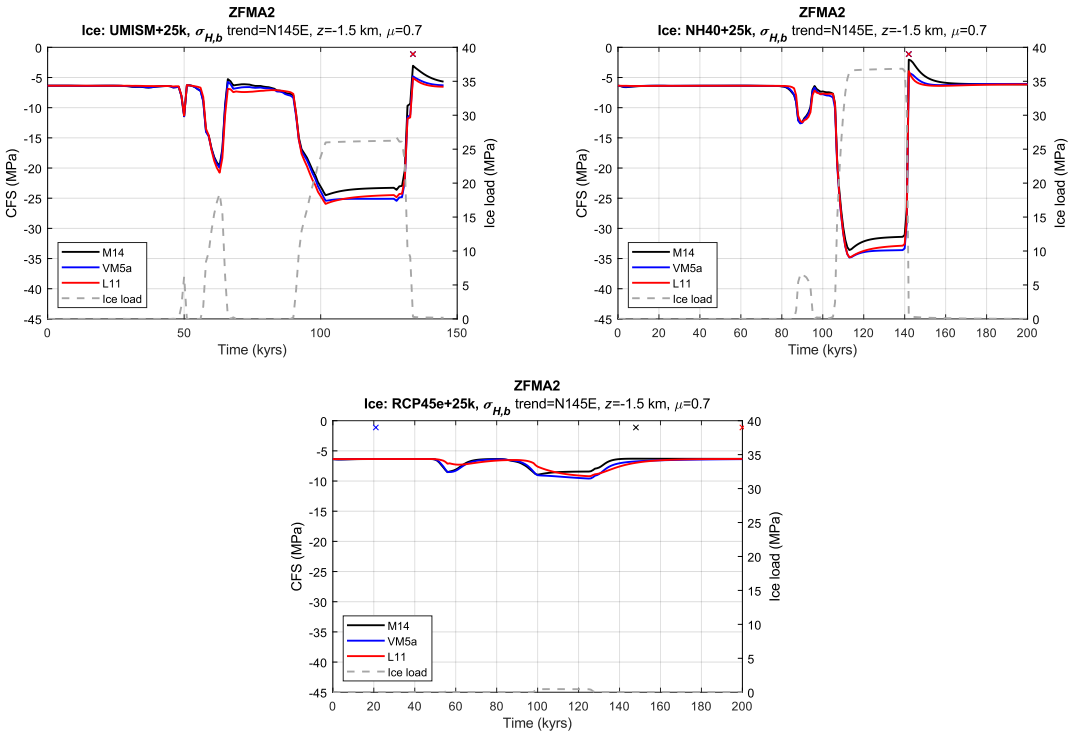

Figure 9-8. *Temporal evolutions of CFS at 1.5 km depth on ZFMA2 for the three ice models with 25,000 years extended ice residence time plotted along with the vertical ice load. Each ice model is combined with three Earth models. The coloured crosses indicate, for each Earth model, the time instance of max CFS.*

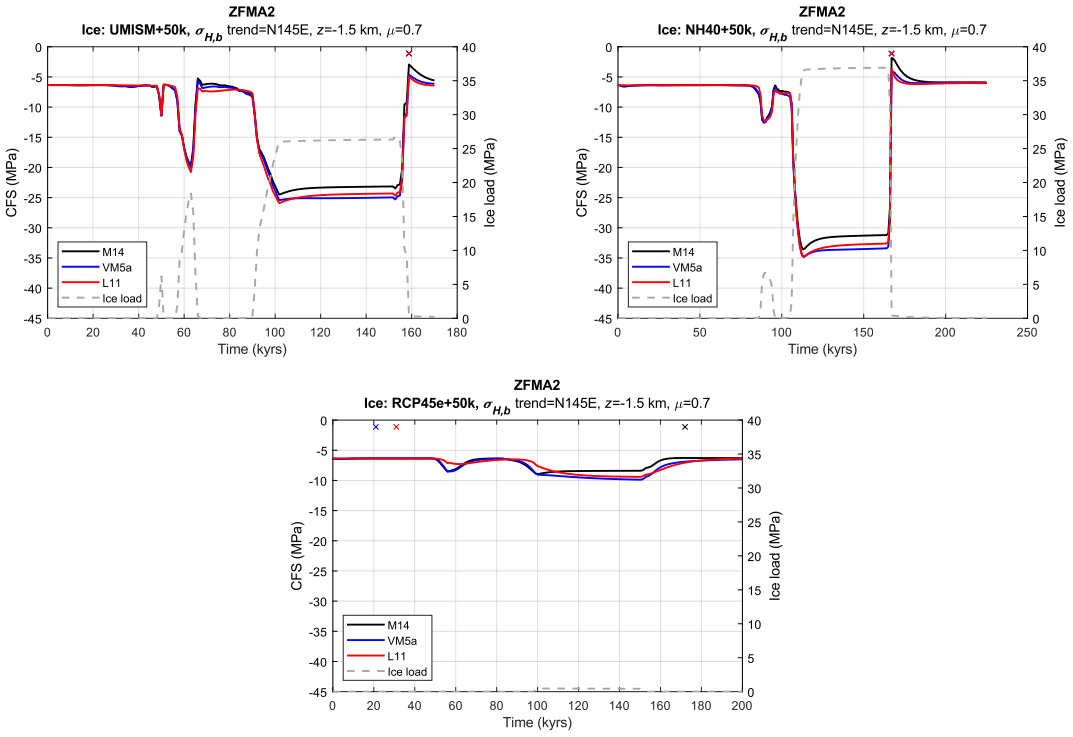

Figure 9-9. *Temporal evolutions of CFS at 1.5 km depth on ZFMA2 for the three ice models with 50,000 years extended ice residence time plotted along with the vertical ice load. Each ice model is combined with three Earth models. The coloured crosses indicate, for each Earth model, the time instance of max CFS.*

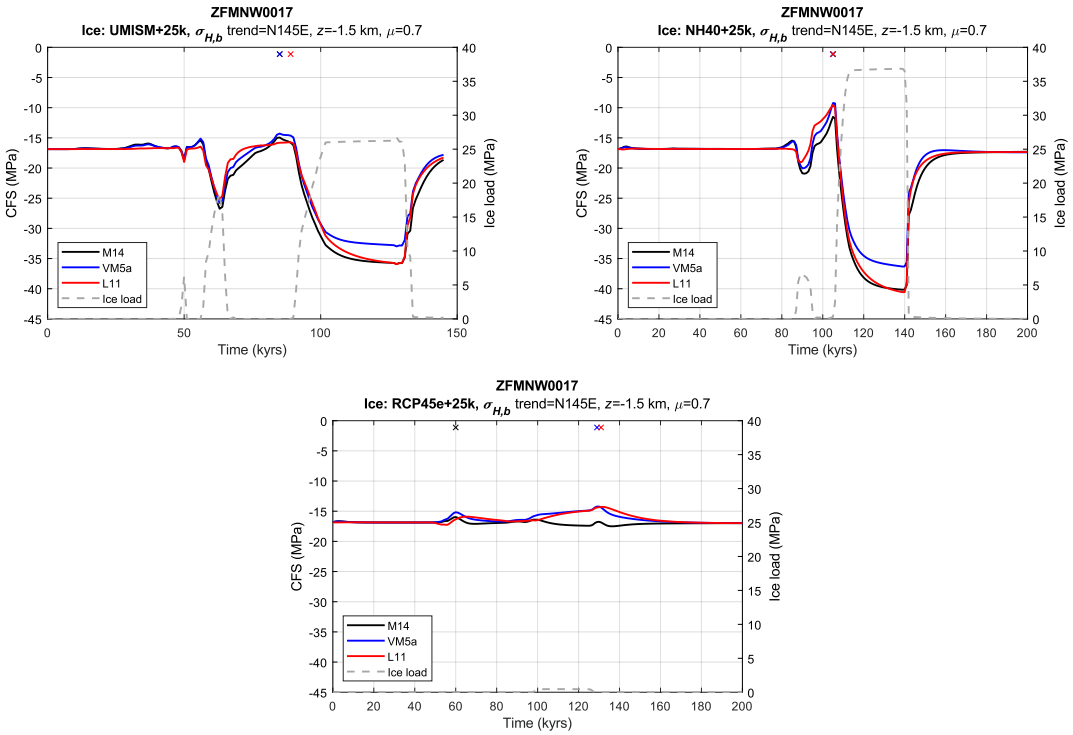

Figure 9-10. *Temporal evolutions of CFS at 1.5 km depth on ZFMNW0017 for the three ice models with 25,000 years extended ice residence time plotted along with the vertical ice load. Each ice model is combined with three Earth models. The coloured crosses indicate, for each Earth model, the time instance of max CFS.*

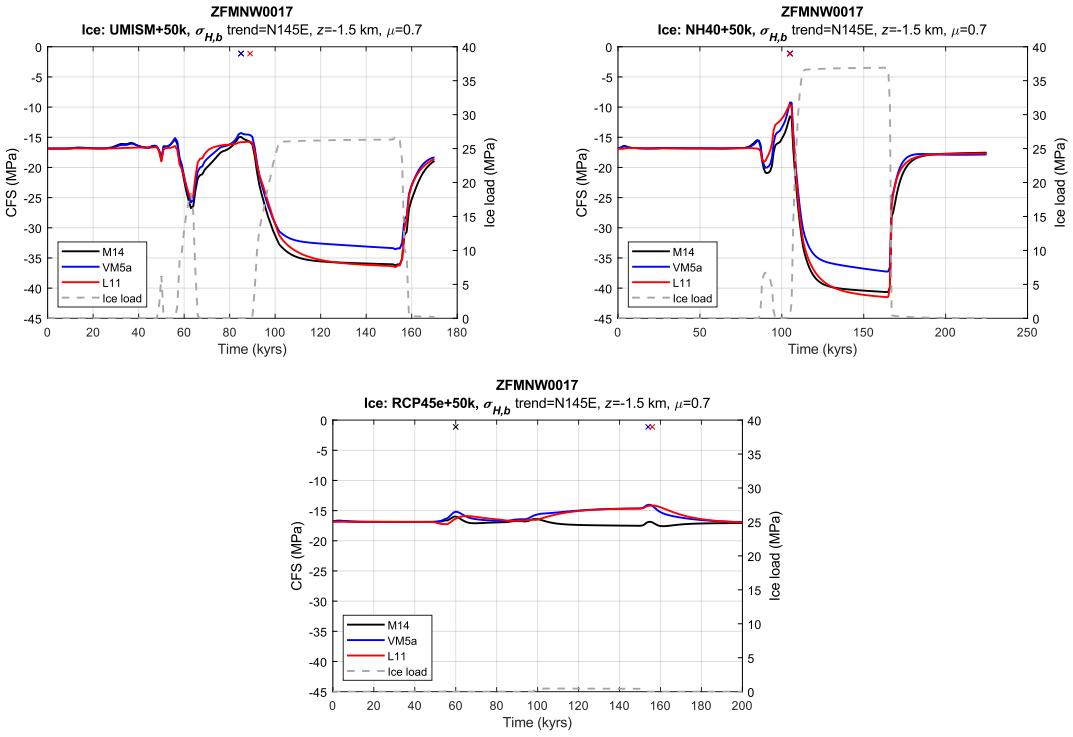

Figure 9-11. *Temporal evolutions of CFS at 1.5 km depth on ZFMNW0017 for the three ice models with 50,000 years extended ice residence time plotted along with the vertical ice load. Each ice model is combined with three Earth models. The coloured crosses indicate, for each Earth model, the time instance of max CFS.*

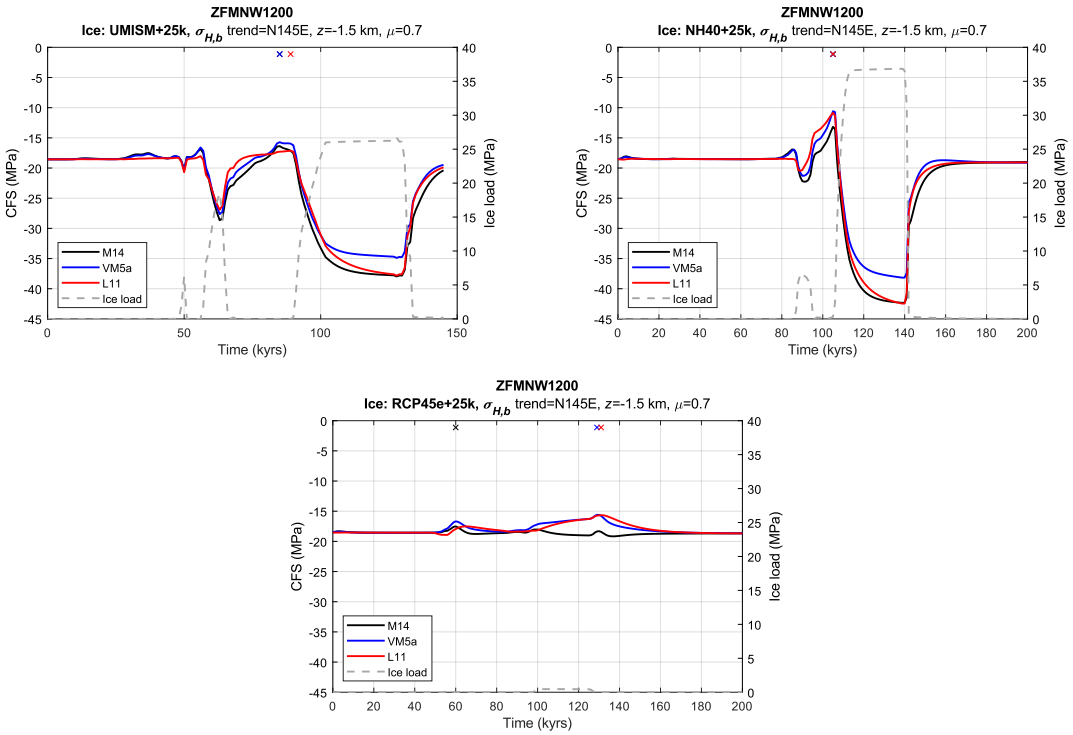

Figure 9-12. *Temporal evolutions of CFS at 1.5 km depth on ZFMNW1200 for the three ice models with 25,000 years extended ice residence time plotted along with the vertical ice load. Each ice model is combined with three Earth models. The coloured crosses indicate, for each Earth model, the time instance of max CFS.*

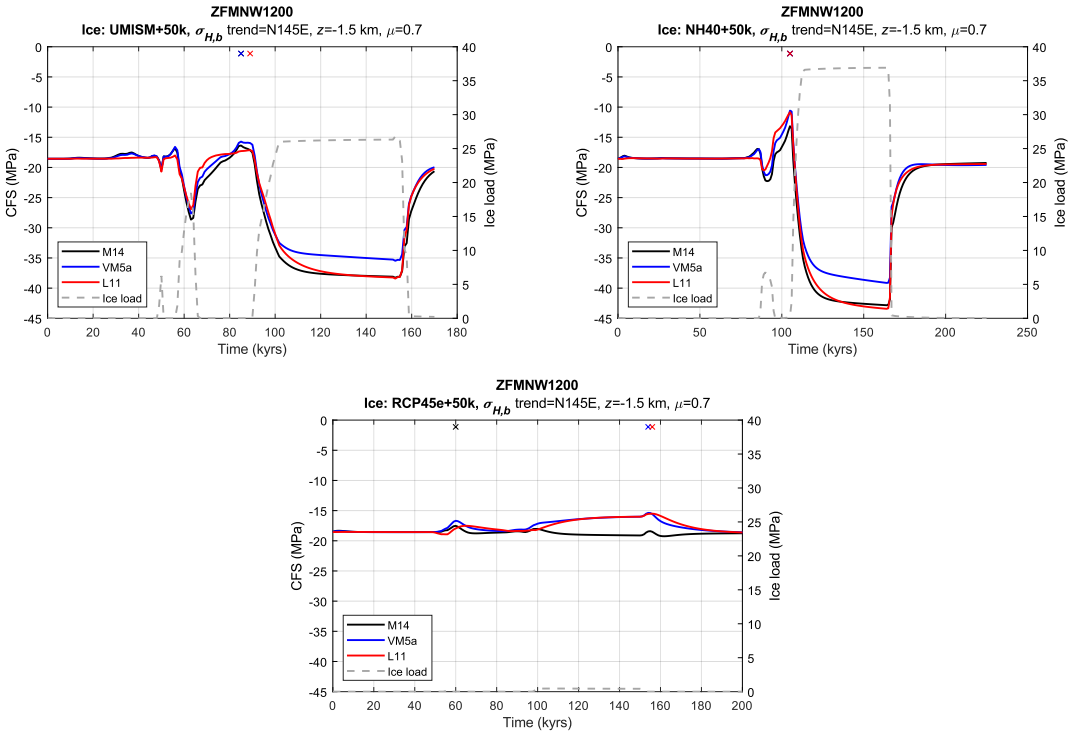

Figure 9-13. *Temporal evolutions of CFS at 1.5 km depth on ZFMNW1200 for the three ice models with 50,000 years extended ice residence time plotted along with the vertical ice load. Each ice model is combined with three Earth models. The coloured crosses indicate, for each Earth model, the time instance of max CFS.*

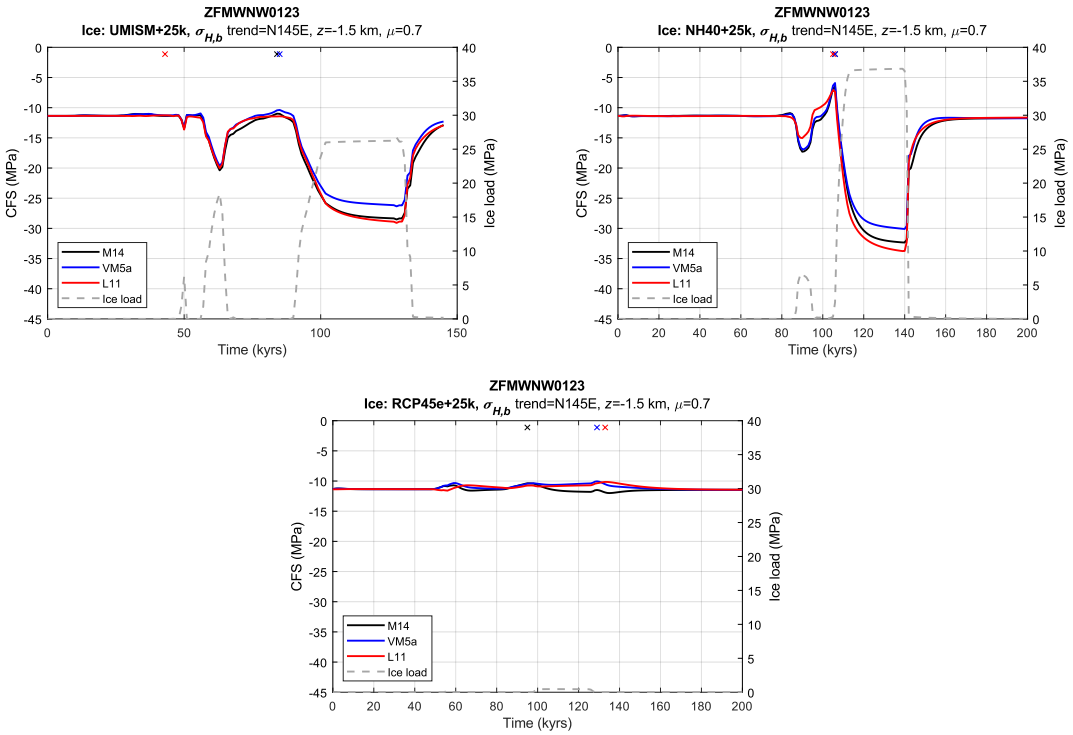

Figure 9-14. *Temporal evolutions of CFS at 1.5 km depth on ZFMWNW0123 for the three ice models with 25,000 years extended ice residence time plotted along with the vertical ice load. Each ice model is combined with three Earth models. The coloured crosses indicate, for each Earth model, the time instance of max CFS.*

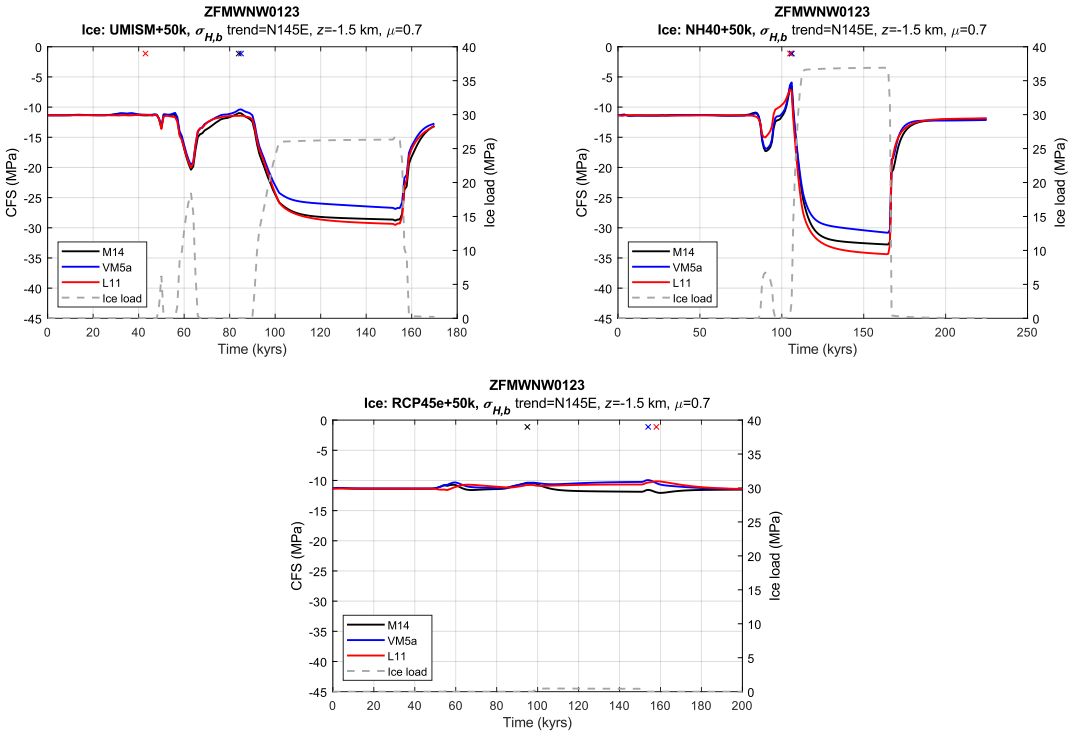

Figure 9-15. *Temporal evolutions of CFS at 1.5 km depth on ZFMWNW0123 for the three ice models with 50,000 years extended ice residence time plotted along with the vertical ice load. Each ice model is combined with three Earth models. The coloured crosses indicate, for each Earth model, the time instance of max CFS.*

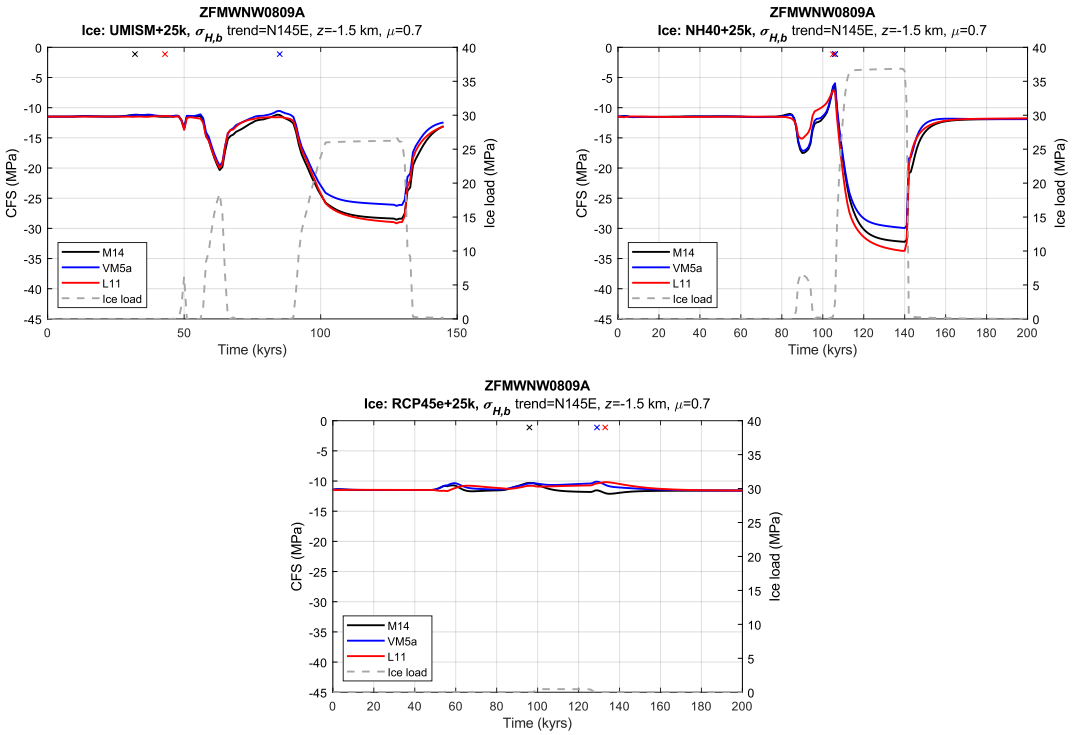

Figure 9-16. *Temporal evolutions of CFS at 1.5 km depth on ZFMWNW0809A for the three ice models with 25,000 years extended ice residence time plotted along with the vertical ice load. Each ice model is combined with three Earth models. The coloured crosses indicate, for each Earth model, the time instance of max CFS.*

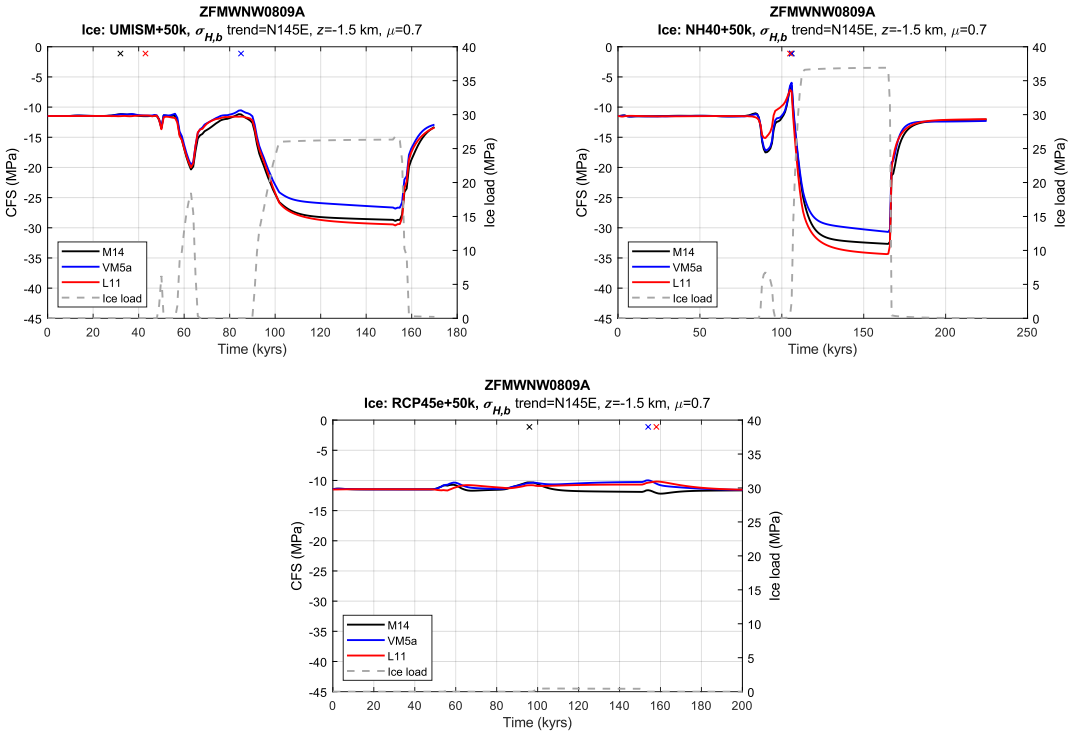

Figure 9-17. *Temporal evolutions of CFS at 1.5 km depth on ZFMWNW0809A for the three ice models with 50,000 years extended ice residence time plotted along with the vertical ice load. Each ice model is combined with three Earth models. The coloured crosses indicate, for each Earth model, the time instance of max CFS.*

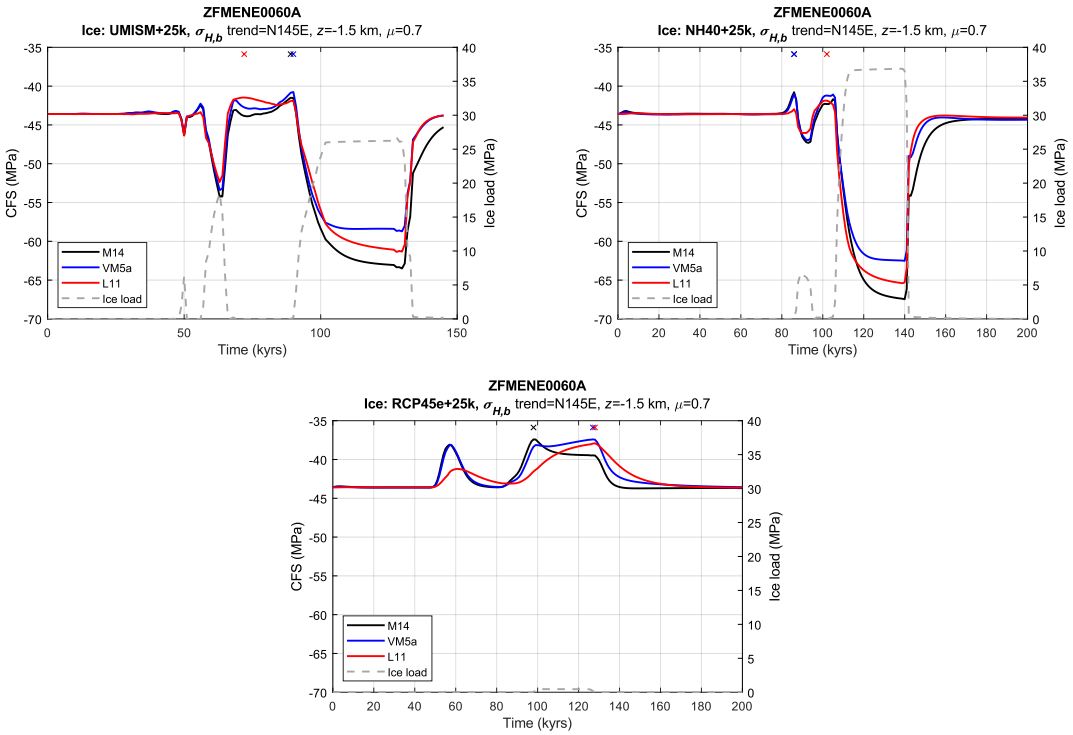

Figure 9-18. *Temporal evolutions of CFS at 1.5 km depth on ZFMENE0060A for the three ice models with 25,000 years extended ice residence time plotted along with the vertical ice load. Each ice model is combined with three Earth models. The coloured crosses indicate, for each Earth model, the time instance of max CFS.*

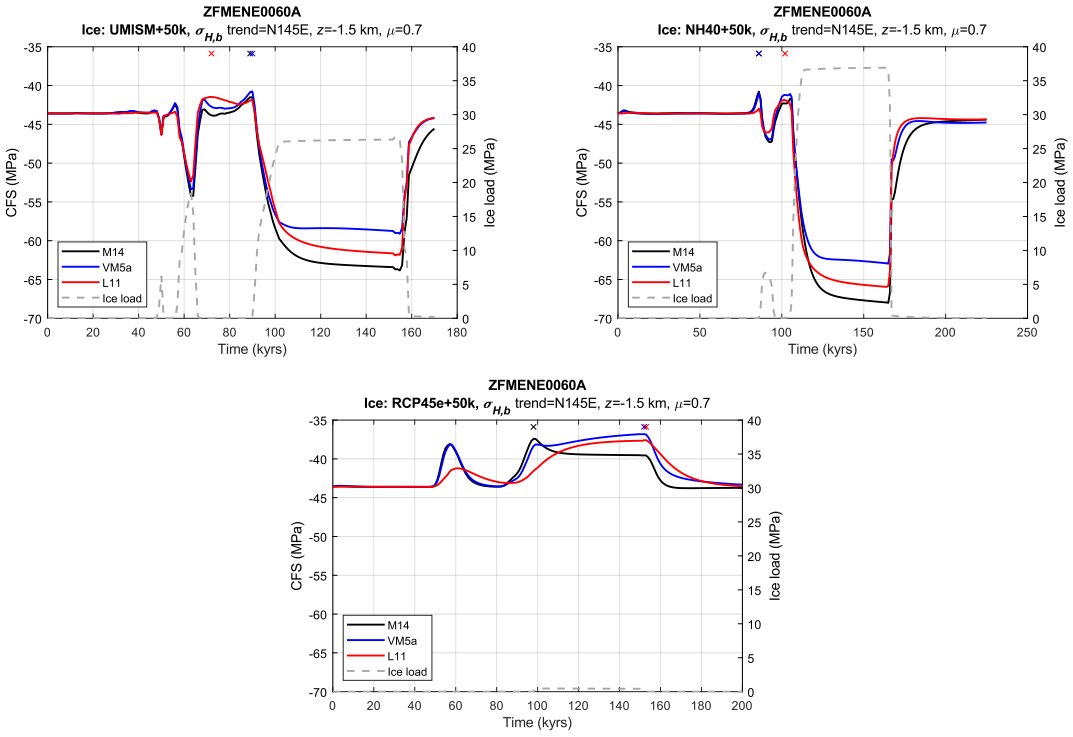

Figure 9-19. *Temporal evolutions of CFS at 1.5 km depth on ZFMENE0060A for the three ice models with 50,000 years extended ice residence time plotted along with the vertical ice load. Each ice model is combined with three Earth models. The coloured crosses indicate, for each Earth model, the time instance of max CFS.*

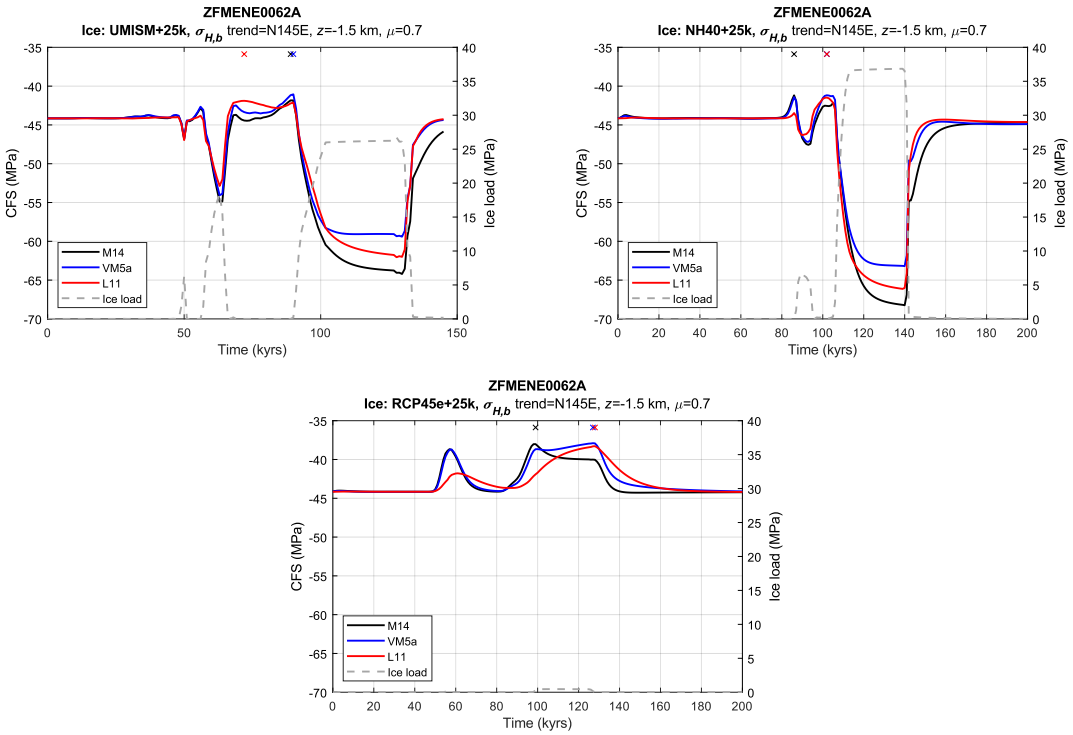

Figure 9-20. *Temporal evolutions of CFS at 1.5 km depth on ZFMENE0062A for the three ice models with 25,000 years extended ice residence time plotted along with the vertical ice load. Each ice model is combined with three Earth models. The coloured crosses indicate, for each Earth model, the time instance of max CFS.*

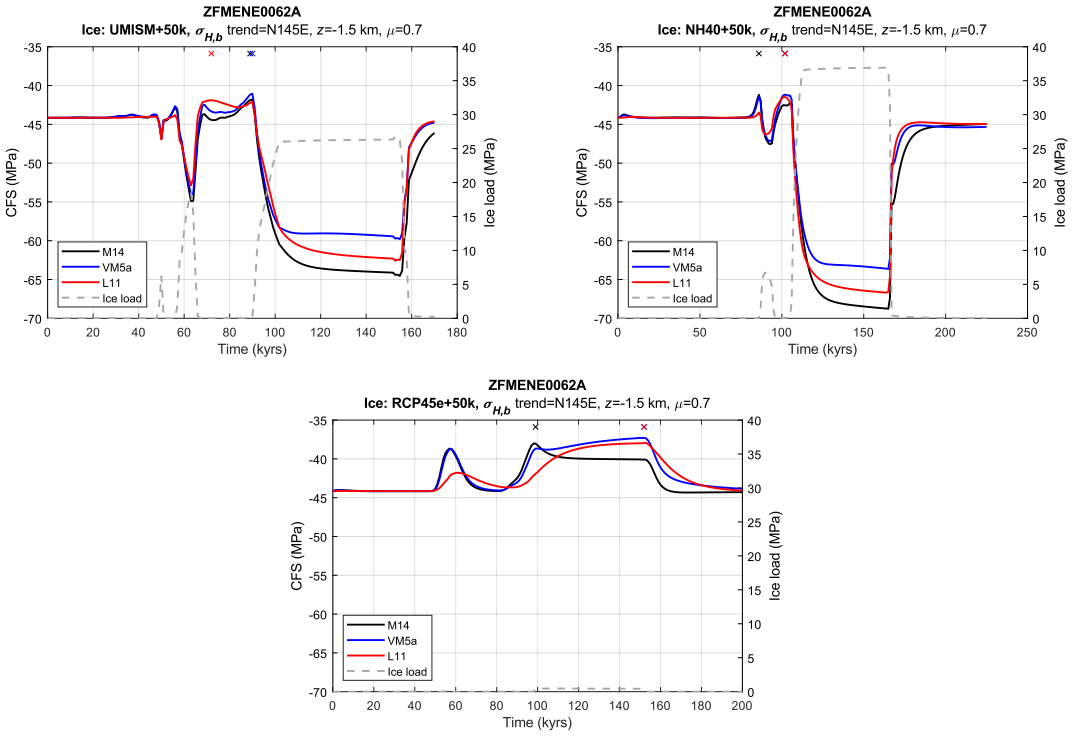

Figure 9-21. *Temporal evolutions of CFS at 1.5 km depth on ZFMENE0062A for the three ice models with 50,000 years extended ice residence time plotted along with the vertical ice load. Each ice model is combined with three Earth models. The coloured crosses indicate, for each Earth model, the time instance of max CFS.*

10 Appendix 4

Effect of the number of realisations *N*

Figure 10-1 and Figure 10-2 show *CFS* as function of depth for ZFMA2 and ZFMNW0017, respectively. The plots illustrate the effect of using different numbers of realisations *N* when generating the input parameter distributions. Based on the results depicted in Figure 10-1 and Figure 10-2, the probability of having $CFS > 0$ was calculated. These results are plotted in Figure 10-3.

The contours in Figure 10-1 and Figure 10-2 indicate that the solution appears to stabilise when $N > 300{,}000$. In Figure 10-3 only minor changes in the results for *N* above 500,000 can be seen, even when using logarithmic *x*-axis scale in the diagrams. In the Monte-Carlo simulations performed in this study, $N = 500{,}000$ was used.

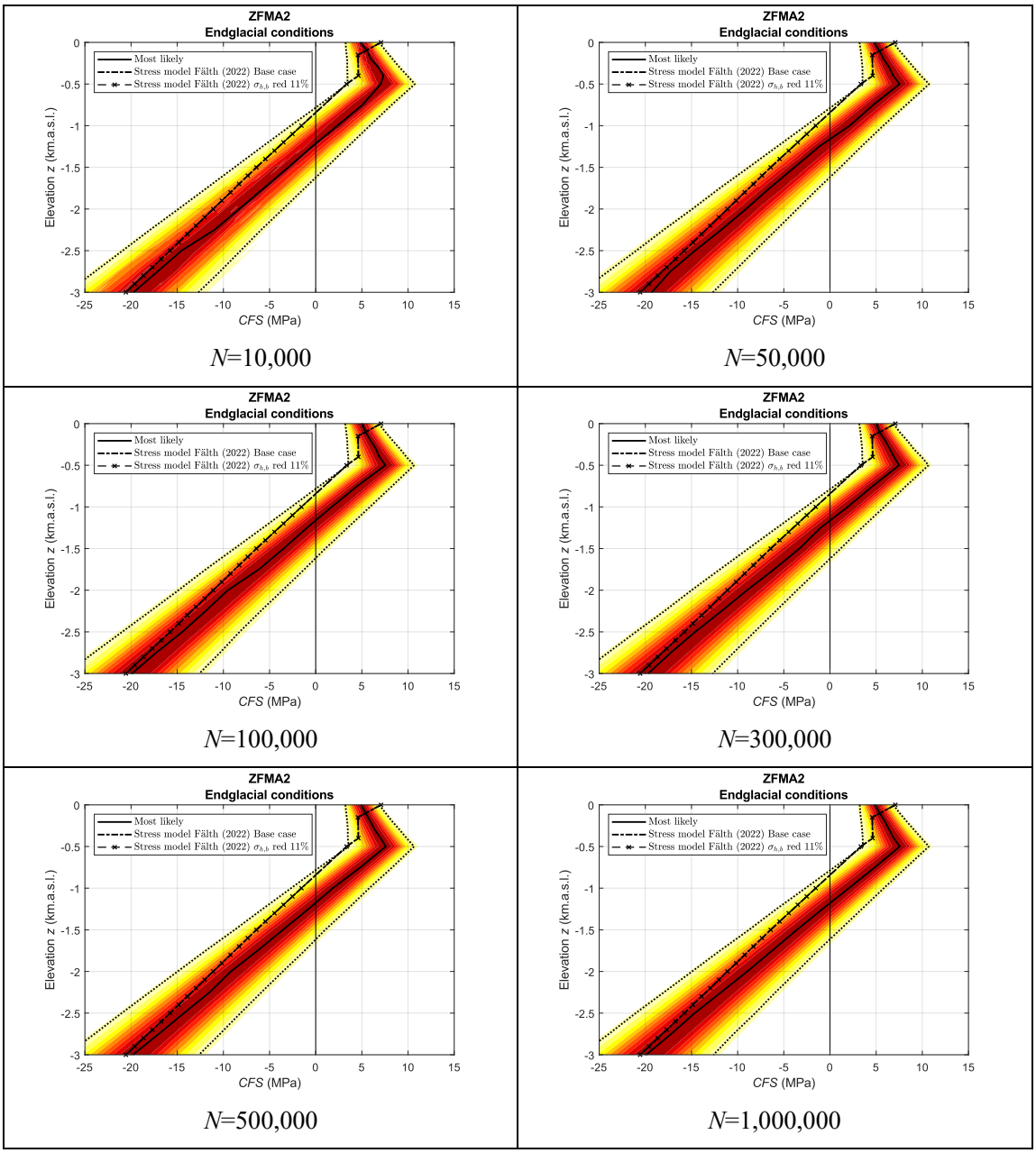

Figure 10-1. *CFS as function of depth for the ZFMA2 under glacial load conditions. The plots show the effect of using different numbers of realisations N when generating the input parameter distributions. The colour scale indicates the relative probability of CFS, and the dotted lines indicate the 95 % confidence interval. The solid line indicates the most likely CFS values. For reference, CFS values based on the input stresses used in the stability estimates by Fälth (2022) are also plotted.*

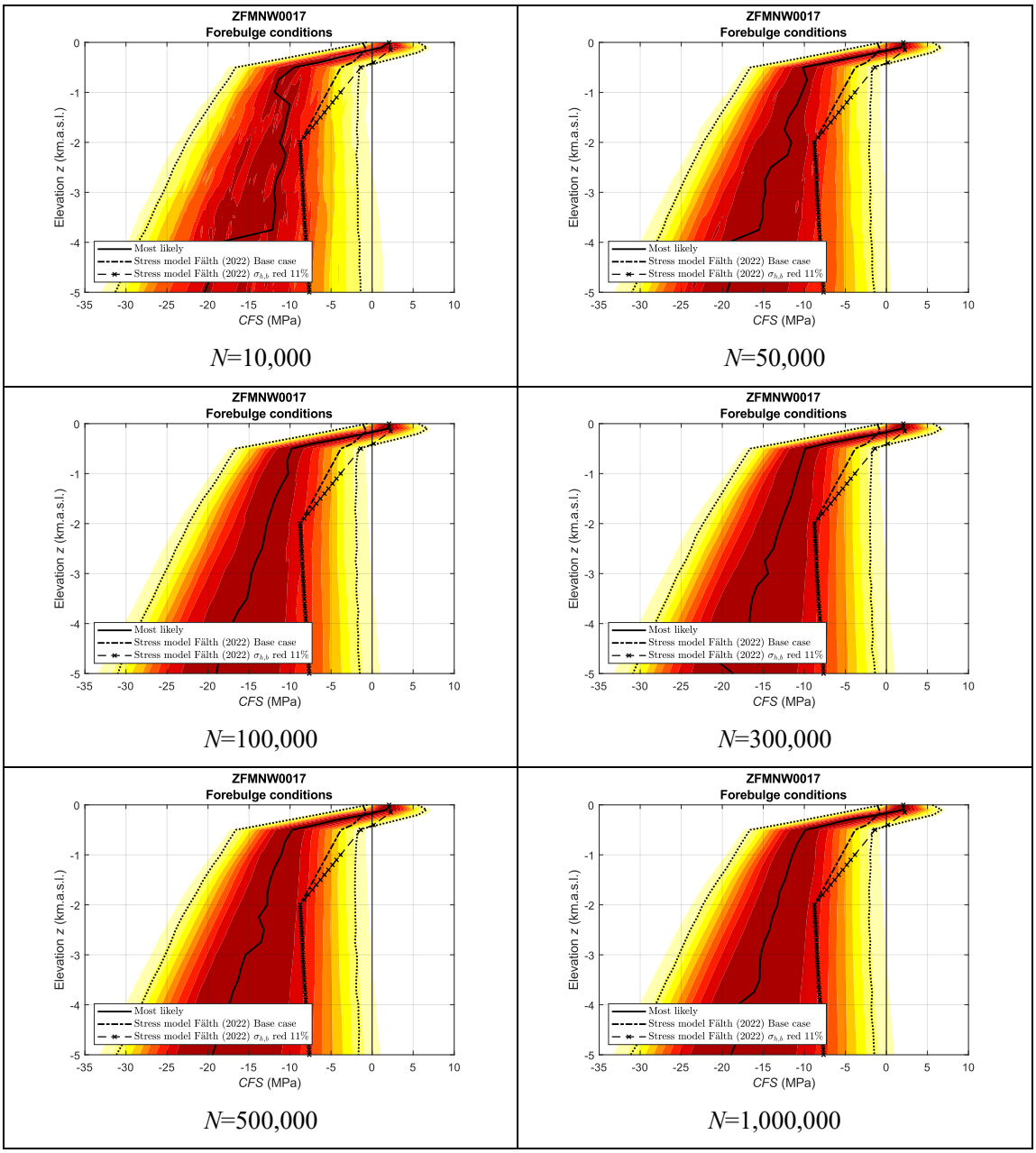

Figure 10-2. *CFS as function of depth for the ZFMNW0017 under glacial load conditions. The plots show the effect of using different numbers of realisations N when generating the input parameter distributions. The colour scale indicates the relative probability of CFS, and the dotted lines indicate the 95 % confidence interval. The solid line indicates the most likely CFS values. For reference, CFS values based on the input stresses used in the stability estimates by Fälth (2022) are also plotted.*

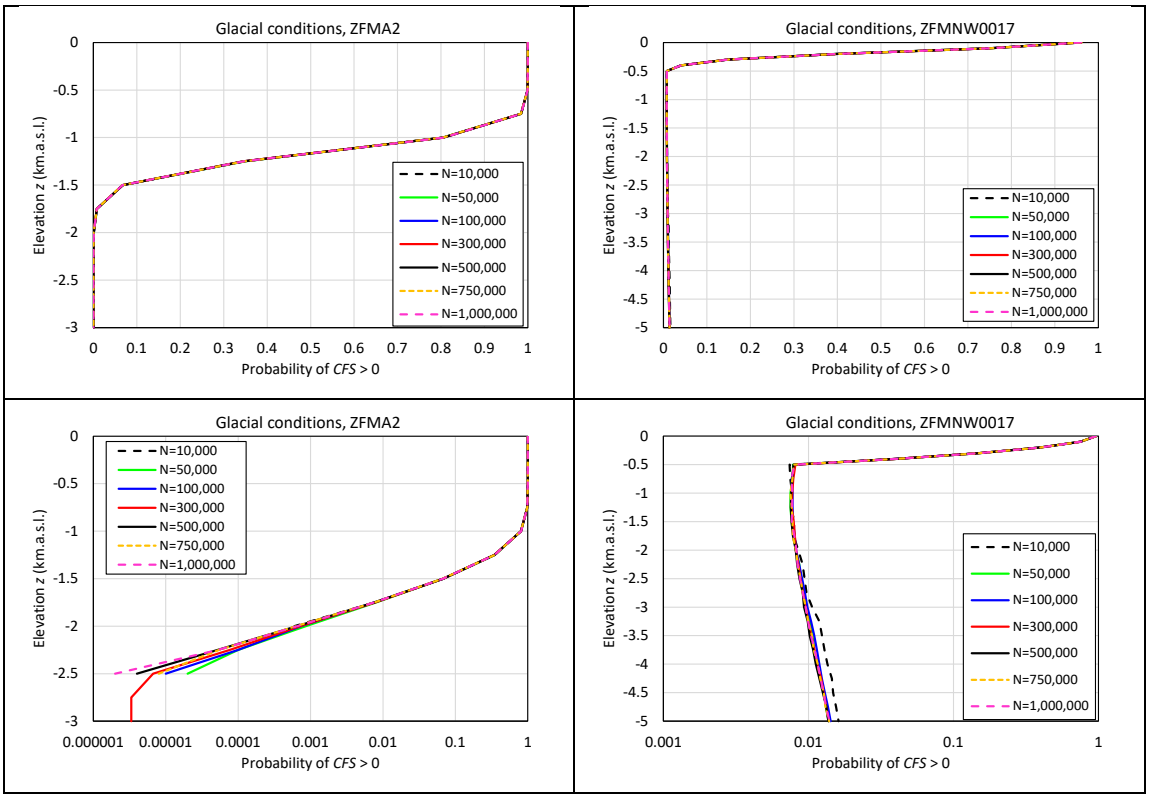

Figure 10-3. *Probability of CFS > 0 as function of depth for ZFMA2 and ZFMNW0017 under glacial load conditions when using different numbers of realisations when generating the input parameter distributions. The diagrams in the upper and lower rows show the same results, but the diagrams in the lower row have logarithmic x-axis scales.*